ABSTRACT

EXPERIMENTAL AND THEORETICAL MODELING STUDIES OF THE SIEGFRIED MASS IDENTIFICATION SYSTEM

By

Marcello Michael DiStasio

The electrostatic mass identification system, SIEGFRIED was used to identify short-lived nuclear reaction products. A combination of Helium Jet Recoil Transport and Time-of-Flight methods was employed for Al, KCl, Ti, Sm and NaF targets. Both β-mass and γ-mass coincidence experiments were performed.

All measurements were made using the 70-MeV ^{3}He beam from the Michigan State University Sector-Focused Cyclotron.

Theoretical modeling of the Time-of-Flight system was accomplished by numerical methods. This modeling was used to explain observed mass peak broadening in terms of the recoil nucleus initial kinetic energy which results from β decay. The possibility of measuring β-decay Q values from observed peak broadening is demonstrated.

EXPERIMENTAL AND THEORETICAL MODELING STUDIES OF THE SIEGFRIED MASS IDENTIFICATION SYSTEM

By

Marcello Michael DiStasio

A DISSERTATION

Submitted to
Michigan State University
in partial fulfillment of the requirements
for the degree of

DOCTOR OF PHILOSOPHY

1980

ACKNOWLEDGMENTS

Thank you to Professor William C. McHarris for serving as my thesis advisor and for all his support through my graduate career. I would also like to thank Dr. William Kelly for all the time and trouble he spent in fulfilling his role as my second reader. To Ray Warner and Richard Firestone I want to express my appreciation for much help and guidance.

Thanks to Dr. D. O. Riska for invaluable discussions and suggestions concerning theoretical matters. I would also like to thank Richard Au and Barb Woodward.

Special thanks to Wayne Bentley for countless hours of help on the experimental work for this thesis.

Thank you to Peri-anne Warstler for an excellent job of typing this work.

Thanks to Roy Gall and Sandy Koeplin for the special friendship they extended to me.

My sincerest thanks to my mother and father for continuing faith and love, all that I accomplish is but a small acknowledgment of their devotion.

To my brother and sisters, thank you for the love and support you have always given.

Finally, a continuing and loving thanks to my wife, Ernie, for her love and understanding over all these years.

TABLE OF CONTENTS

LIST OF TABLES

LIST OF FIGURES

CHAPTER I

INTRODUCTION

The development and refinement of many new and ingenious instruments for investigations of nuclei from the region of β-stability has made such endeavors challenging and rewarding. Experiments that were very difficult ten years ago are fast becoming relatively easy and almost routine. Among the new techniques are the Helium Jet Recoil Transport system (HeJRT), the Rabbit system, and a number of new time-of-flight (TOF) mass identification systems. The HeJRT and Rabbit systems were developed to provide a means of fast transport of short-lived products of nuclear reactions to a low background counting area. This is a very important function when one is dealing with reaction products that have half-lives in the tenths of second range. Besides their short half-lives, another difficulty one must deal with is interfering products. Generally the result of the interaction of a projectile beam with a chosen target is never exclusively the product of interest. One is always faced with the problem of differentiating the species of interest from a crowded field of interfering reaction products. As a means of separating out and studying

a particular isotope of interest, on-line mass separation systems have been developed. The time-of-flight spectrometer is a conceptually simple and increasingly popular instrument for isotope identification. Our system, SIEGFRIED, was constructed toward this end.

The basic principle of SIEGFRIED, as of all TOF systems, is that nuclei of varying masses may be differentiated according to the time each mass requires to traverse a given flight path length. In our system each mass is initially accelerated to a known velocity and then allowed to drift a known length. Measurement of the time-of-flight yields the associated mass. In contrast to many other TOF systems, SIEGFRIED was developed as a means of labeling a β-decay event with the associated mass resulting from the decay; it was not originally intended to provide highly precise mass measurements. In this respect SIEGFRIED is analogous to the fast chemical separation techniques used for the study of short-lived nuclei. These techniques were invaluable in dealing with complex mixtures of radioactive reaction products. Serving a similar function SIEGFRIED is a fast, mass identification system.

Our mass identification system is actually a result of coupling a HeJRT system, for transport, to the TOF system, for mass identification. Some of the original work along these lines was accomplished by a group at Texas A & M (Ju71). They used their MAGGIE system to analyze recoils

from α-decay. To demonstrate that recoils from β-decays could be mass analyzed by TOF methods the MSU SIEGFRIED project was initiated (Ed76). As with so many supposedly simple instruments unexpected results often manifest themselves. Closer inspection of the details of our TOF spectra leads one to suspect that a great deal of interesting information about the nuclear decay associated with an observed recoil mass, is being preserved in the observed mass peaks. In order to confirm or refute such suspicions, it is necessary to gain a clear understanding of precisely how the SIEGFRIED TOF system works. In a large measure, this will be a main thrust of our discussion. In this thesis we will attempt to dovetail experimental results in various mass regions with a rigorous theoretical modeling study of the system. Of course the model will not be an exact simulation of the system yet we will strive for the most realistic representation possible while still practical.

Before proceeding to the bulk of our presentation I would like to point out that our system has resulted directly and indirectly from the work of many researchers in the area of TOF measurements. As is the case with many experimental systems, SIEGFRIED has provided us with a number of successes, a fair share of frustrations, and a plethora of intriguing potentialities. Among the successes we should first count the fact that SIEGFRIED has proven that β-recoil ions can be routinely mass analyzed. This is something that

only a few years ago was an uncertain hypothesis. Second, as will be shown in later chapters, we have employed SIEGFRIED for mass identification over a range of different mass regions with fair success. These experiments have been performed, in part, to investigate the utility of, and difficulties associated with our system when applied to a variety of cases that one would expect to obtain reasonable results. Third, we will demonstrate in this work that a prime bit of information that can be obtained from our mass peaks is the initial recoil energy of the observed β-decay product. This is a quantity that is directly related to the β-decay energy.

CHAPTER II

DETAILS OF TOF SYSTEM

Since a detailed analysis of our Time-of-Flight (TOF) system will comprise a significant portion of subsequent discussions it is worthwhile at this point to provide a brief exposition concerning the design and use of the SIEGFRIED spectrometer. Many aspects of our instrument and the TOF measurement process are not unique to SIEGFRIED but are common to many TOF systems. In the following presentation the only details relating to SIEGFRIED that will be stressed are those that represent changes from the original construction. They are modifications effected by the author that should be noted by future users of SIEGFRIED. For a full discussion of the design and construction of SIEGFRIED, see reference (Ed76).

In a "typical" experiment for TOF measurements, nuclear reaction products are generated with the MSU Sector-Focused Cyclotron and transported to SIEGFRIED by means of a Helium Jet Recoil Transport System (HeJRT). In this HeJRT system a gaseous mixture of He, impurities, and reaction products flow through a capillary tube and into an evacuated chamber of SIEGFRIED that is called the skimmer chamber. The

gaseous mixture is directed at a conical skimmer which acts to remove most of the helium gas (See Figure 2-1). The reaction products are attached to large molecular "clusters" which have a smaller divergence as they flow from the end of the capillary and so have a higher probability of passing through the skimmer assembly and striking the stainless steel collecting plate in the collection chamber. These molecular clusters stick to the collecting plate and provide a very thin source. The metallic collecting plate is held at a static, positive high voltage, usually +6 kV with respect to SIEGFRIED ground potential.

When one of the radioactive species undergoes a β-decay, a simple sequence of events occurs that is the basis for our time-of-flight measurements. As the nucleus of interest emits the β particle, it will recoil to conserve momentum and leave the surface of the collector. Also, when a nucleus emits a β particle, there is a resulting sudden change in the nuclear charge from Z to Z ± 1. This very fast change causes a pertubation on the electrostatic potential in which the atomic electrons move and often results in the ejection of an atomic electron. Studies (Ca63) have shown that in the majority of ionizing events a +1 charge state results.

The positive ions so created are then accelerated across a region of nearly uniform electric field, transforming the 6 kV of potential into kinetic energy. The

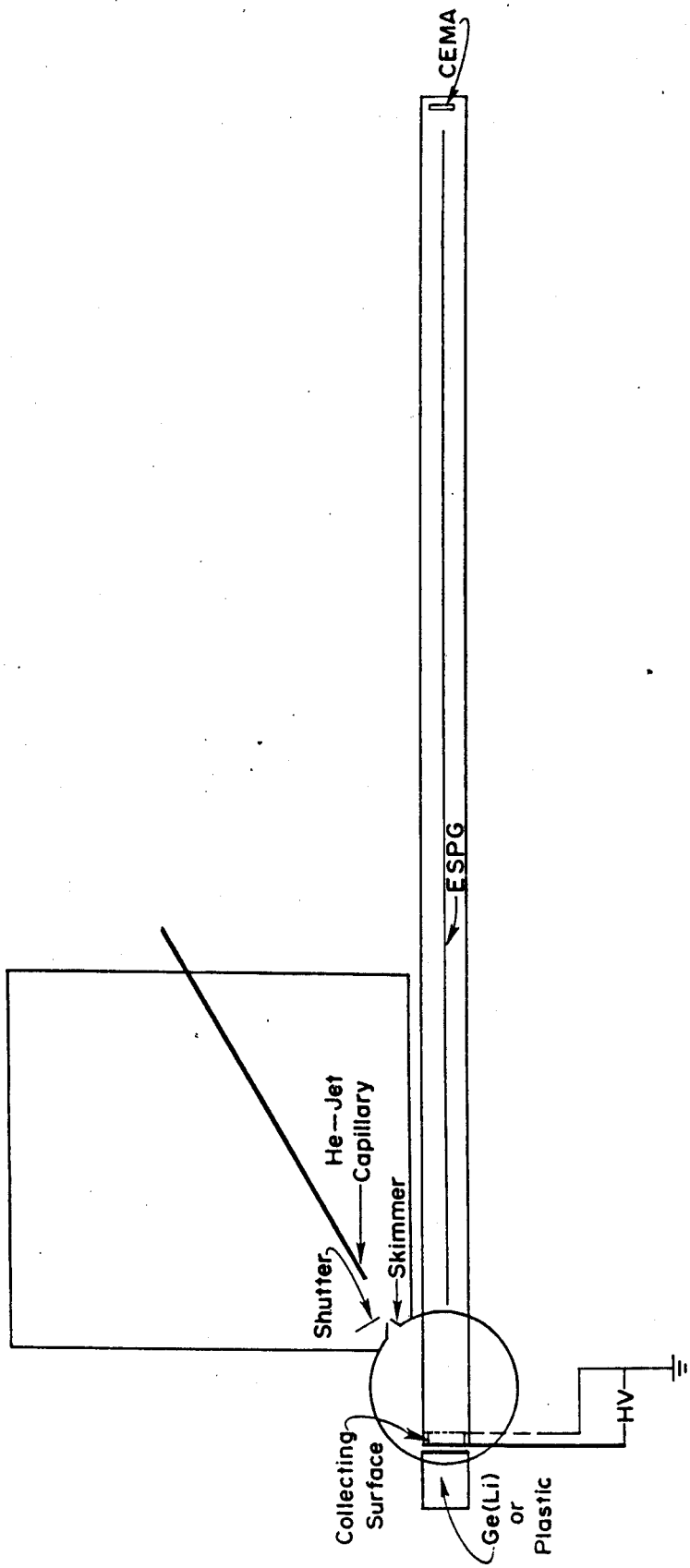

Figure 2-1. Schematic diagram of SIEGFRIED.

acceleration zone is in effect a circular plate capacitor with the collector at 6 kV as one plate and a disc formed of fine wire mesh (90% transmission mesh) acting as the ground plate.

After passing through the wire mesh disc, which effectively completes the ion acceleration, the recoiling ions enter a weak field region we will refer to as the "flight tube". In this portion of the instrument there is a very small diameter (0.005 cm) wire held at a small negative voltage (-110 V) concentric with a relatively large radius (5.25 cm) pipe that is held at ground. The result of this configuration is a region of logarithmic potential: the wire, commonly called an Electrostatic Particle Guide (ESPG), acts to focus the recoil ions in the radial direction and onto a set of Channel ELectron Multiplier Arrays (CEMA) that serves as the ion detector. A set of two CEMA's is often called a Chevron detector. The CEMA's are positioned close to the end of the flight tube, roughly 1 m away from the collector plate and the source.

The electronics necessary for a mass measurement is made up of standard NIM modules that are widely employed by nuclear experimentalists. The basis of the measurement is as follows: (1) a radioactive species emits a β particle that strikes a plastic scintillator, which provides a start pulse for a Time to Pulse Height Converter (TAC); (2) the

recoil ion, after acceleration and drift down the length of the flight tube, strikes the CEMA detector and generates a pulse that stops the TAC; (3) the TAC then gives a voltage output that is proportional to the recoil ion time of flight.

In Figure 2-2 is shown a minimum electronics block diagram for a mass TOF measurement. The function of this set-up is to perform a simple delayed coincidence measurement. The anode output from the plastic scintillator photomultiplier tube is fed to timing filter amplifier (TFA) for shaping and amplification. The TFA output is then processed by a Constant Fraction Timing Discriminator to provide a very sharp, fast start pulse for the TAC. The output from the CEMA preamp is sent through an identical set of NIM modules and so generates the stop signal for the TAC. The output of the TAC is sent to an analog-to-digital converter (ADC); the digitized output of the ADC is then stored in a computer as the TOF spectrum of interest.

The basic operation of SIEGFRIED has remained virtually unchanged since the original construction was completed in 1976 by M. Edmiston. Nevertheless, we have made a few modifications related to the system that are necessary to document for future use of SIEGFRIED. The two most important changes are: (1) design and inclusion of a safety control unit for the power to the CEMA's and (2) a new set of CEMA detectors.

The CEMA's are a rather delicate set of detectors, and

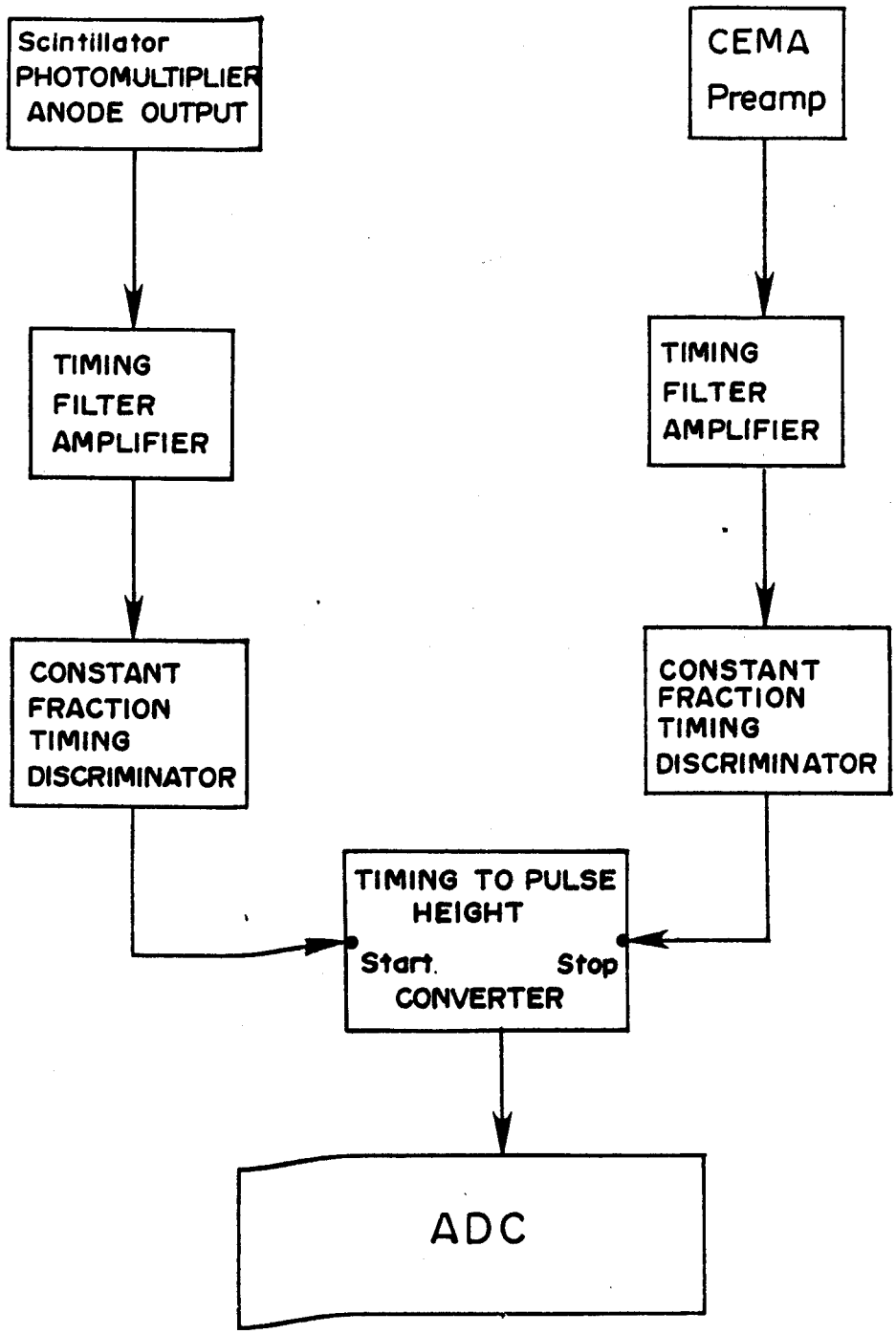

Figure 2-2. Electronics for TOF mass measurement.

the manufacturer (Bendix Corporation) warns that they should not be powered in any vacuum worse than 10^{-5} torr at the risk of their destruction. In the original operation mode of SIEGFRIED the only safeguard against the destruction of the CEMA detectors during an experiment was through interlocks between two vacuum valves, V4 and V6 (see Figure 2-3), and the power supply for the detectors. Actually, these interlocks were not meant to serve as a safeguard system against problems arising during the length of an experiment. Originally the interlock system was intended to ensure only that the CEMA detectors were not powered before the vacuum in SIEGFRIED was below a level safe for operation of the detectors. Well, true to form this interlock system did not function as the failsafe it was never intended to be, as the old CEMA detectors met with a rather quick and complete demise during the course of an early experiment. This sudden, distasteful development is what led to the second of the aforementioned modifications related to SIEGFRIED -- acquisition of a new set of CEMA detectors.

The new channel plates were purchased from the Bendix Corporation, product number 302-B-005-MA. In many respects the new CEMA's are much the same as the old ones, both sets functioning according to the same ingenious theory of operation which is well described in the Technical Application Note provided by the manufacturer. The new CEMA's are thinner and draw less current than the old set, but a most

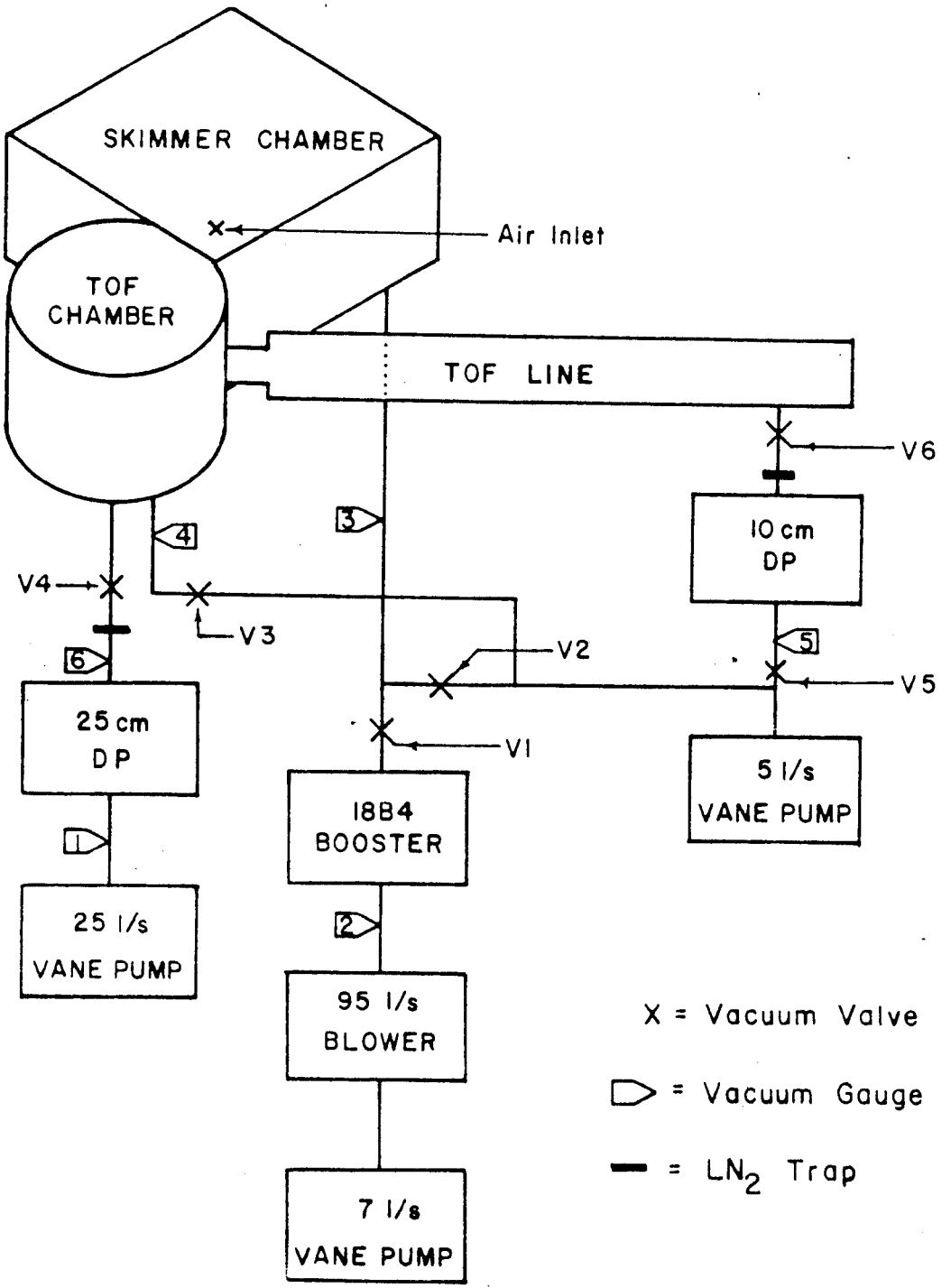

Figure 2-3. SIEGFRIED's vacuum system.

important difference between the old set and the new that cannot be overemphasized is that the new CEMA detectors require -2000 V bias. The old set required -2700 V for operation. This particular difference is especially important to note carefully since using the wrong high voltage setting can easily lead to serious damage of the new CEMA's -- if not their complete destruction as functional detectors.

Another difference between the old and new sets of CEMA detectors is of much less importance than the power requirements but interesting nonetheless. The bias angle of a CEMA is the angle that the channels make with the normal to the detector face. Greater bias angles alleviate a problem that is known as ion feedback. The new CEMA's have bias angles of 8° as compared to 0° and 5° of the old CEMA chevron set, this means that the new set will have a better signal-to-noise ratio than the old set.

As a result of our experience of destroying the CEMA's, it was decided that a fast and reliable means of safeguarding the new set of detectors was a rather obvious necessity. A safety-control unit was designed, constructed, and put into operation as a reliable means of quickly shutting down power to the CEMA detectors in the event of a sudden bad vacuum and/or a large current flow through the CEMA's -- both of which can damage or destroy the multiplier array detectors that are vital for the operation of SIEGFRIED and are very expensive.

In Figure 2-4 is shown the circuit schematic for the safety control unit for the CEMA detectors. Power is from an ORTEC 459 power supply that has a remote shutdown feature and so can be effectively turned off by the control unit. The 10 μA meter shown monitors the current drawn by the CEMA's; if this current exceeds the setpoint (usually ≈3 μA), the meter will cut off the power to the CEMA's. In many tests of this system, intentional or not, the failsafe has been highly successful. The vacuum interlock system was not so useful as the current interlock portion. There were two reasons for this. First, the only region of vacuum that is of value to the safeguard system is around 10^{-5} torr. The only reliable means to monitor the vacuum in that range is utilizing vacuum gauges that generate ions in such quantities as to create severe noise problems in the CEMA's. Second, the vacuum interlock system only provides a redundancy of the overcurrent safeguard that, in view of the noise problem, is of reduced value.

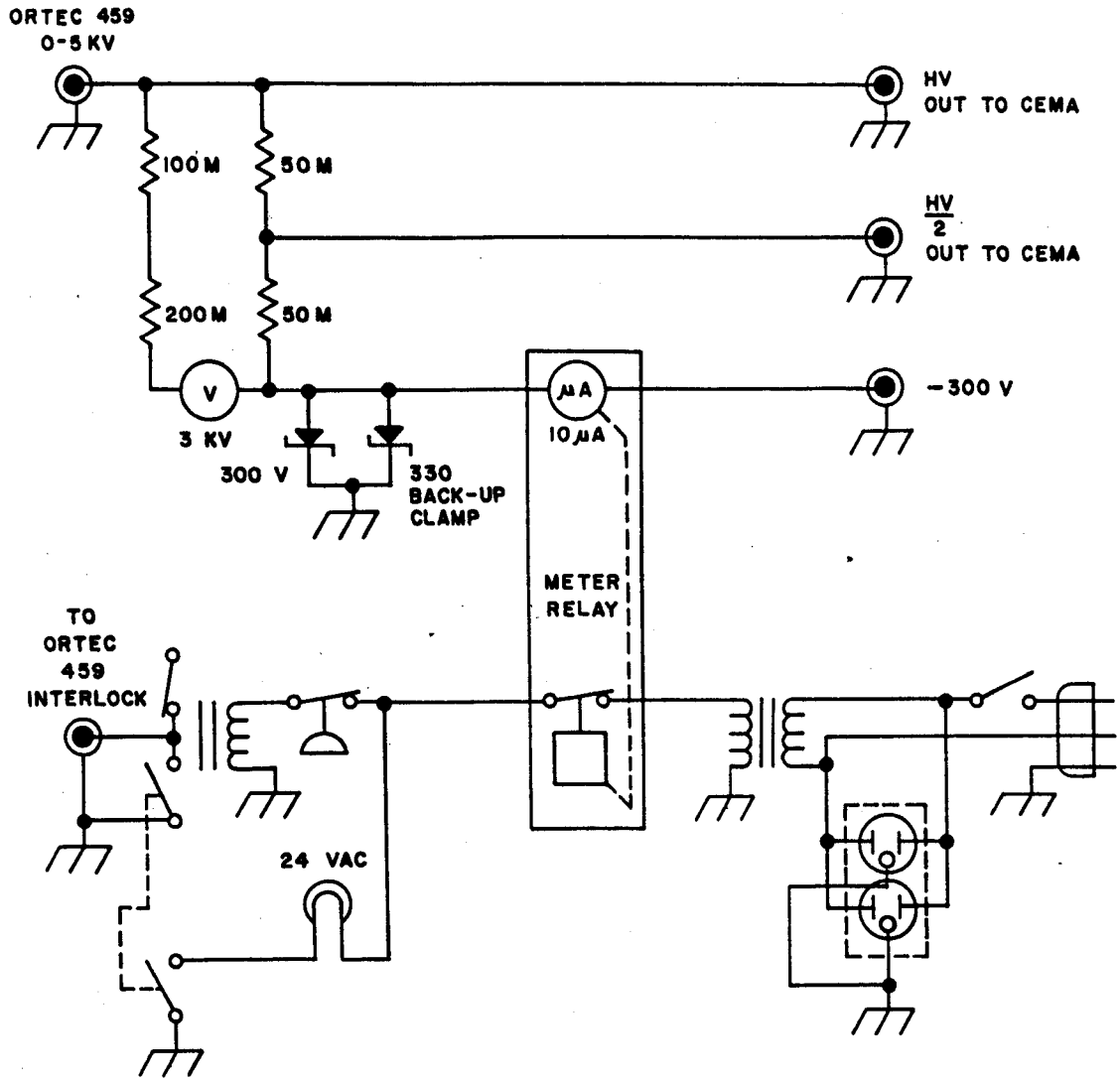

Figure 2-4. Schematic for CEMA failsafe.

CHAPTER III

EXPERIMENTAL RESULTS

An important aspect of any experimental instrument is its range of utility. In order to make the greatest use of any apparatus it is necessary to investigate and define the types of systems that are most suited to the capabilities and limitations of the method of measurement. This is especially true of the SIEGFRIED, and the following discussion will attempt to deal with these aspects in a manner that will aid in further use of this time-of-flight system.

The results of a number of TOF measurements for several different targets will be presented and discussed in a manner that will display the reasoning and logic required to design, run, and interpret a mass-identification experiment. In addition, these measurements will present a survey on the use of SIEGFRIED in a number of different mass regions.

The coupling of the HeJRT system to SIEGFRIED presents the experimentalist with a number of advantages that makes such a combination very well suited to the study of short-lived nuclei that fulfill certain criteria. Naturally, species that do not have the appropriate characteristics yield poor or null results. The aforementioned criteria

are unfortunately not quantitative conditions, but the following discussion should serve as a guideline for determining whether a particular TOF measurement is feasible.

The obvious first step in designing an experiment with SIEGFRIED is to choose an appropriate target. Because of the total efficiency of the HeJRT-SIEGFRIED system it is important to select cases with high reaction cross-sections and targets that can withstand maximum beam on target. Foil targets are well suited to such conditions. In a number of runs with chloride and oxide targets it was found that a large quantity of powdery substance had been generated in the target area and had clogged the input end of the HeJRT capillary, which effectively reduced the transport efficiency to zero. The nature of this powder and the mechanism for generating it are both unknown but do constitute a real problem with oxide and chloride targets.

Having decided on the target most suited to the reaction of interest, it is worthwhile to estimate the products of the chosen reaction and their relative cross-sections. This is a task that is best accomplished by using the computer routine called ALICE (B170). ALICE is Fortran code written by M. Blann and F. Plasil and is available on the MSU Σ7 computer as a user's code. The results of ALICE computations give the reaction cross-sections as a function of energy for a number of different reaction products. A number of figures in this section are the result of such

computations which provide a convenient tool for estimating the most probable products from the reaction of interest. After determining the probable reaction products, one must consider the half-lives of these products. The time required for transport of a product from the target area up to the collection plate of SIEGFRIED has been estimated to be on the order of hundreds of milliseconds, so species with half-lives less than a few hundred milliseconds will decay away before reaching SIEGFRIED. Using the HeJRT system at MSU, Edmiston (Ed76) was able to measure the half-lives of ^{47}Cr, ^{46}V and ^{55}Ni. He found these to be 460 ± 1.5 msec, 420 ± 3 msec and 219 ± 6 msec, respectively. These measurements can be used to gain a rough estimate on the upper limit of the transport time. Species with half-lives greater than a few minutes are also difficult to measure with SIEGFRIED. In such cases one must optimize counting and collection intervals as is discussed in this chapter.

The chemical properties of the reaction products and the associated molecular clusters are an important aspect of the transport and measurement process. Though less understood than many details of the system, these properties should be considered in designing an experiment. For the sake of this discussion I will divide the relevant chemical properties into two categories: (1) transport efficiency and (2) sticking efficiency. (This division may well be

partially artificial but will aid in understanding two chemically related aspects of our system.)

Kosanke (Ko73) studied the efficiency of transporting a number of different reaction products with the HeJRT system. It was found that the transport efficiencies varied from 24% to 60% and was also a function of the type and concentration of impurity added to the pure He. The situation now is that the actual nature of the recoil-cluster association has not been elucidated to the point where it is possible to predict the transport efficiency for a given species, but it remains an important point.

Once a species has been transported from the target area to the counting area, it is sprayed onto a surface and if the sample adheres to the surface, a thin film source results. However, it is by no means certain in all cases that the nuclei of interest will stick well enough to remain on the surface until they decay. This "sticking efficiency" was also looked into by Kosanke (Ko73) but only with regard to varying capillary-collecting surface angles and distances. No studies thus far have dealt with this efficiency with respect to differing chemical species, since it has been assumed that the "clusters" stick to the surface and the nuclei of interest somehow adhere to the clusters.

Whatever the actual chemical nature of the transport and sticking process, a few practical observations have been made. In no instances have any noble gases (i.e., He, Ne,

Ar, Xe) been observed even when the appropriate reaction cross-section is fairly high. This seems to be a rather obvious chemical effect, since the noble gases are known to be relatively chemically inert. In a number of experiments performed it has been noted that chlorine and fluorine products had very reasonable cross-sections but were not observed. This may suggest a poor transport and/or sticking efficiency for halide ions.

Once a set of reasonable reaction products have been predicted, one should calculate the time of flight for the heaviest mass expected. This is necessary in order to choose the appropriate TAC scale to be used in the measurement. The time of flight for a nucleus of mass number A for our system can be calculated from the formula

$$TOF(\mu sec) = 2.536 \sqrt{A/HV} \qquad (3\text{-}1)$$

where HV, the voltage applied to the collector plate is in kiloVolts. For a more complete discussion of this equation, see Appendix I.

Having chosen the appropriate time scale for the TAC, it is very important to calibrate the TAC. A convenient method of calibration is to use the Tennelec Model 1030 Time Calibrator, a NIM module that generates start and stop signals suited for most TAC's. A second means of calibration is to use some standard target with a well-known TOF spectrum.

In all of our experiments an Al foil target was used for calibration, since it gives high statistics, well separated peaks, and is simple to construct. This latter method is actually preferable to the former, since it gives a calibration for the system -- not just the TAC. It has been found that a combination of the two calibration procedures is preferred in most cases. (The Time Calibrator allows determination of a precise number of nsec per channel.)

After completion of the data acquisition, one uses the time calibration to extract the measured time of flight; that is, transform channel number to time units. This transformation is a simple linear one. Once the TOF's for each peak are known, the mass number can be extracted by the simple relationship

$$A = 0.155\ (HV)(TOF)^2 \qquad (3\text{-}2)$$

After determining the mass number corresponding to each peak, one must determine the particular isotope that is associated with the known mass number. If a γ-mass coincidence has been run, it may be possible to associate a particular γ ray with a known mass, thus specifying the particular decay. Unfortunately, in our experiments it has been found that the majority of γ rays is annihilation radiation, which, of course, is of little use in characterizing a decay -- except to show it occurs via positron

emission.

For most of our runs we have used β-mass coincidence, recording the TOF and the β energy. For decays with highly different β-endpoint energies one can determine the correct species straightforwardly. However, in many cases the β energies are not greatly different, and because of the poor energy resolution of plastic scintillator no unique characterization is possible.

In the absence of direct measurements uniquely determining Z, one must rely on reasonable deductions. Comparison of the observed masses with the predictions from ALICE calculations often narrows the possible isotopes to one or two choices. After choosing a number of potential candidates, one must consider the relative half-lives and reaction cross-sections to characterize finally the decay that gives rise to the observed TOF peak.

$^{27}Al + {}^{3}He$

Al foils were the first and most frequent targets used for our experiments. The material is readily available in varying thicknesses and the ^{27}Al isotope comprises 100% of the material, so there are no interfering contaminants. In addition, the ^{27}Al (p,xnyp) and ^{27}Al (^{3}He,xnyp) reactions give products that are very well suited for measurements by SIEGFRIED. In the developmental stages of our TOF

system, these reactions were used almost exclusively to provide simple and familiar spectra. Another advantage of these reactions was that an identifiable mass TOF spectrum would result from an hour's worth of counting time with a beam current of roughly 1/2 μA of 70-MeV ^{3}He on target. Also, the decays that give rise to the observed TOF spectra are straightforward ground-state to ground-state decays in most cases. The resultant peaks have a shape that is prototypical of the mass peaks we obtain with SIEGFRIED.

In light of the aforementioned advantages of using Al foil targets, it is natural that this target has come to be used as a source for a standard spectrum for many of our runs. This is especially true in the mass region 20-50 amu.

Using a TAC calibration from the Tennelec Time calibrator, the first peak in Figure 3-1 is found to occur at a TOF of 4.915 μsec. Then, using Equation (3-2) the mass number is found to be 23. Mass 24 does not appear in the spectrum, but, following the same procedure, we assign A = 25-29 successively. As a double check, a linear least squares fit to the TOF's as a function of centroid was performed. The results are given in Table III-1; χ^2 for the fit was 8.0×10^{-6}.

In Figure 3-2 the theoretical excitation functions for $^{27}Al + {}^{3}He$ are plotted. These curves are the result of an ALICE calculation. The plots do not include stable

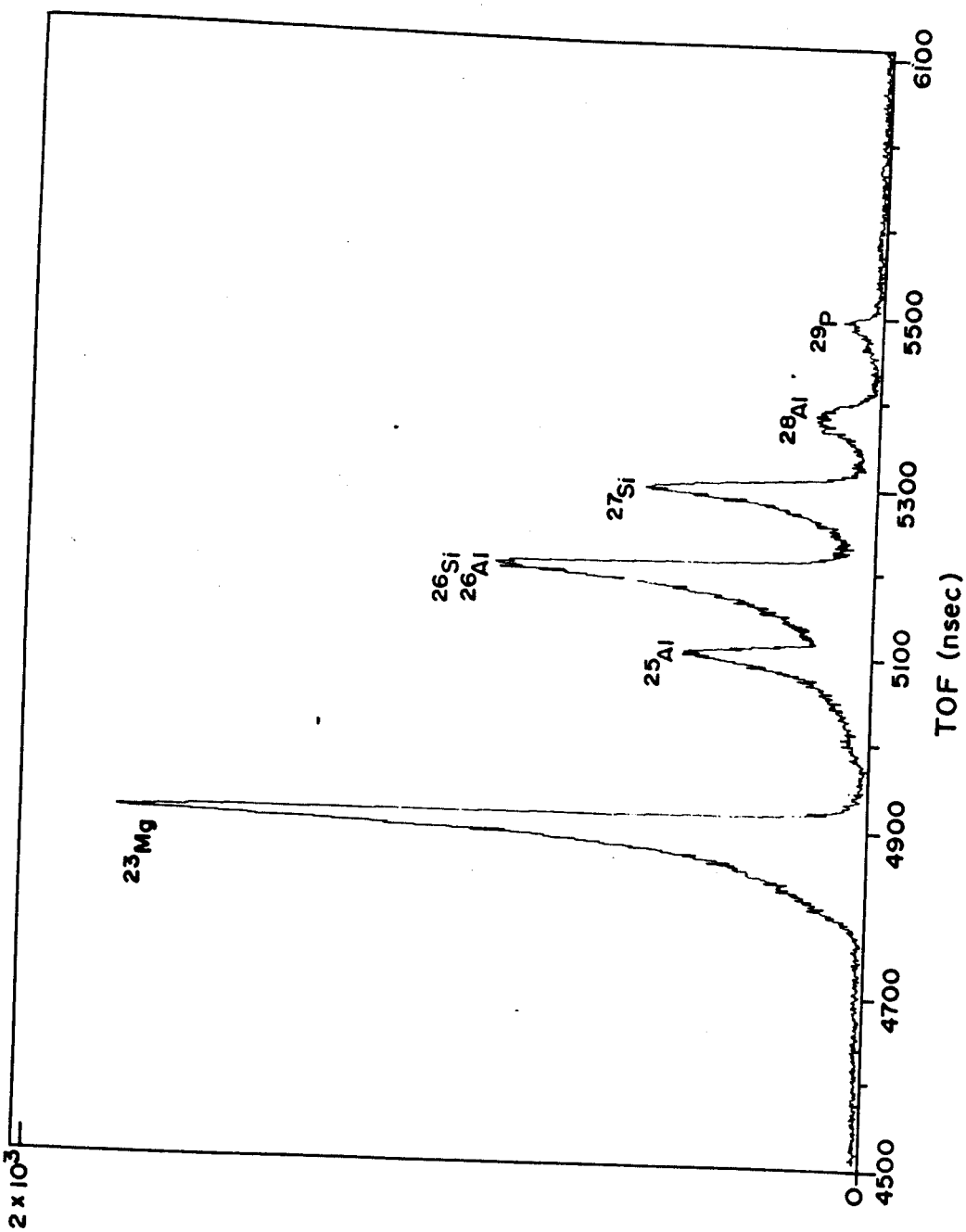

Figure 3-1. TOF spectrum for products of ^{27}Al + 70-MeV ^{3}He.

Table III-1. LSQ Fit to Al TOF Spectrum.

A (AMU)	TOF (μsec)	Centroid (Channel number)	T_{LSQ} (μsec)	Δ (μsec)	A_{LSQ}
23	4.915	5087	4.914	0.001	22.99
25	5.127	5288	5.126	0.001	25.00
26	5.229	5387	5.231	0.002	26.02
27	5.330	5484	5.334	0.004	27.04
28	5.428	5569	5.424	0.004	27.95

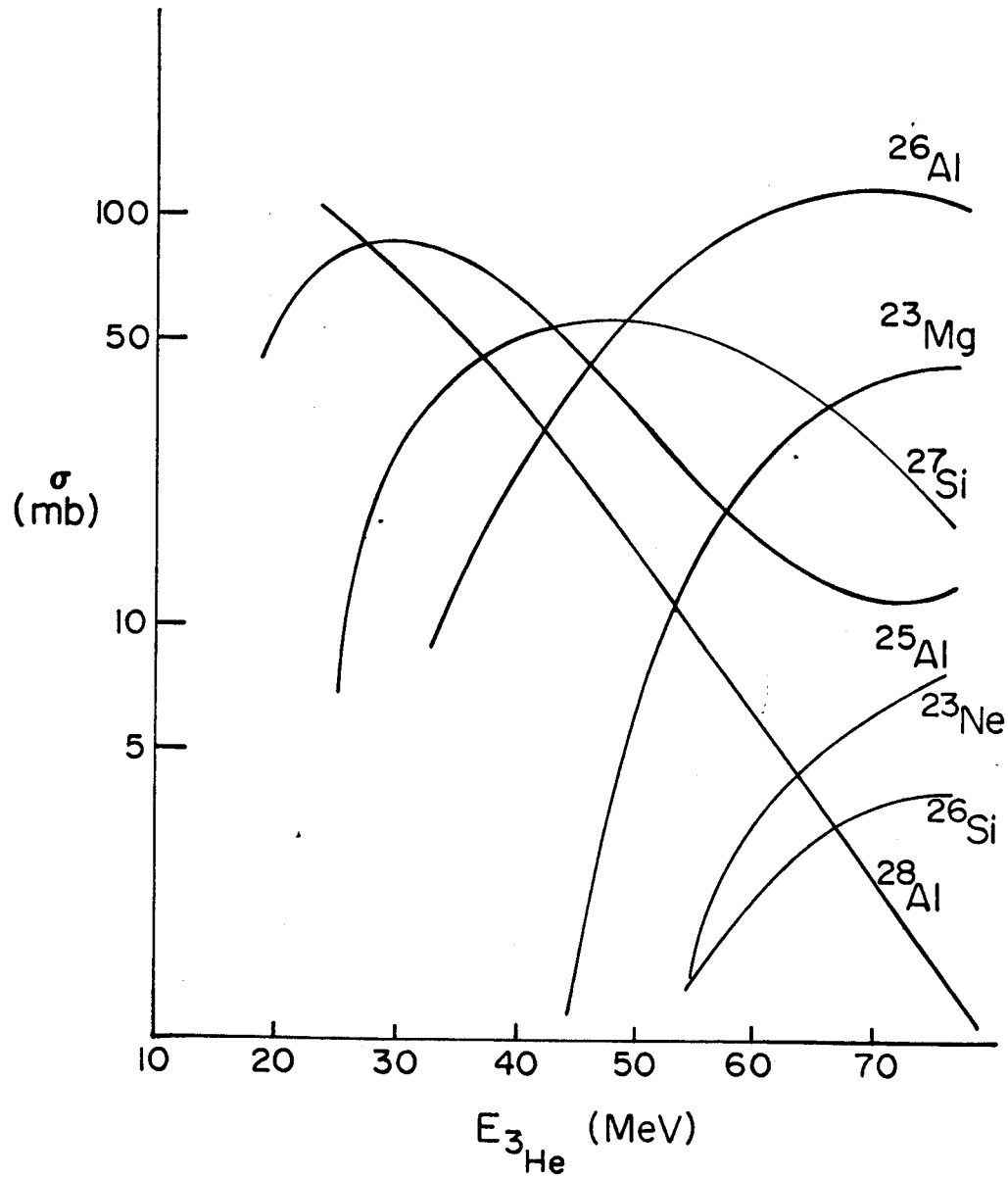

Figure 3-2. ALICE predictions for ^{27}Al + ^{3}He.

products or species with half-lives greater than a few hours, since these products will not be measurable with our system. The spectrum shown in Figure 3-1 is the result of 70-MeV ^{3}He on ^{27}Al. For this experiment we collected and counted for roughly two hours with 1 μA of beam target. In Table III-2 are the integrated areas and the theoretical cross-sections for 70-MeV ^{3}He.

Now that we have the mass number for each of the peaks we must assign an atomic number Z for complete characterization. According to the ALICE calculations (see Figure 3-2) there are two possible sources of the A = 23 peak. They are ^{23}Mg and ^{23}Ne, with ^{23}Mg having about six times as large a reaction cross-section. In addition, ^{23}Ne is a noble gas and thus known to have very poor transport and sticking efficiency. ^{23}Mg is well-suited for SIEGFRIED; studies by Kosanke (Ko73) showed it has good transport and sticking properties. On this basis we have assigned the mass 23 peak to ^{23}Mg. For mass 25, the ^{25}Al is the only possibility with a reasonable half-life (7.2 sec) and reaction cross-section (11.5 mb). ^{25}Na has a suitable half-life (60 sec) but very small cross-section (1.5 mb). The mass 25 peak was assigned to ^{25}Al. In the case of the A = 26 peak, we have two good candidates, ^{26}Al and ^{26}Si. The ^{26}Al has a very large cross-section (117 mb) according to the ALICE calculation, while the ^{26}Si has a cross-section of 3.8 mb. However, the difficulty with the ^{26}Al species is that its

Table III-2. Predicted Cross-sections and Integrated Areas for Al Peaks.

	σ (mb)	Area
^{23}Mg	41	68683
^{25}Al	11	6423
^{26}Al	120	54897
^{27}Si	28	21139
^{28}Al	3	6605

ground state (5^+) has a very long half-life (7.2×10^5y) but its first excited state (0^+) has a half-life of 6.4 sec. Obviously SIEGFRIED will "see" only the decay of the 0^+ state. The problem lies in deciding what fraction of the cross-section results in populating the 0^+ state. Yet even if only 10% of the cross section leads to the 0^+ state, the "effective" cross-section for the 0^+ state of ^{26}Al is still roughly 4 times that of the ^{26}Si. In light of these considerations, we consider the A = 26 peak to be ^{26}Al predominantly, with some contribution from ^{26}Si.

The case of A = 27 is fairly straightforward, since ^{27}Si is the only real possibility. It has a reaction cross-section at 70-MeV ^{3}He of 28 mb and a half-life of 4.1 sec. The mass-28 peak has been assigned to the ^{28}Al species. The strength of this assignment lies in the absence of reasonable alternatives. The cross-section for producing ^{28}Al is only 2.6 mb, which is small compared to the cross-sections from other members of the spectrum. The half-life for ^{28}Al is 2.3 min -- much longer than one might expect to observe strongly with SIEGFRIED's counting mode (this counting arrangement will be discussed later in this chapter). However, among the members of A = 28 isobars there are no other reasonable candidates. The ^{28}P has negligible cross-section and a half-life (270 msec) far too short to be feasible for measurement by SIEGFRIED. In view of the relative strength of the A = 28 peak, it may be that

the ALICE calculation has underestimated σ_{rx} for ^{28}Al.

For the small A = 29 peak, the ALICE calculation suggests that nothing should be there -- an obvious underestimate. ^{29}P has a half-life of 4.1 sec and a moderately larger β^+ energy (4.94 MeV). This is also the result of a $^{27}_{13}Al(^3He,n)^{29}_{15}P$ reaction, which, while not highly favorable with 70-MeV ^3He, is the only reasonable means of obtaining a mass 29 from ^{27}Al + ^3He.

SIEGFRIED Kinetics

During the collection interval we spray activity onto a collection plate continuously so that the amount of fresh source accumulated would be linearly proportional to the collection time if the species were stable. The deposited activity is radioactive; it has a characteristic half-life and associated decay constant. Therefore, during the collection interval some of the source decays. We will assume that the kinetic equation describing the change in the number of species per unit time is

$$\frac{dN}{dt} = - \lambda N + S \qquad (3\text{-}3)$$

S is the source term, assumed to be constant during the collection interval. The solution to this equation is

$$N(t) = N_o\, e^{-\lambda t} + \frac{S}{\lambda} (1-e^{-\lambda t}) \qquad (3\text{-}4)$$

where t is the time measured from the start of the interval and N_o is the number of atoms at t = 0. During the counting interval there is no source term and we have the simple exponential relation,

$$N = N_i \, e^{-\lambda t} \qquad (3\text{-}5)$$

where N_i is the number of atoms present at the time t_i. In effect, the source term turns on and off at regular intervals, as shown schematically below. This corresponds to a slightly different kinetic behavior for successive "bins."

Collection (1)	Count (1)	Collection (2)	Count (2)	. . . .
$\frac{dN}{dt} = -\lambda N+S$	$\frac{dN}{dt} = -\lambda N$	$\frac{dN}{dt} = -\lambda N+S$	$\frac{dN}{dt} = -\lambda N$	
t_o	t_1	t_2	t_3	t_4

Since we have regular intervals, by taking $t_o = 0$, we have $t_i = i\Delta t$. We are interested in the numbers present at the endpoints of the intervals.

At the start of the first collection interval, $N_o = 0$, there are no species present. Defining $g(\Delta t) = \frac{S}{\lambda}(1-e^{-\lambda \Delta t})$, we have the following sequences:

$t = t_1 = \Delta t$ $\quad N(\Delta t) = g(\Delta t)$

$t = t_2 = 2\Delta t$ $\quad N(2\Delta t) = N(\Delta t)e^{-\lambda\Delta t}$

$= g(\Delta t)e^{-\lambda\Delta t}$

$t = t_3 = 3\Delta t$ $\quad N(3\Delta t) = (N(2\Delta t)e^{-\lambda\Delta t})e^{-\lambda\Delta t} + g(\Delta t)$

$N(3\Delta t) = g(\Delta t)\ (1 + e^{-2\lambda\Delta t})$

$t = t_4 = 4\Delta t$ $\quad N(4\Delta t) = N(3\Delta t)e^{-\lambda\Delta t}$

$N(4\Delta t) = g(\Delta t)\ (e^{-\lambda\Delta t} + e^{-3\lambda\Delta t})$

.

.

.

$t = (2j-1)\Delta t$ $\quad N((2j-1)\Delta t) = g(\Delta t) \sum_{k=0}^{j-1} e^{-k(2\lambda\Delta t)}$

$t = 2j\Delta t$ $\quad N(2j\Delta t) = N((2j-1)\ t)\ e^{-\lambda\Delta t}$

.

We count the number of disintegrations in each count interval,

$$D(2j\Delta t) = N((2j-1)\Delta t)(1-e^{-\lambda\Delta t}) \qquad (3\text{-}6)$$

The total number of disintegrations counted after M counting intervals is D:

$$D_M = \sum_{j=1}^{M} D(2j\Delta t) = \sum_{j=1}^{M} (1-e^{-\lambda\Delta t})N(2(j-1)\Delta t)$$

$$D_M = g(\Delta t)(1-e^{-\lambda\Delta t}) \sum_{j=1}^{M} \sum_{k=0}^{j-1} e^{-k(2\lambda\Delta t)}$$

So we see that the total number of possible disintegrations counted is a double sum of decreasing exponentials -- a rather inconvenient form to evaluate, since both sums are finite. Normally one might choose some sufficiently small number to be the truncation limit and use that truncated sum. But careful inspection shows that the sum is actually a geometric progression, which turns out to reduce to much simpler form: (Gr65)

$$I_M = \sum_{j=1}^{M} \sum_{k=0}^{j-1} e^{-kx}$$

$$\sum_{k=0}^{j-1} e^{-kx} = \sum_{k=1}^{j} e^{-(k-1)x} = \frac{1-e^{-jx}}{1-e^{-x}}$$

$$I_M = \sum_{j=1}^{M} \left(\frac{1-e^{-jx}}{1-e^{px}}\right) = \frac{1}{1-e^{-x}} \left\{ \sum_{j=1}^{M} 1 - \sum_{j=1}^{M} e^{-jx} \right\}$$

$$\sum_{j=1}^{M} 1 = M \qquad \sum_{j=1}^{M} e^{-jx} = e^{-x} \sum_{j=1}^{M} e^{-(j-1)x} = e^{-x} \left\{ \frac{1-e^{-Mx}}{1-e^{-x}} \right\}$$

$$I_M = \frac{1}{1-e^{-x}} \left\{ M - \frac{e^{-x}(1-e^{-Mx})}{1-e^{-x}} \right\}$$

So we have succeeded in collapsing a finite double sum

to a simple algegraic form. Taking $x = 2\Delta t$, we have

$$D_M = \frac{S}{\lambda}(1-e^{-\lambda\Delta t})^2 \; I_M = S \cdot F_M(\lambda, \Delta t)$$

$$D_M = \frac{S}{\lambda} \frac{(1-e^{-\lambda\Delta t})^2}{(1-e^{-2\lambda\Delta t})} \left\{ M - \frac{e^{-2\lambda\Delta t}(1-e^{-2\lambda\Delta t})}{(1-e^{-2\lambda\Delta t})} \right\}$$

A much more concise form than the double sum.

Turning to the mechanistic side, we see that the total number of disintegrations is linearly proportional to the source term S, which is intuitively reassuring. If we wish to compare calculations with observed results, a model of S myst be hypothesized. This is very difficult, since the source term S, representing the mechanism for adding fresh sample to the collection plate, is an unknown but certainly complicated quantity! Realistically, it should be function of the relevant reaction cross-section, transport efficiency, transport time, and sticking efficiency. We can use the ALICE calculations to provide reaction cross-sections. In order to take the transport time into account, we suppose that the radioactive species with a decay constant λ will decay during the total transport time τ; thus, a factor $\exp(-\lambda\tau)$ reduces the source term from the start of transport. Different species might have different transport

times, but if we accept a molecular cluster transport mechanism, we would expect τ to be species independent, since the massive clusters should have roughly the same τ. To compare with the observed peak areas, A_i we will assume:

$$A_i = \varepsilon D_M^i = \varepsilon S_i \, F_M(\lambda_i, \Delta t)$$

where ε is the efficiency of SIEGFRIED itself, which should be independent of species. For source term we use the form

$$S_o = \gamma_i \cdot e^{-\lambda_i \tau} \sigma_i \cdot I \, N$$

γ_i is the transport efficiency for species i, σ_i is the reaction cross-section, I is the beam current on target, and N is the number of target atoms. We are actually interested in relative quantities, so we will normalize to a specific case. For the case of the Al spectrum I used the largest peak ^{23}Mg for the normalization. If we take $a_i = A_i/A_{23}$ and $\eta_i = \gamma_i/\gamma_{23}$

$$a_i = \left(\frac{\gamma_i}{\gamma_{23}}\right)\left(\frac{\sigma_i}{\sigma_{23}}\right) e^{(\lambda_{23}-\lambda_i)\tau} \frac{F_M(\lambda_i)}{F_M(\lambda_{23})}$$

$$a_i = \eta_i \, \psi_i$$

From the last form we can estimate the relative transport efficiency η_i from a_i, an experimental quantity, and ψ_i, a calculated parameter. For the spectrum of Figure 3-1 we collected for two hours with 4-sec counting intervals, so $\Delta t = 4.0$ and $M = 900$. The results of this calculation are given in Table III-3. All parameters have been normalized to the ^{23}Mg peak, the largest in the spectrum. The last column gives the relative transport efficiency according to our model. The values for the ^{25}Al, ^{26}Al, and ^{27}Si cases appear reasonable in the absence of any corraborative figures. The value for the ^{28}Al is excessively high, perhaps reflecting an unusually low value for the reaction cross-section (2.6 mb). This dependence on the calculated cross-section may also explain the difference in the transport coefficients for the ^{25}Al and ^{26}Al cases. Since both are aluminum isotopes, and so chemically equivalent, their transport coefficients should be the same.

NaF + ^{3}He

In an attempt to observe some light mass TOF spectra and to obtain a high multiplicity of peaks it was deemed worthwhile to use targets made up of binary compounds. We wanted to use compounds whose components both seemed likely to result in products that would be suited to measurement by SIEGFRIED.

Table III-3. Results of Kinetics Study of Al Spectrum.

	$t_{1/2}$	$e^{(\lambda^{23}-\lambda^{i})\tau}$	$(\sigma^{i}/\sigma^{23})rx$	$\frac{F(\lambda^{i})}{F(\lambda^{23})}$	ψ_i	a_i	n_i
^{23}Mg	12.1	1.0	1.0	1.0	1.0	1.0	1.0
^{25}Al	7.2	0.981	0.28	0.993	0.273	0.093	0.34
^{25}Al	6.4	0.975	2.93	0.990	2.83	0.799	0.28
^{27}Si	4.2	0.948	0.68	0.971	0.626	0.308	0.49
^{28}Al	132	1.026	0.063	0.980	0.063	0.096	1.51

Our first choice was a NaF pressed powder target. The excitation functions resulting from ALICE calculations for $^{23}Na + {}^{3}He$ and $^{19}F + {}^{3}He$ are shown in Figures 3-3 and 3-4, respectively. In Table III-4a and III-4b are given the expected products, their associated half-lives, calculated cross-sections, β decay energies, and associated recoil energies for ^{23}Na + 70-MeV ^{3}He and ^{19}F + 70-MeV ^{3}He, respectively. All the cases tabulated possess a number of attractive characteristics that make them well suited for TOF measurements by SIEGFRIED. The majority of half-lives are on the order of tens of seconds. The decay energies are large enough to result in large recoil energies. In the cases of ^{16}N and ^{20}F, the very large decay energies give rise to huge recoil energies -- 4 keV and 1.5 keV, respectively. Such recoil energies are quite appreciable fractions of the usual 6-kV accelerating voltage employed in our system.

As will be shown in following discussions, the broadening effects from such large initial kinetic energies would be very pronounced in the resulting TOF spectrum. This would provide us with a highly graphic demonstration of the dependence of TOF peak widths on the initial recoil energy. Furthermore, the NaF target should provide us with a real multiplicity of TOF peaks with very little interference from recoils with the same A. As a result, we should obtain a light mass spectrum that is easily

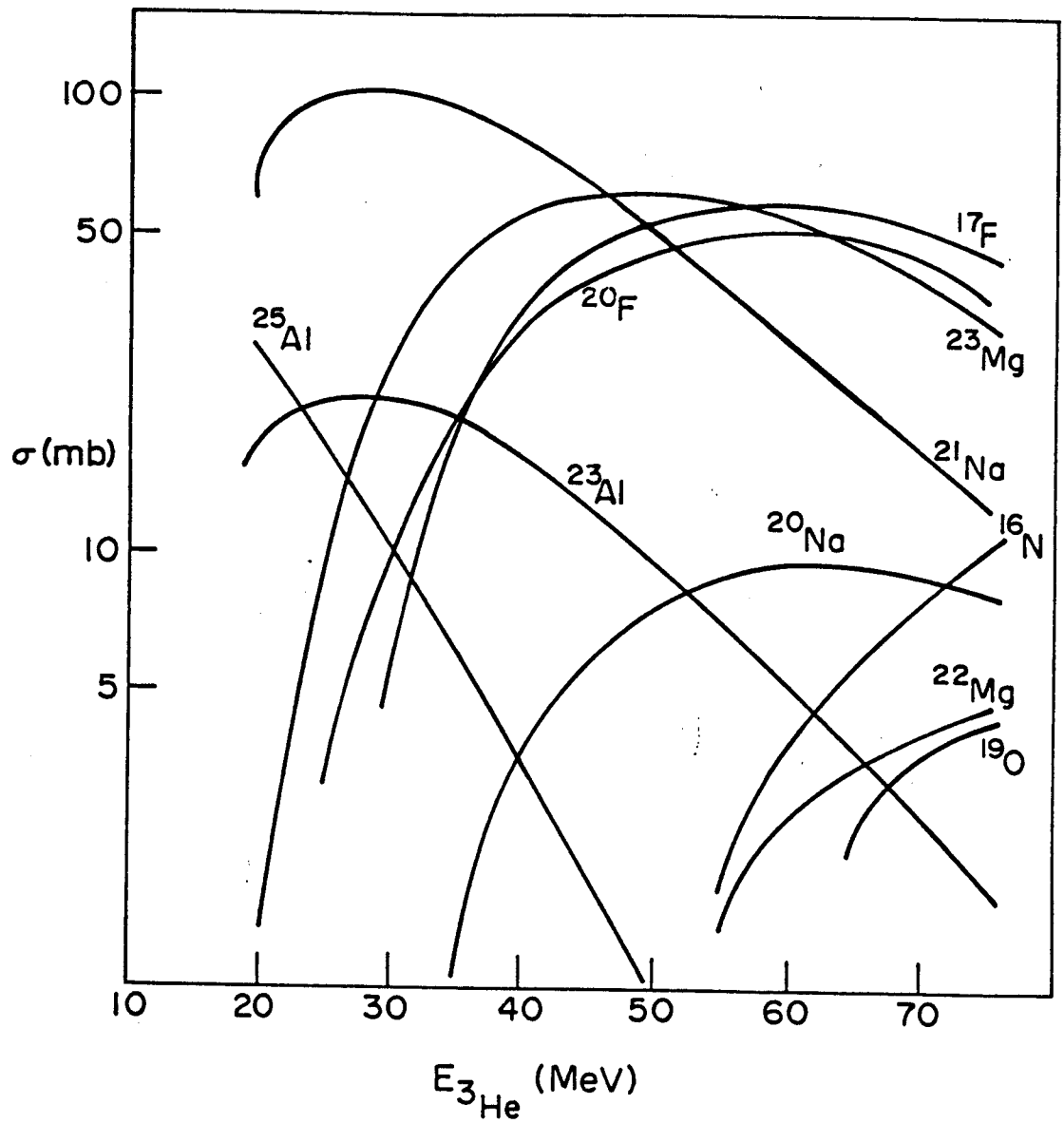

Figure 3-3. ALICE predictions for $^{23}Na + {}^{3}He$.

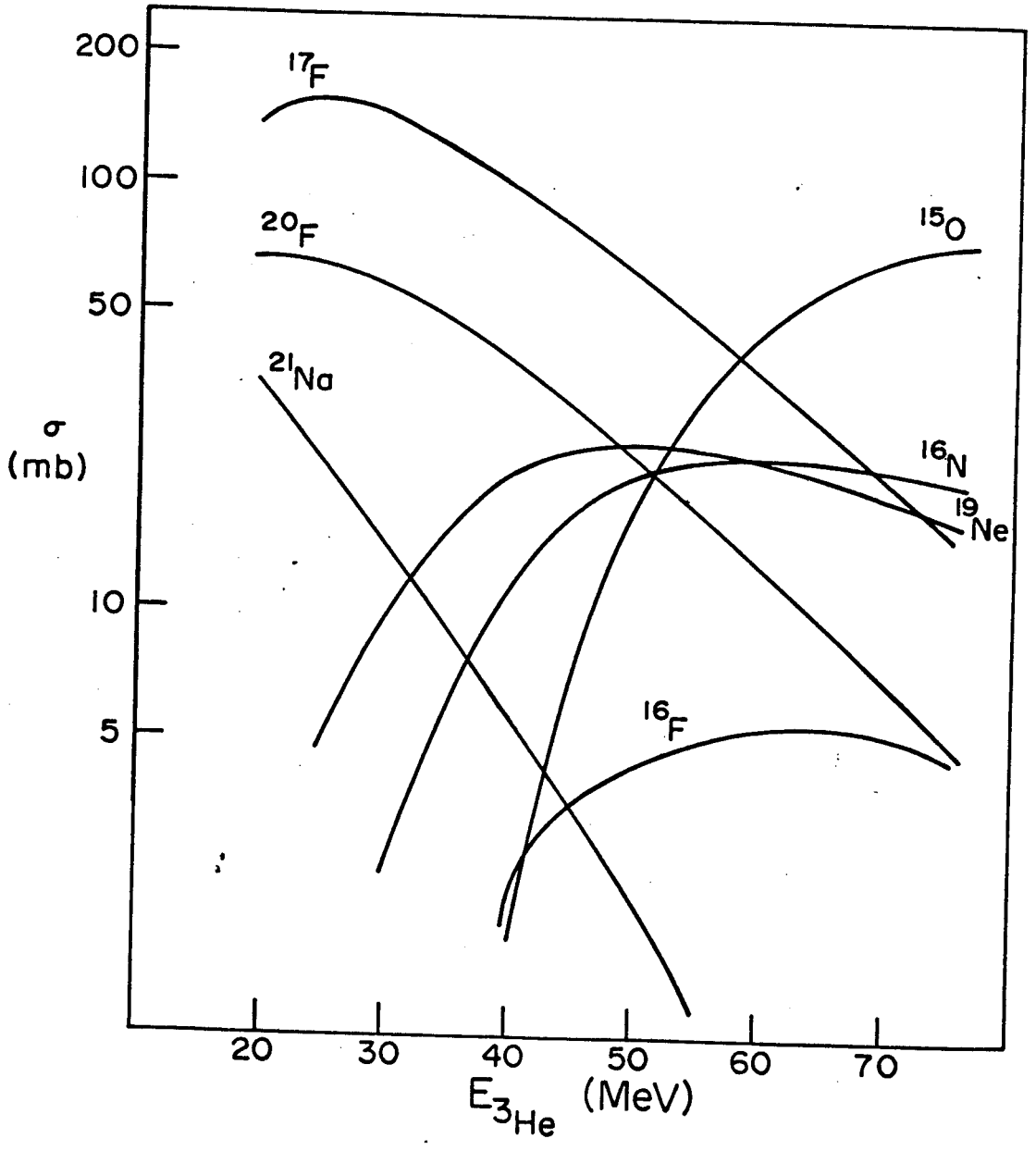

Figure 3-4. ALICE predictions for $^{19}F + {}^{3}He$.

Table III-4a. Properties of Reaction Products from ^{23}Na + 70-MeV ^{3}He.

Isotope	$t_{1/2}$ (s)	σ (mb)	E_β (MeV)	Recoil Energy (eV)
^{16}N	7.1	7	10.42	4000.
^{17}F	64.5	47	1.74	152.
^{19}O	27	4	4.82	795.5
^{20}F	11	42	7.03	1519.3
^{21}Na	3.9	16	2.52	228.2
^{22}Mg	12.1	4	3.77	441.0
^{23}Mg	7.2	37	3.03	280.1

Table III-4b. Properties of Reaction Products from ^{19}F + 70-MeV ^{3}He.

Isotope	$t_{1/2}$ (s)	σ (mb)	E_β (MeV)	Recoil Energy (eV)
^{15}O	122	68	1.74	172.0
^{16}N	7.1	23	10.42	4000.
^{17}F	64	22	1.74	152.0
^{19}Ne	17	19	2.22	203.0
^{20}F	11	7	7.03	1519.3

calibrated and contains some interesting peaks.

For this experiment we calibrated the system by first obtaining an ^{27}Al + 70-MeV ^{3}He spectrum from two hours of counting. After cleaning the collection plate, we collected data on the NaF spectrum for 1-1/2 hours with 1μA of beam current on target. Shown in Figure 3-5 is the result of the 1-1/2 h counting from the NaF target. Obviously we didn't need to worry about overlapping or interfering TOF peaks! The single mass peak occurring in the spectrum occurs exactly where the ^{23}Mg peak occurs in the Al calibration spectrum.

The results of this run are slightly disconcerting, as we mentioned that the pertinent characteristics of the reaction products seem to be almost tailored to SIEGFRIED. It goes almost without saying that we must have overlooked something important! In a few cases it might be that the real cross-section is much smaller than the ALICE predictions but it is very improbable that all but one cross-section were overestimated. The characteristic that we did not take into consideration was the transport properties of the reaction products. Except for the Mg and Na isotopes, all the reaction products are potentially volatile species that would have poor transport efficiencies. In studies using a system very similar to SIEGFRIED, H. Wolnik (Wo76) found that elements like the noble gases, Br, and I are hardly attached to the molecular clusters but still pass

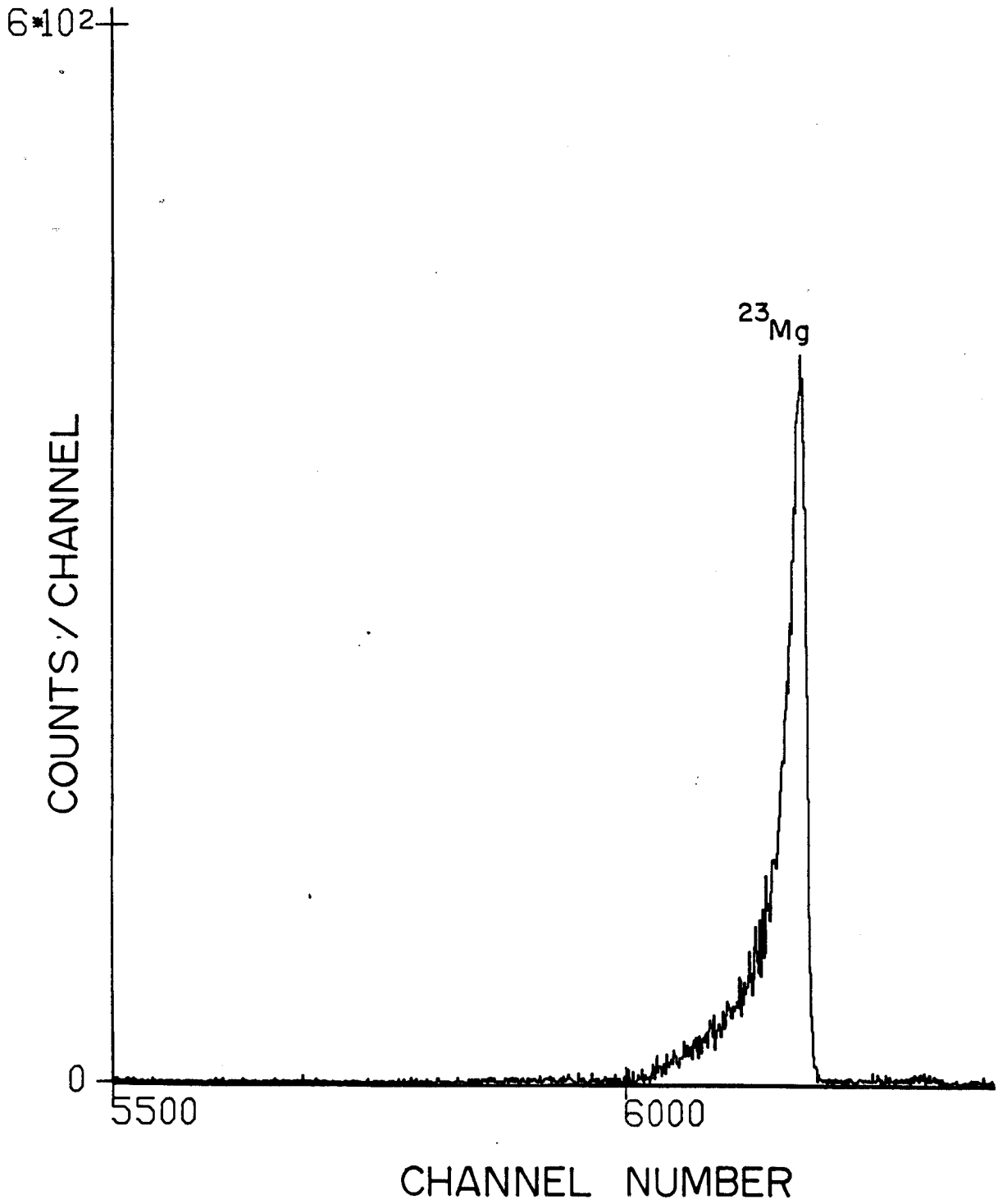

Figure 3-5. TOF spectrum for 70-MeV ^{3}He on NaF target.

through the capillary with reasonable efficiency. Nevertheless, at the collector foil it was found that the total efficiency is very low. Evidently the same phenomenon is occurring for the F, N, O, and Ne isotopes that we expected to observe.

KCl Target

The next binary compound used as target material for a possible TOF measurement was potassium chloride (KCl). For these experiments pressed powder targets on a thin Al backing were used. Figure 3-6 gives the calculated excitation functions for the $^{39}K + {}^{3}He$ reaction for the energy range 20 - 75 MeV. The excitation functions for $^{35}Cl + {}^{3}He$ are given in Figure 3-7. As can be seen from these plots we can expect a fair number of suitable reaction products especially at the higher energies for the incident ^{3}He. Another consideration favoring higher energies is the transport efficiencies of the products. The excitation functions for the $^{39}K + {}^{3}He$ reaction show that at the lower energies ($E_{^{3}He} < 50$ MeV) two chloride isotopes account for the majority of the reaction cross-section. If our experience with the NaF target taught us anything, poor transport efficiency should be expected with potentially volatile species such as chlorides. In view of these facts, we ran the KCl experiments with a beam energy of 70 MeV. Since the heaviest possible product would have a

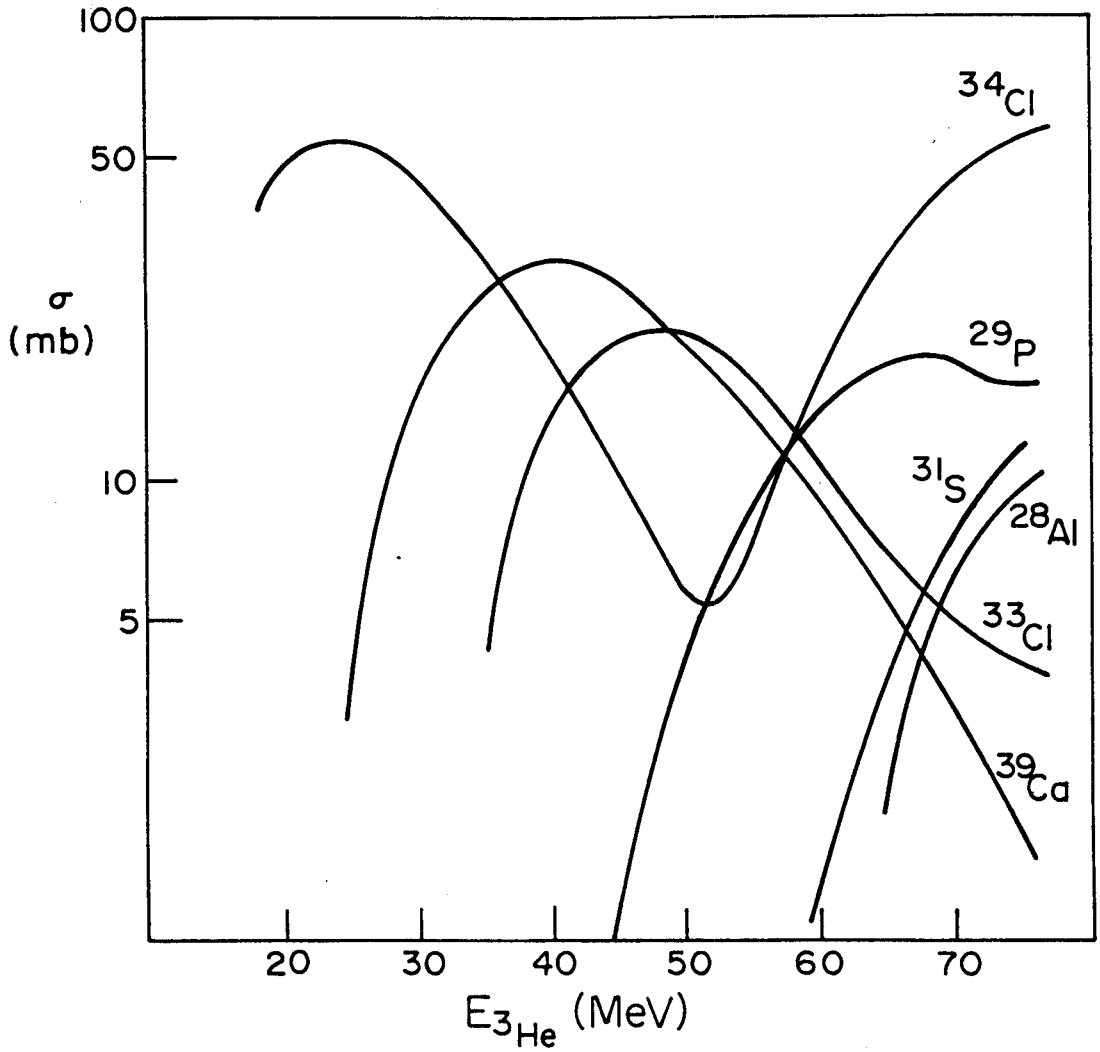

Figure 3-6. ALICE predictions for $^{39}K + {}^{3}He$.

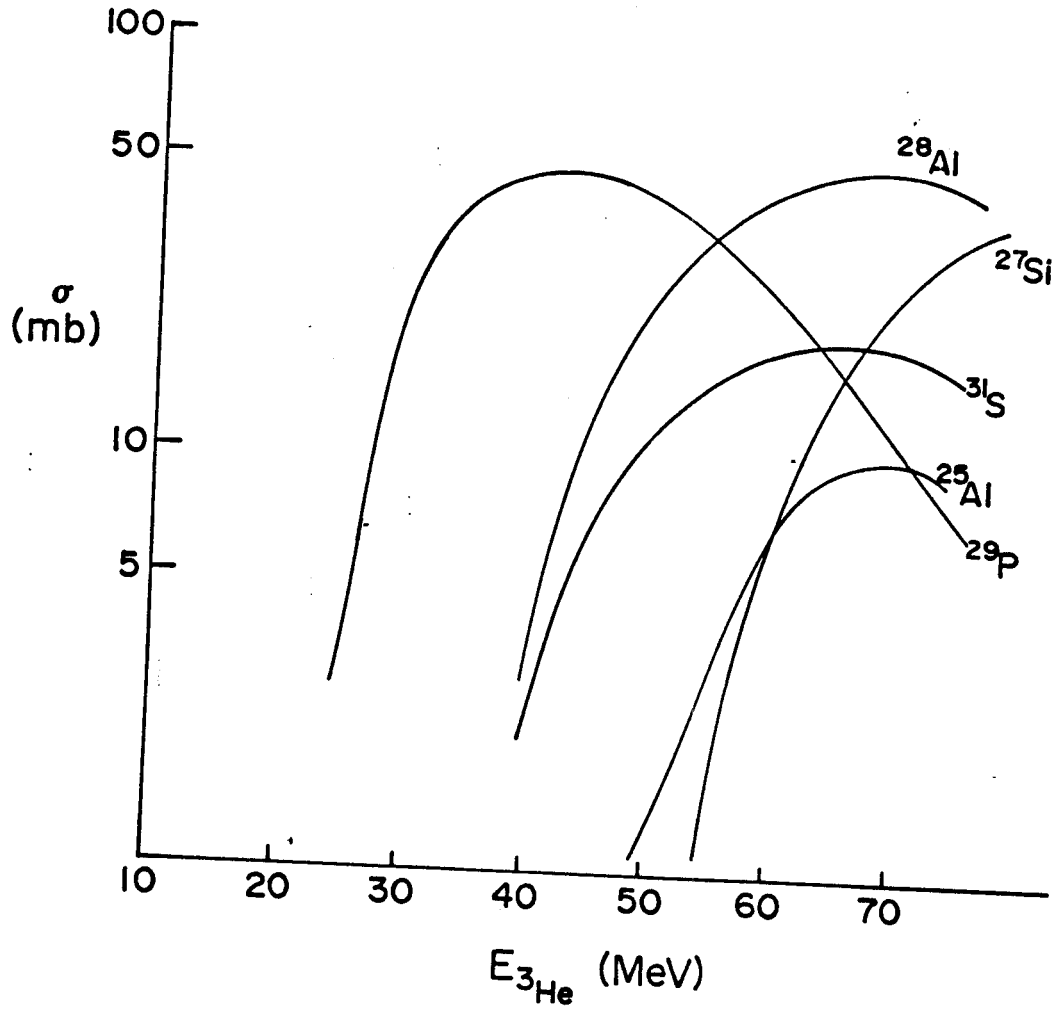

Figure 3-7. ALICE predictions for $^{35}Cl + {}^{3}He$.

time of flight of about 6.8 μsec we used an 8 μsec TAC range. This is also a convenient range for the Al Calibration spectrum.

We collected data on the KCl target for approximately ten hours. The count rate with 1μA of 70 MeV ^{3}He on target was decidedly lower than the Al calibration. Nonetheless after an hour of counting, a multiplicity of TOF peaks was observed. Using the Al calibration we determined the slope, K and the intercept, t_o for the relation:

$$TOF(CN) + K \cdot CN + t_o \qquad (3.3)$$

This allows one to calculate the time-of-flight as a function of channel number (CN). From the TOF(CN) we are able to determine the corresponding mass number from Equation 3.2, with HV = 6 kV. The accumulated spectrum is shown in Figure 3-8. Using the K and t_o from the Al spectrum and Equation 3.3 we determine the correct mass numbers. The fact that masses 26 and 27 occur at precisely the same position on both the calibration and KCl spectrum strengthens these assignments. Finally as a double check, a linear least squares fit to the assigned TOF's, as a function of channel number, was run. The results of this fit are given in Table III-5. The χ^2 for the fit was 2.3×10^{-5}.

Assignment of the correct Z corresponding to each peak in the KCl spectrum is more difficult than in the previous

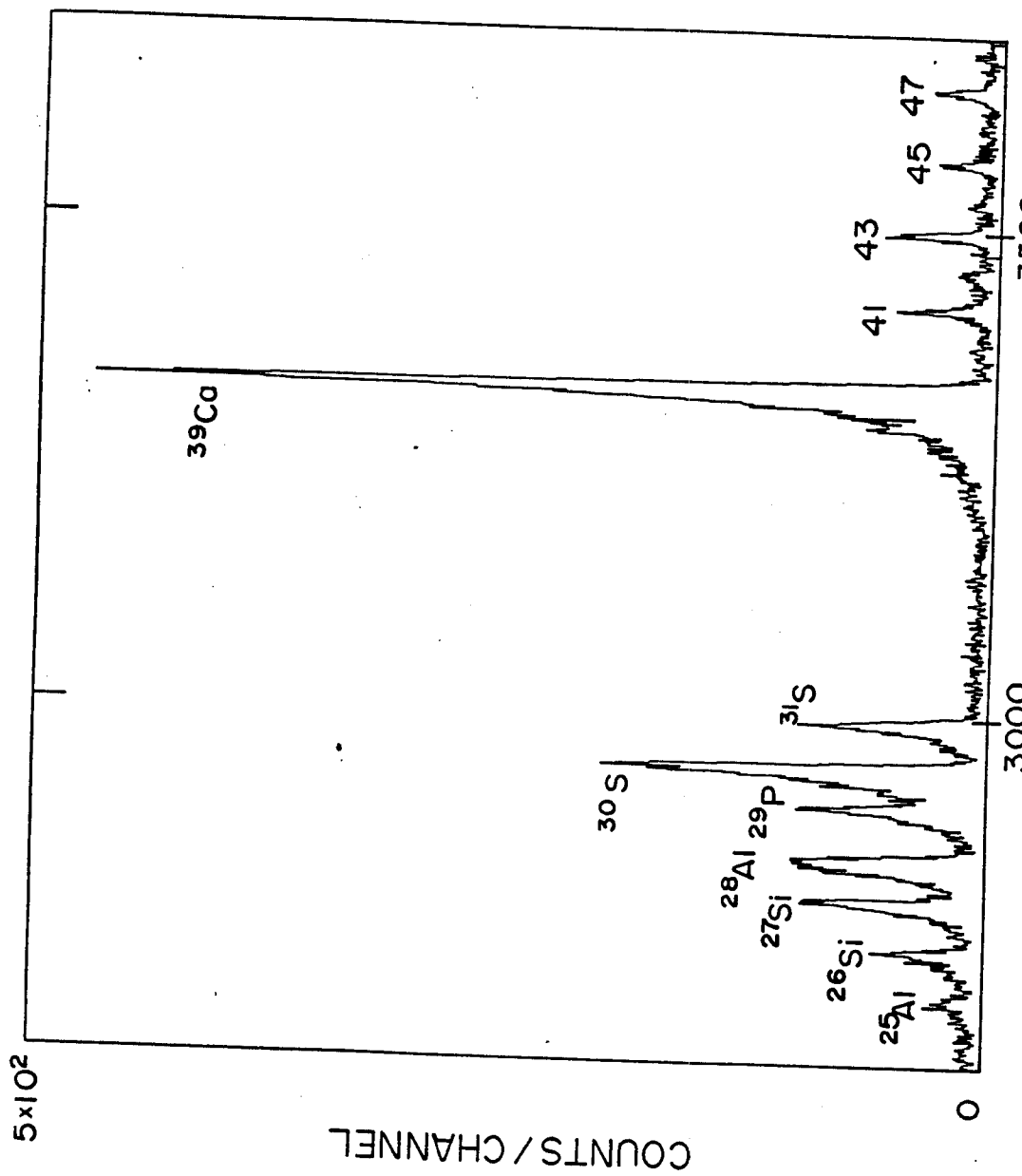

Figure 3-8. TOF spectrum for 70-MeV ^{3}He on KCl target.

Table III-5. LSQ Fit for KCl Spectrum.

A (amu)	TOF (μsec)	Centroid (Channel number)	T_{LSQ} (μsec)	Δ (μsec)	A_{LSQ} (amu)
26	5.279	5515	5.278	0.001	25.00
27	5.380	5619	5.385	-0.005	27.00
28	5.478	5704	5.437	-0.005	28.00
29	5.575	5809	5.581	-0.006	29.00
30	5.671	5892	5.667	-0.006	30.00
31	5.764	5983	5.671	-0.003	31.00
39	6.466	6668	6.467	-0.001	39.00

two cases analyzed. However, conspicuous by their absence are masses 33 and 34 which, according to the ALICE predictions, would correspond to the chloride isotopes ^{33}Cl and ^{35}Cl. This may be due to the poor transport and/or sticking efficiencies of chlorides. Recalling the results of the NaF experiment and those of H. Wolnik (Wo76) it appears that F, Cl, Br and I isotopes display similar transport properties. This chemical equivalence shown by this set of elements is not too surprising when one notes that this group makes up the halogen family. As is known from elementary chemical principles the halogens all act chemically similar in many reactions.

The mass 39 peak is fairly simple to assign since ^{39}Ca is the only possibility at that mass. The only other members, ^{39}Cl and ^{39}Ar, have poor transport efficiency, little or no cross sections and half-lives that are much too long (60 m and 269 y respectively). ^{39}Cl has a half-life of 0.86 sec and a calculated cross-section of 5 millibarns. However, the ^{39}Ca peak is easily the largest single feature in the spectrum. The collection-counting intervals used for this run were 4 sec, which may favor such half-lives but not to the extent that it would make up for such a relatively small cross-section. It seems that the ALICE calculation may well be underestimating the actual cross-section. Another intriguing point is that in the KCl spectrum it appears that ^{39}Ca has a very good transport

efficiency while in the Al and NaF spectrum ^{23}Mg has excellent transport properties. Noting that both Mg and Ca belong to the same chemical family -- the chalogens, it is intriguing to hypothesize a potential correlation between transport efficiencies and chemical families.

The peak for mass 31 is also easily identified by elimination. Among the A = 31 isobars ^{31}S is the only choice, it has a half-life of 2.7 s and a calculated cross-section of 27 millibars. The only other unstable mass 31 is ^{31}Si with a half-life of 2.6 hr which immediately eliminates it as a possible contribution.

The two mass peaks corresponding to A = 26 and 30 represent a bit more difficult task to assign. For the mass 26 we have already mentioned in the section dealing with the standard Al target that this mass may arise from either ^{26m}Al and/or ^{26}Si. The assignment of ^{26}Si is tentative at this point although evidence presented in the next chapter seems to lend weight to the assignment. The potential contribution from ^{26}Al cannot be determined at this point. A similar problem exists for the mass 30 peak. The possible candidates for this mass are ^{30}S or ^{30}P. The ^{30}P has a half-life of 3 m while the ^{30}S has a half-life of 1.4 s which is more favored by our short-time counting arrangement. On this basis the mass 30 is tentatively assigned to ^{30}S. ^{29}P has been assigned to the A = 29. It has a calculated cross-section of 28 millibarns and a

half-life of 4.4 s. The only other A = 29 isobar that is unstable is ^{29}Al which has a 6.6 m half-life and a very small reaction cross-section. ^{29}P is a $1/2^+ \rightarrow 1/2^+$ (ground state to ground state) transition by positron emission.

As in the ^{27}Al + ^{3}He TOF spectra, we find that ^{28}Al is the only reasonable contribution for the A = 28 peak. The ^{28}Al has a fairly large cross section (σ = 50 mb) from the ^{35}Cl + ^{3}He (70 MeV) reaction and a small contribution (σ = 6 mb) from the ^{39}K + ^{3}He. Again it should be pointed out that ^{28}Al differs from the majority of species observed in that it decays by β^- decay rather than positron emission.

The small peak at the position of A = 25 is due to the decay of ^{25}Al. This isotope has a half-life of 7.2 s and a calculated reaction cross-section of 10 millibarns from the ^{35}Cl + ^{3}He reaction at 70 MeV. Comparison of the cross-section and the half-life with other members of the spectrum would lead one to expect this peak to be much larger. The fault cannot lie with transport efficiency since the ^{28}Al seems to be transported very well. It may be that the calculated cross-section is too large. In studies of ^{40}Ar on ^{160}Dy, ^{164}Dy and ^{174}Yb, Y. LeBeyec *et al*. (LeB76) has found systematic discrepancies in comparisons of ALICE predictions and experimental results. The origin of these discrepancies is not well understood.

^{46}Ti Target

Towards the end of the experiment using the KCl target the count rate dropped gradually but continuously until there was no rate at all! After checking the obvious things such as the cyclotron, we opened the target chamber. A large quantity of yellowish-white powder was found to coat much of the thermalizer chamber. There was enough of an accumulation on the walls of the chamber to plug up the capillary tube. This served to block the transport of recoil products and so the count rate drop-off occurred. The origin of this powder is not known.

For our next experiment we decided to use a natural Ti foil target as a possible means of avoiding the aforementioned problem with the powder generated in the thermalizer chamber. Although the ^{48}Ti isotope accounts for part of the target material ALICE calculations indicate that this isotope would not give rise to any species that would be measurable by SIEGFRIED. This is also true for the ^{47}Ti and ^{49}Ti isotopes. Shown in Figure 3-9, are the calculated cross-sections for the reaction products for ^{46}Ti + ^{3}He. In Table III-6 are given the associated half-lives and cross-sections for production with a 70-MeV ^{3}He beam. The ^{45}Ti, with a half-life of 3 hr, is included because the other mass 45 predicted is ^{45}V which is so far unknown. If we see a peak corresponding to mass 45 in our TOF

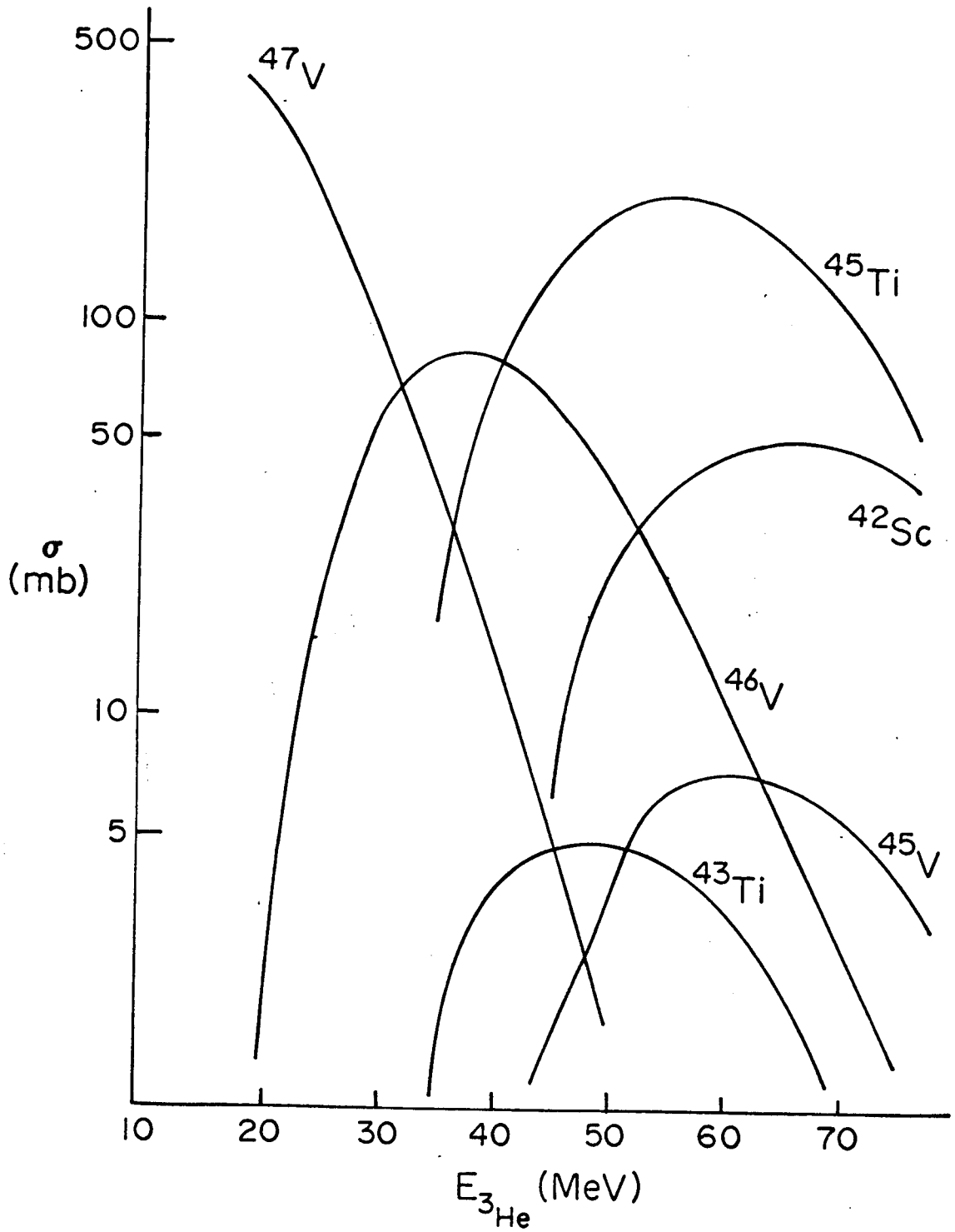

Figure 3-9. ALICE predictions for $^{46}Ti + {}^{3}He$.

Table III-6. Properties of Products of ^{46}Ti + 70-MeV ^{3}He.

	$t_{1/2}$	σ (mb)
^{42}Sc	0.7 s	50
^{43}Ti	0.6 s	1.1
^{45}Ti	3.0 h	110.
^{45}V	Unknown	5.5
^{46}V	0.4 s	3.0
^{47}V	33 m	0.0

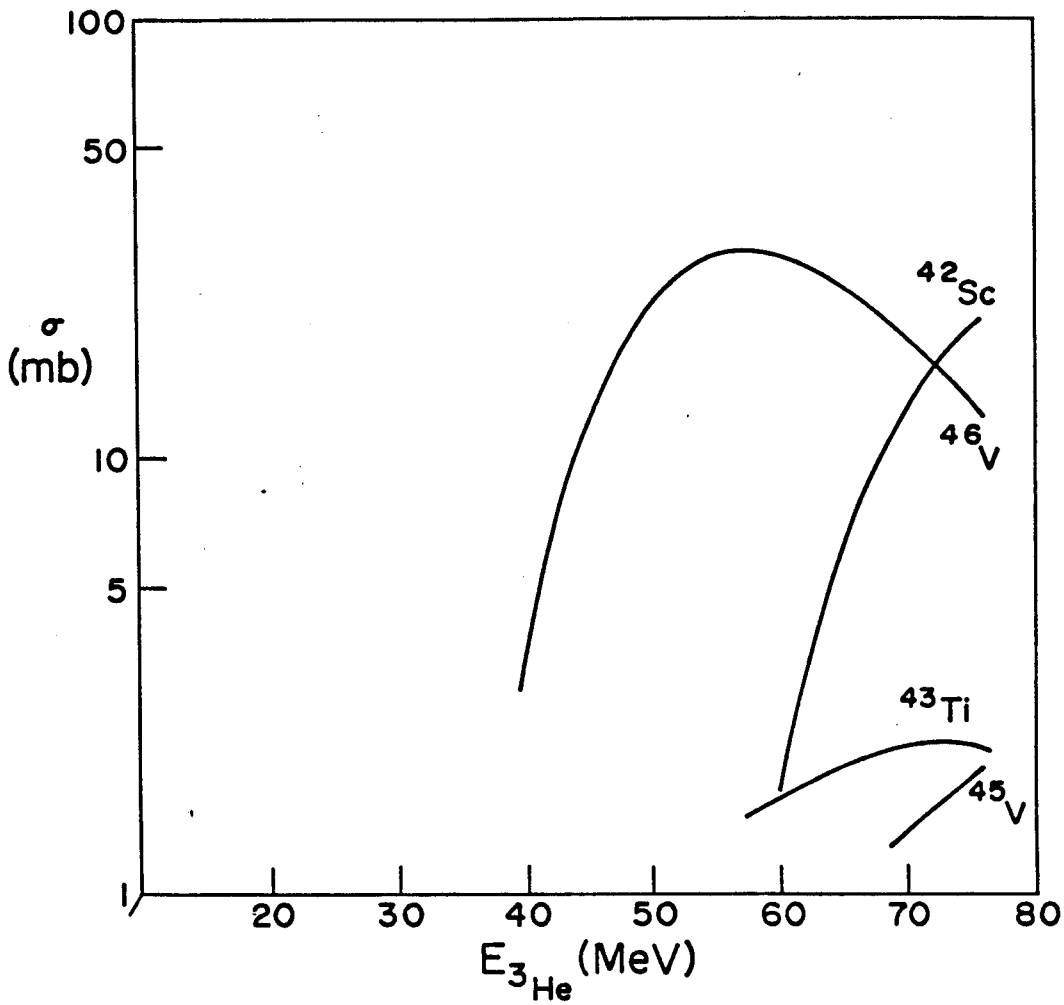

Figure 3-10. ALICE predictions for $^{47}Ti + {}^{3}He$.

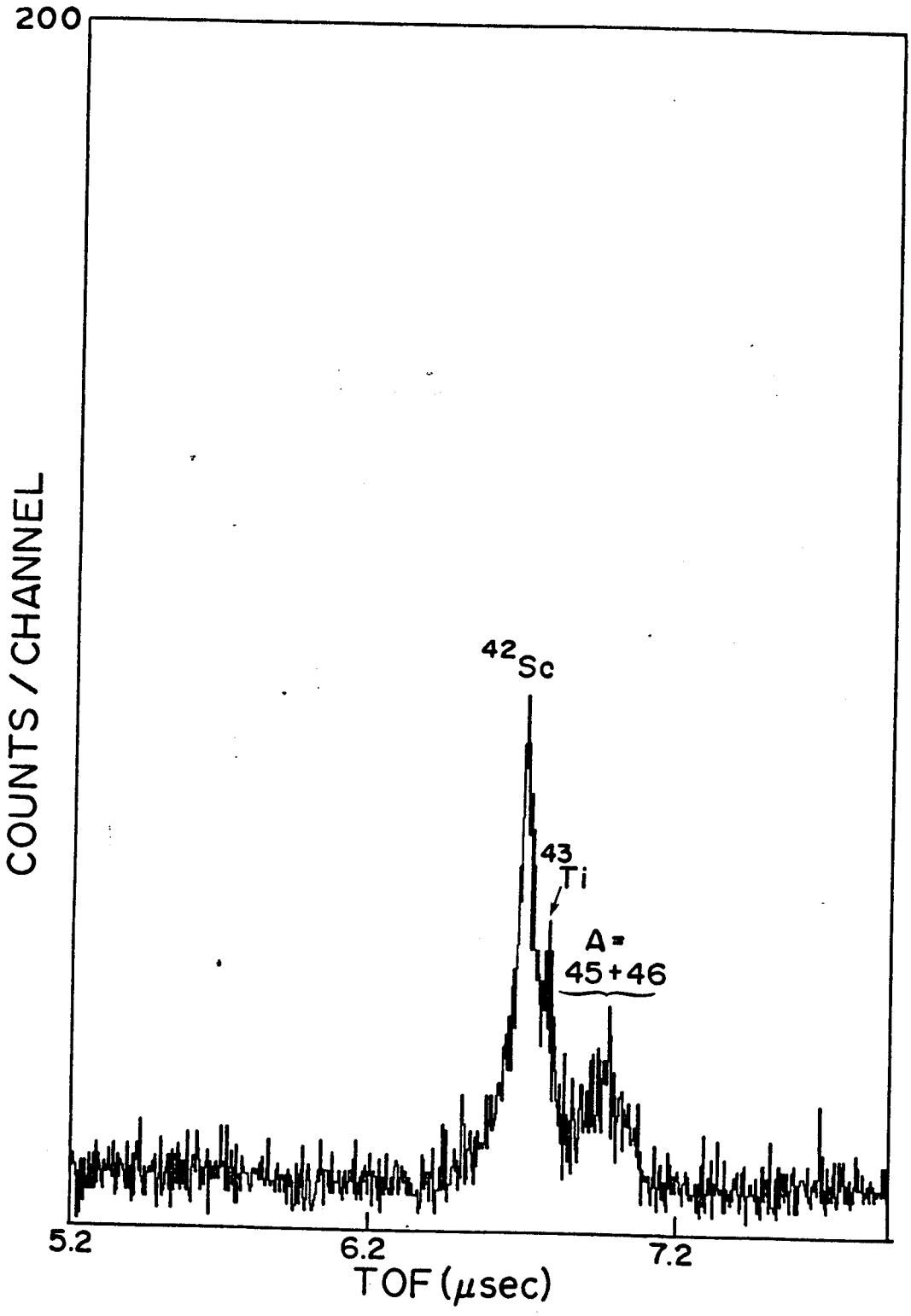

Figure 3-11. TOF spectrum for products of 70-MeV ^{3}He on Ti target.

from a combination of two masses, 45 and 46. The mass 44 should occur in the valley between the ^{43}Ti shoulder and this broad distribution. A mass 47 recoil would occur at 7.1 s which is slightly above the mass conglomerate. Since the two masses peaks are so poorly resolved we have no information on the strengths of the individual peaks but there are two mass peaks in the wide distribution. ^{46}V is the most probable source of the mass 46 contribution to the broad peak. Among the A = 46 isobars it is the only one with a suitable half-life and ALICE predictions indicate that it has a 3 mb production cross-section. As for the A = 45 contribution there are no convincing prospects. According to the ALICE calculations ^{45}Ti should be produced in relatively large amounts. However, the 3 hr half-life of this isotope is very unfavorable. The other potential candidate, ^{45}V has a cross-section of roughly 6 mb but the half-life of this isotope is unknown. ^{45}V has so far only been observed in charged-particle measurements (Mu76).

Nickel + ^{3}He

A natural nickel foil was used as the target for our next experiment. This represents a step of about ten to twelve amu from the titanium foil target previously employed. This allows us to investigate the performance of our system in a slightly heavier mass region. The isotopic composition of the target is as follows:

^{58}Ni (68%), ^{60}Ni (20%), ^{61}Ni (1.25%), ^{62}Ni (8.7%) and ^{64}Ni (1.1%). ALICE calculations were performed for all the constituents. The main contribution to the reaction cross-section was from the ^{58}Ni isotope. The results of the ALICE calculations for ^{58}Ni + ^{3}He are shown in Figure 3-12. Note that the ^{55}Ni isotope has a reasonable production cross-section between 35 and 60 MeV. This particular isotope is as yet poorly known but the ALICE calculations predict a 7 mb production cross-section at 45 MeV. Also at this energy we might expect a fairly strong ^{54}Co peak to appear in our TOF spectrum.

For our first run with the Ni target, a 45-MeV ^{3}He beam was used. Since the recoil mass products were in the range of 50-60 amu, the TAC was run on the 10 μsec range. For the counting arrangement it was decided to collect activity and then count for twenty-second intervals since the predicted products have half-lives in the tens of seconds to minutes range. We collected statistics for approximately four hours. This was interrupted by frequent problems with the cyclotron. For the start detector we used a NaI(Tl) detector, which for annihilation radiation is as efficient as the plastic scintillator. Shown in Figure 3-13 is the TOF spectrum resulting from the ^{58}Ni + 45 MeV ^{3}He run. As was expected, a large peak occurs for ^{54}Co. At slightly earlier TOF's there appears to be a triplet of peaks centered on A = 53. We have

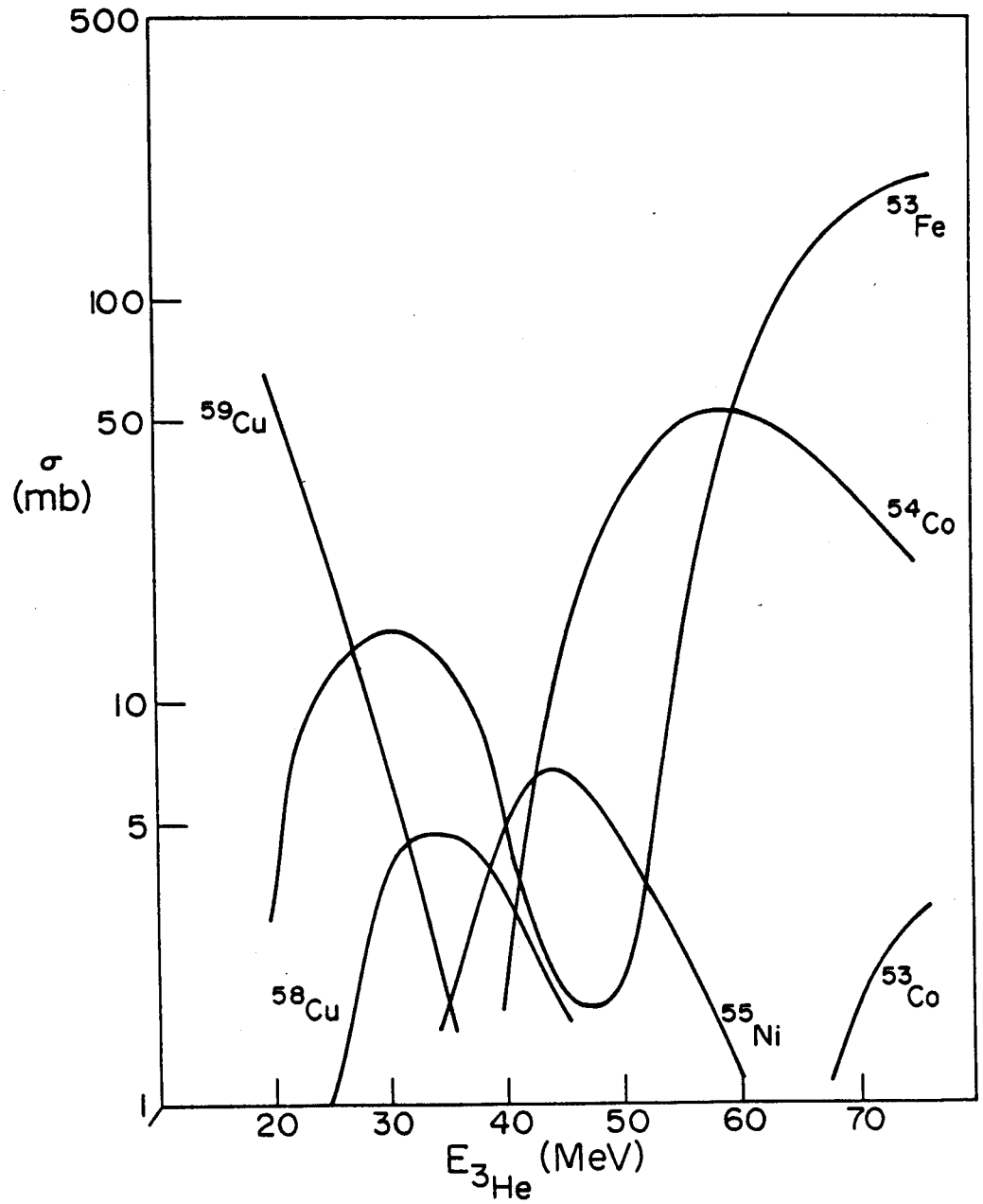

Figure 3-12. ALICE predictions for $^{58}Ni + {}^{3}He$.

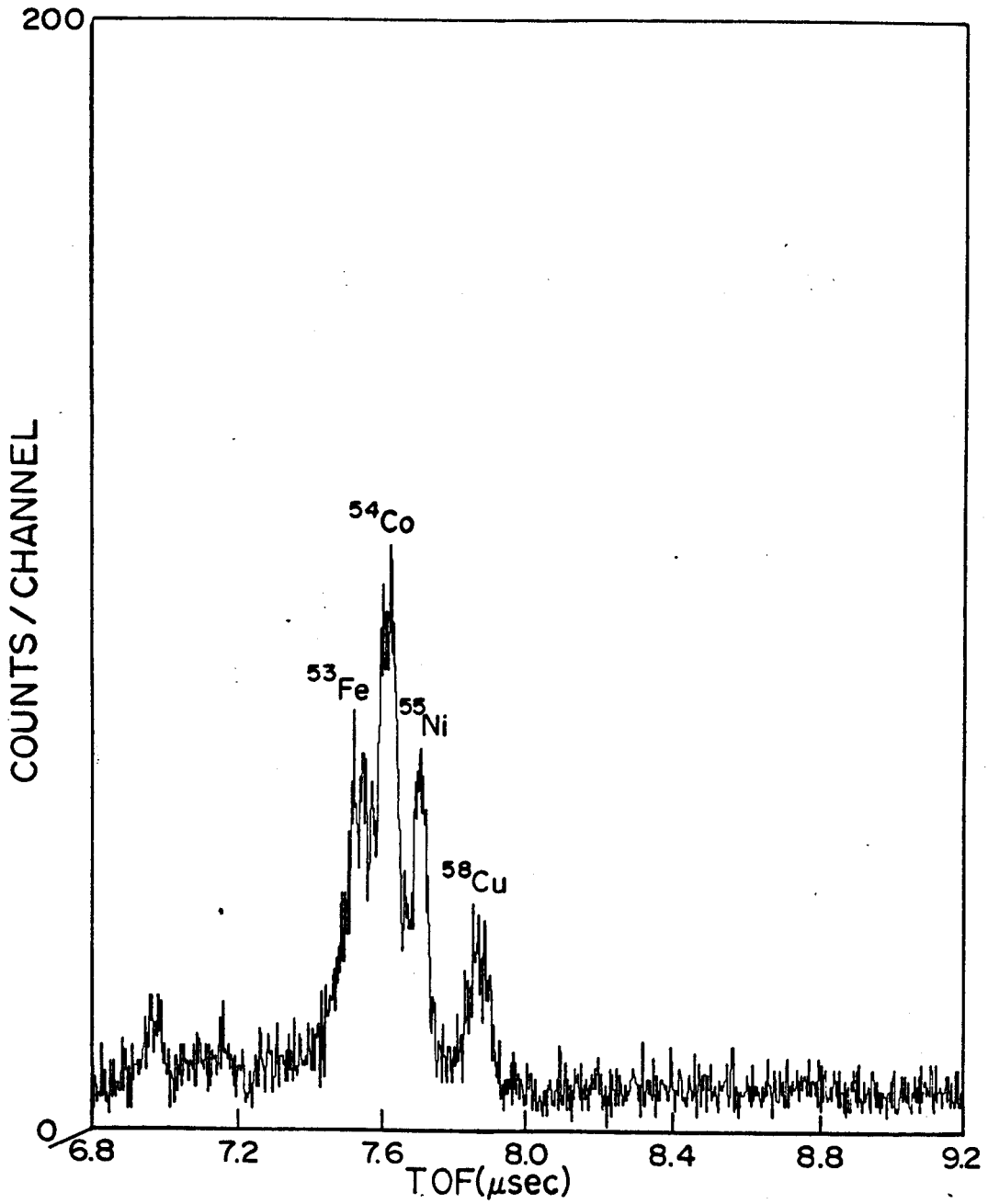

Figure 3-13. TOF spectrum for products of 45-MeV ^{3}He on Ni target.

tentatively assigned this group to ^{53}Fe which decays to states in ^{53}Mn which immediately γ-decay to the ground state. The effect of the γ-decay on the recoil TOF may be reflected in this splitting. Just beyond the ^{54}Co there is a fairly large peak at the position of A = 55. We have tentatively identified this as ^{55}Ni. However, this cannot be taken as an unequivocal assignment, from our experience with the ALICE calculations it would seem rash to place too much confidence in the predictions. The ^{55}Cr isotope has a very small production cross-section according to calculations but it has a reasonable half-life (3.5 m) and may be a possible source of the mass 55 peak. The assignment of ^{55}Ni to this peak should be taken as tentative at this point.

The next feature in the TOF spectrum of Figure 3-13 is a smaller, broad peak whose centroid corresponds to mass 57.5. The peak probably has two components: A = 57 and 58. However it is not really possible to resolve this peak. From the ALICE calculations we would expect some production of the ^{58}Cu isotope which has a very large decay energy, (Q_{EC} = 8.57 MeV) and positron decays to various levels in ^{58}Ni with a half-life of 3.2 s. The large decay energy results in a maximum recoil energy of 600 eV, which is 10% of the 6 kV acceleration voltage and may explain the distinct broadening seen in this peak. If there is an A = 57 component to this peak it is very difficult to

rationalize. The only possibility amoung the A = 57 isobars is ^{57}Mn but there is no reasonable reaction of ^{58}Ni + ^{3}He to produce ^{57}Mn at these energies.

After a day of running we were forced to stop due to difficulties with the cyclotron. When we came on-line again it was decided to run at 70-MeV He on the same Ni target. The TOF spectrum shown in Figure 3-14 is the result of approximately 8 hrs of counting. As expected from the ALICE predictions the mass 53 peak is now the largest feature due to the appreciable increase in cross-section for ^{53}Fe and the onset of production of ^{53}Co. The ^{54}Co peak is correspondingly reduced as suggested by calculations. At the position of A = 55 there is a small peak on the shoulder of the ^{54}Co peak. On the basis of the previous run with the Ni target we assign ^{55}Ni to this weak peak but again urge caution in this assignment. Rather unexpected is the smaller, partially resolved doublet at the position of A = 58 and 59. The ALICE calculation for ^{58}Ni + ^{3}He indicate both ^{58}Cu and ^{59}Cu to have appreciable cross-section at much lower energies. However, ^{62}Ni, (4% of natural) may be a potential source for these species. In the absence of any other reasonable species we tentatively assign ^{58}Cu and ^{59}Cu to this doublet.

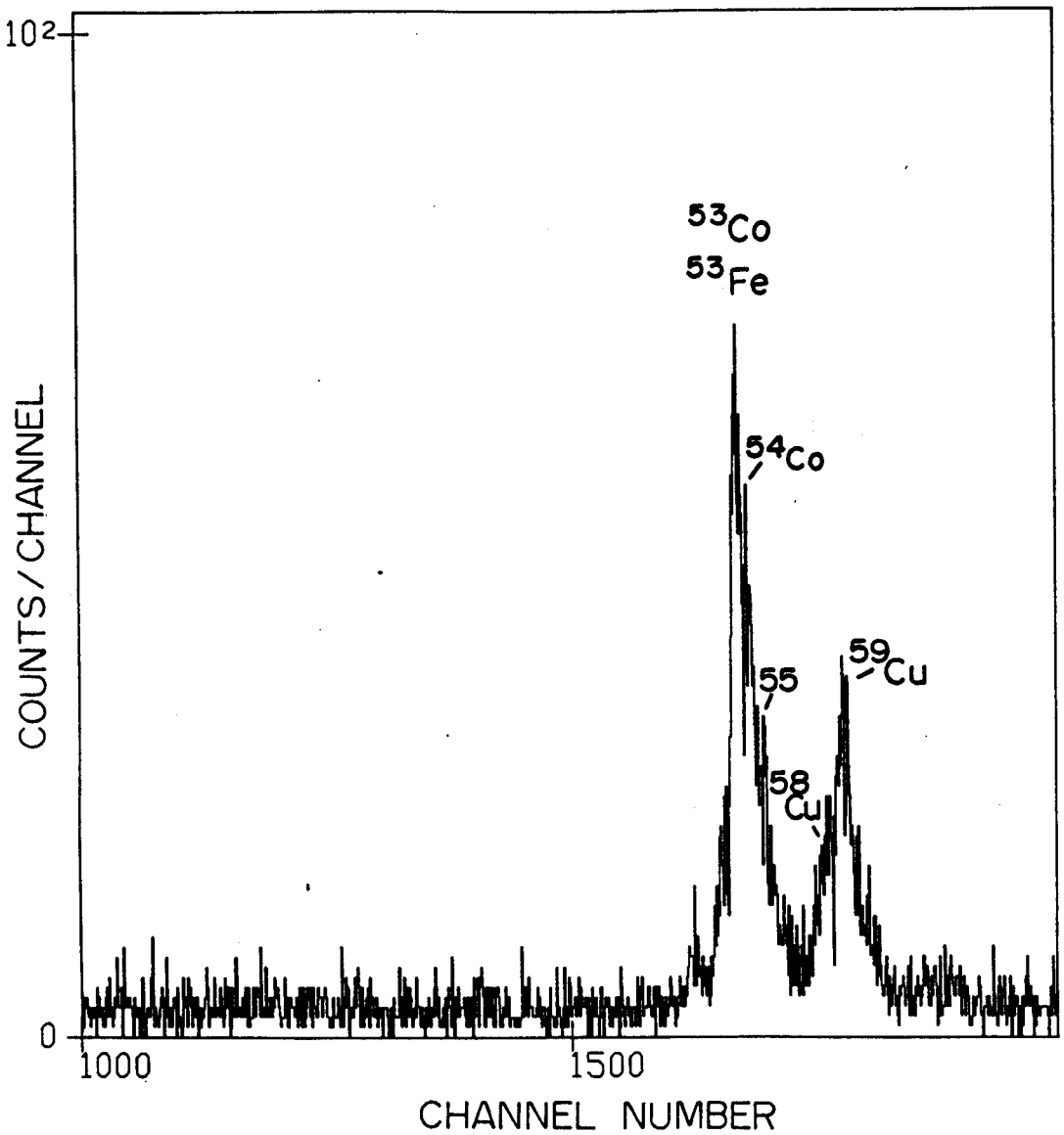

Figure 3-14. TOF spectrum for products of 70-MeV ^{3}He on Ni target.

Al γ-Mass Coincidence

The use of a γ ray detector for the start signal of a TOF event is an attractive alternative to the plastic scintillator used heretofore. As is well-known, γ transitions are discrete as compared to the continuum resulting from β transitions. It is much easier to determine the energy of a γ transition than it is to measure the end-point energy of a β decay. As a result it is more useful to label a mass peak with a given γ ray energy.

In order to demonstrate the feasibility of such experiments, we decided to use a NaI (Tl) scintillator as the start detector for an ^{27}Al + 70 MeV ^{3}He experiment. As discussed earlier, this particular reaction and the resulting TOF spectrum are familiar and well understood from many earlier experiments. Since the majority of decay products we see in the spectrum result from positron emission, annihilation radiation will provide effective start signals for any ground state to ground state transitions.

The ^{27}Al target was the same one used for the experiments described in Section I, as were the beam energy (70 MeV) and TAC scale (8 μsec). The amount of beam on target was roughly 0.5 μA and data were collected for 2.5 hrs. The resulting TOF spectrum is shown in Figure 3-15. The two most striking features of this spectrum are the background and the peak distribution as compared to the

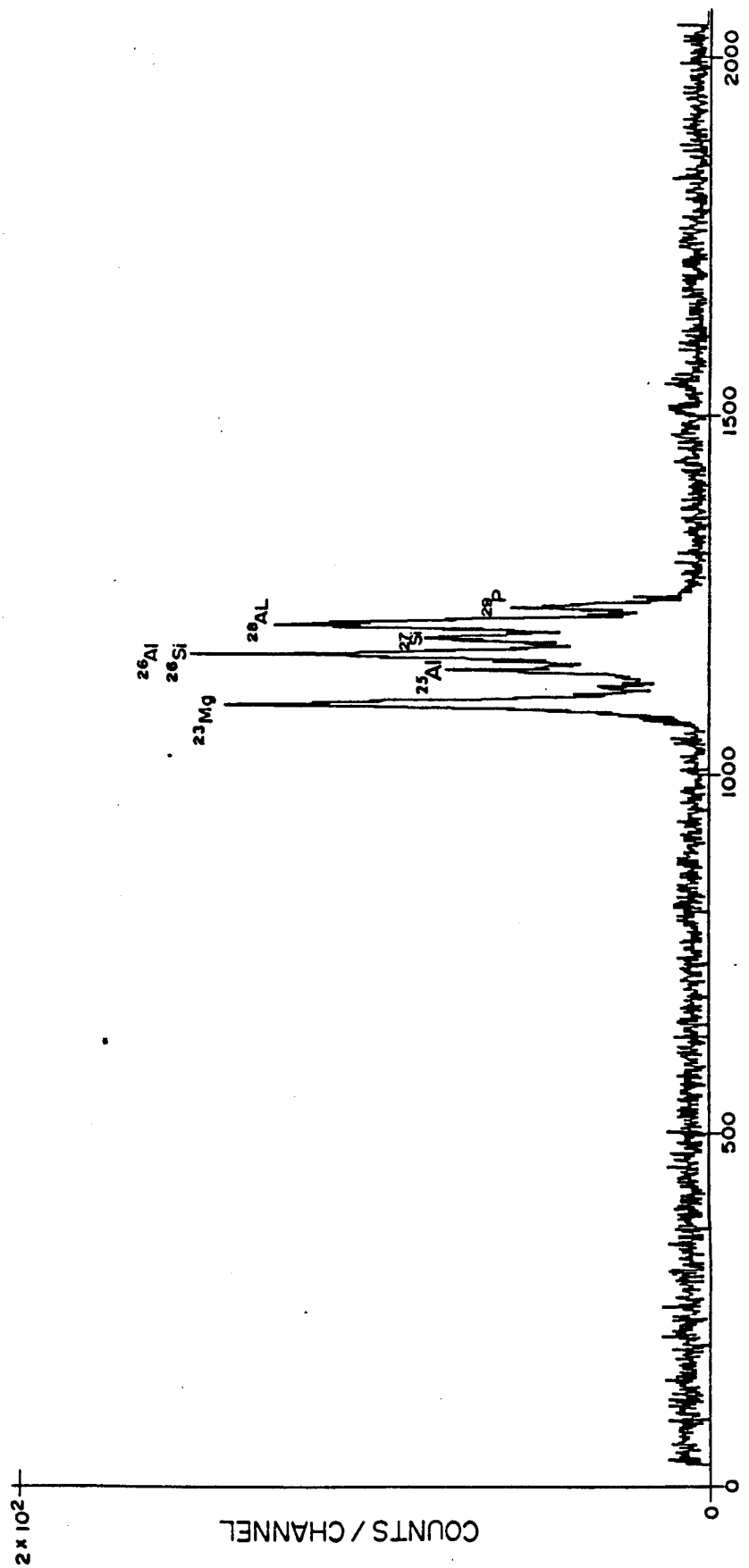

Figure 3-15. TOF spectrum for Al + 70-MeV ^{3}He reaction products (using NaI(Tl) as start detector).

same spectrum using a plastic scintillator for the start detector. This is especially noticeable in the case of the ^{23}Mg peak which in all spectra resulting from plastic scintillator start signals is easily the largest peak in the set by a factor of two. In the γ-mass spectrum of Figure 3-15, this is obviously not the case. Actually the mass 26 peak is now the larger peak. This is not well understood at this point. One would expect the only differences in distributions to occur as a result of large differences in positron energies. The NaI(Tl) scintillator will detect positrons by their annihilation radiation which occurs once the positrons have been stopped and the scintillator should be more effective stopping lower energy positrons. Accordingly we would expect NaI(Tl) scintillator to be more sensitive to lower energy positron. However, in the case of the ^{23}Mg and ^{26}Al, thepositron energies are about the same. If the ^{26}Si is the main component its positron energy is 0.8 MeV greater than the ^{23}Mg which is in conflict with the efficiency argument.

The highest background observed is probably due to the large number of random start signals resulting from bremsstrahlung and Compton scattering. For a 3 MeV electron passing through stainless steel, energy losses due to bremsstrahlung is about 11% of the loss due to ionization (Si66). Since there are always some residual gas molecules in the TOF chamber striking the CEMA's and the

NaI(Tl) scintillator is very efficient for low energy radiation such as bremsstrahlung the higher background is expected.

Figure 3-16a is the NaI(Tl) spectrum associated with the TOF spectrum of Figure 3-15. Figure 3-16b is the spectrum after a 3-channel smoothing was performed to accentuate details of the spectrum. Since the majority of decays are positron emitting ground state to ground state transitions the very large 511 keV peak is an expected feature. The large "hump" preceding the 511 keV peak is due to a combination of Compton scattering events and bremsstrahlung. The small peak at 1780 keV is due to the γ-transition following the decay of ^{28}Al.

$^{144}Sm + {}^{3}He$

As an example of a heavier mass TOF spectrum, we decided to use a $^{144}Sm_2O_3$ target. This was available in the separated isotope form (99%). The ALICE calculations for the products of $^{144}Sm + {}^{3}He$ are given in Figure 3-17. The predicted cross-sections are much larger than any of the previous experiments discussed here. Since we expect recoils in the region of 150 amu, the minimum TAC range, with 6 kV acceleration, is 13 μsec. To be safe we used a 20 μsec TAC range. One difficulty with such a long TAC range is that we have cut down on our resolution -- there are more nsec per channel in this case. Also working

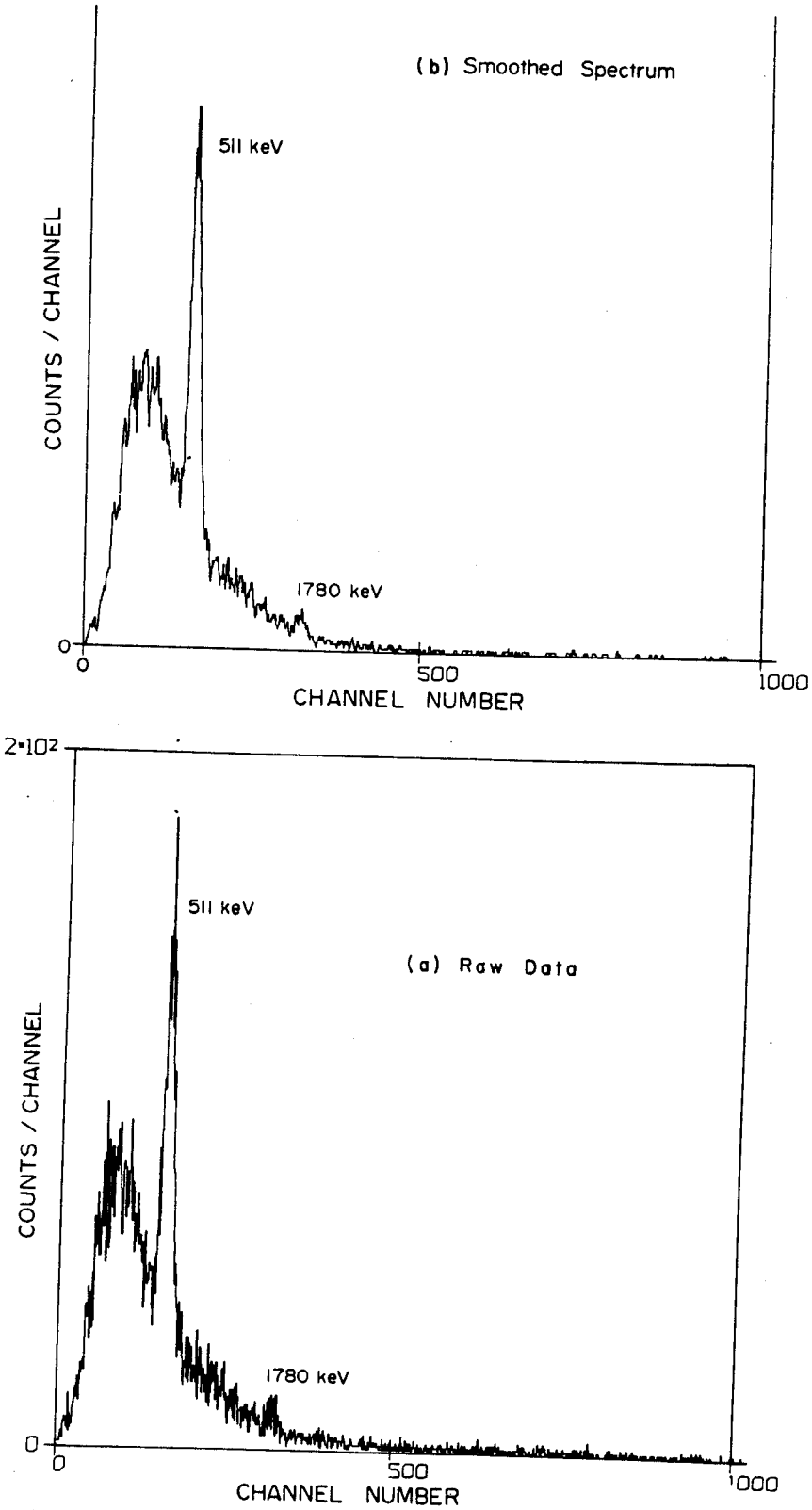

Figure 3-16. NaI γ-spectrum in coincidence with spectrum of Figure 3-15.

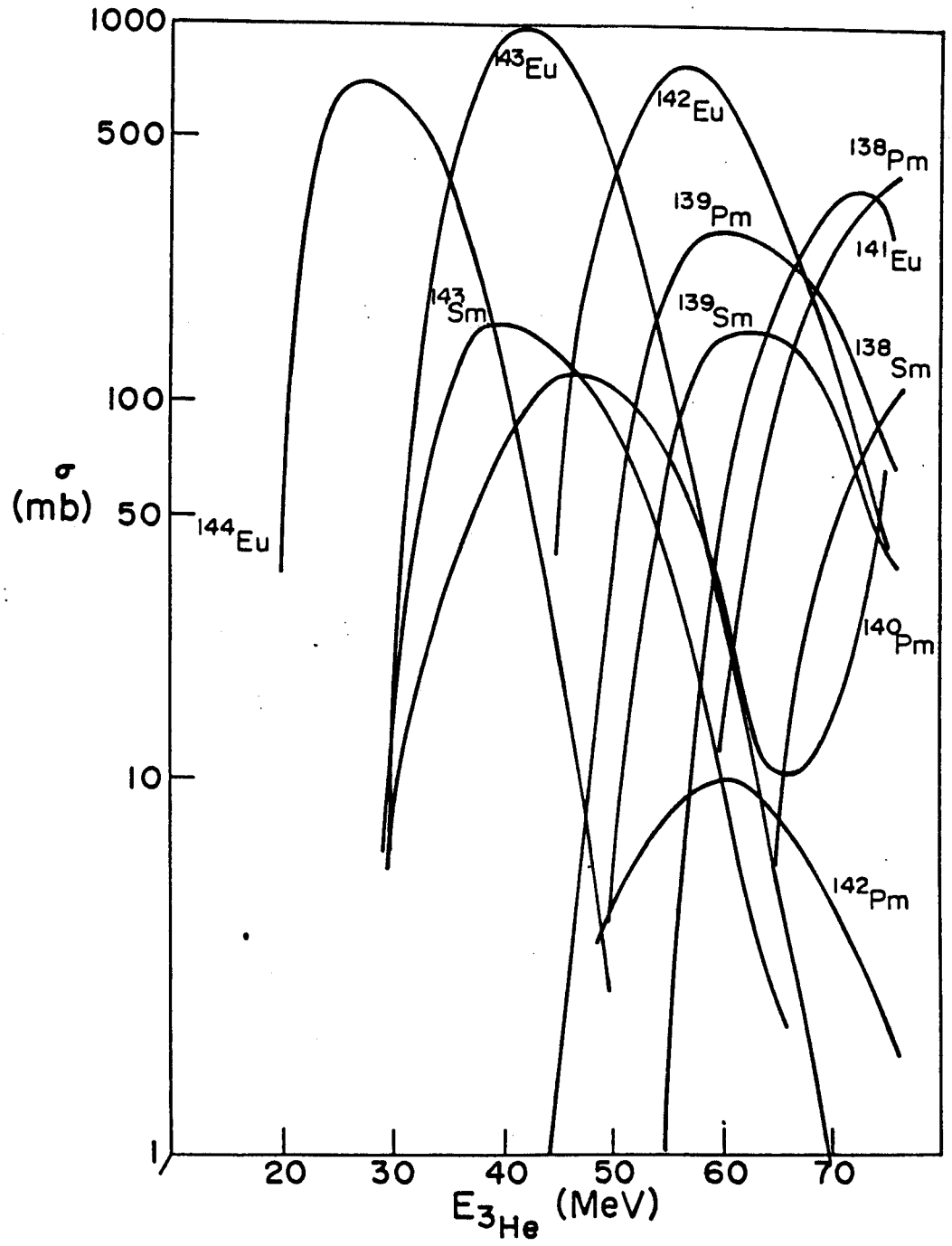

Figure 3-17. ALICE predictions for ^{3}He + ^{144}Sm.

against us in the heavier mass region is the fact that the differences in TOF's for successive masses are decreasing so the peaks will tend to bunch together, making it difficult to resolve adjacent mass peaks. Normally one way to alleviate this problem is to use a very precise delay for the start signal for the TAC. This allows one to use a shorter TAC range and thereby expand the region of interest. This effectively increases the resolution substantially. In light of these considerations the Precision Digital Delay Model 7030 was bought from Berkeley Nucleonics Corporation. This module is essentially a sophisticated, highly stable delay line. Unfortunately, the reliability of the box is significantly lower than its other qualities. It was malfunctioning before this run and was not used. It was deemed worthwhile to do the experiment for a number of reasons. First, in a number of runs the coincidence rates were very low making complex experiments of interest impossible. To have a rough idea of the collection rate would be very helpful for planning further experiments. Also of interest was how serious is the problem of mass peak bunching; possibly the adjacent peaks "ride" on one another's tails yet are still resolvable. Lastly, in view of the importance of the transport and sticking efficiencies as established earlier it seemed worthwhile to find out if we would "see" anything in reasonable quantities.

Shown in Figure 3-18 is the TOF spectrum resulting

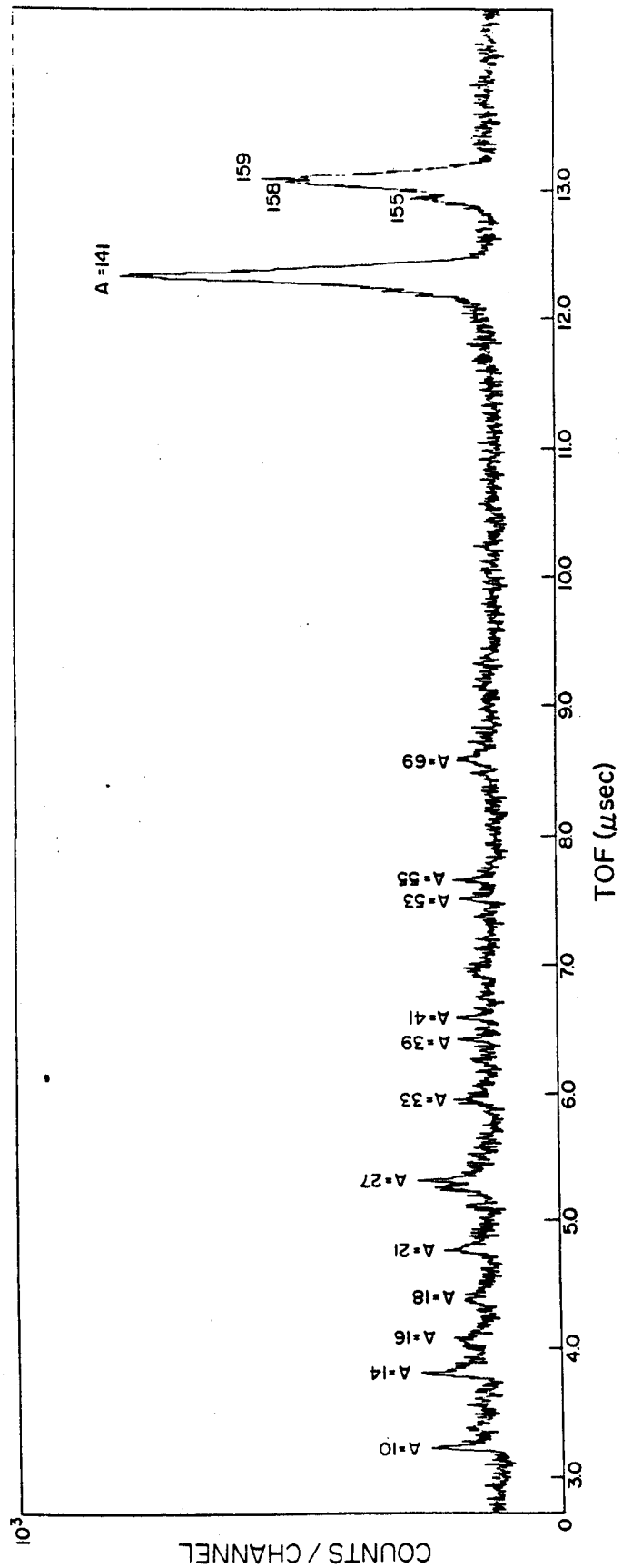

Figure 3-18. TOF spectrum for products of 70-MeV ^{3}He on ^{144}Sm target.

from two hours of counting of the products from the $^{144}Sm + {}^{3}He$. At the long TOF end of the spectrum are two large, very broad peaks. The first of these two peaks occurs at the position of A = 141 but, as expected it is broad enough to encompass masses 138-144. Obviously it is impossible to resolve meaningfully the individual mass components of this peak. The only thing one can surmise from this feature of the spectrum is that we have measured the TOF's of a number of species with masses between A = 138 and 144. The second large peak shown in the spectrum seems to allow some resolving of the individual components. The masses most prominent in the peak correspond to 155, 158 and 159. Yet how can such masses result from a compound nucleus of maximum mass of 147? A number of experimenters (Ne78), (Ne79), (Wo77) have observed very similar phenomena in their TOF spectra and attribute the heavy mass peaks to molecular species that are somehow volatilized from the collector surface. The fact that the second large mass peak corresponds to the earlier masses + 16 amu, which is the mass of ^{16}O, suggests that the components of this peak are the same as the lighter masses except there is an attached oxygen (A = 16).

In the remainder of this spectrum can be found a large number of small TOF peaks that are not explained as simply as the peak centered around A = 158. They may correspond to radicals ($C_nH_mO_k$, etc.) that have been ionized by collision with the primary recoils.

CHAPTER IV

RECOIL ENERGY FITTING

A close inspection of the mass time-of-flight peaks acquired with SIEGFRIED reveals a number of phenomena that are not exactly what one would expect for simple measurement of an ion flight time. Referring to Figures 4-1, 3-1, and 3-5, it is easy to notice that the peaks are all rather wide -- much wider than any electronic timing contributions might account for, as will be shown. Perhaps more striking to the eye is the very peculiar shapes exhibited in the spectra; all have long nearly exponential tails on the low time side, implying some mechanism that suppresses higher energy events and favors longer TOF events.

It seems reasonable to view the source of the recoils as a thin film deposited on the collecting plate, since massive clusters provide the means of transport of the product nuclei from the target area. A simple picture of recoils passing through a surface layer of cluster deposit seems to favor a higher probability of escape for high energy recoils than for low energy recoils. However, higher

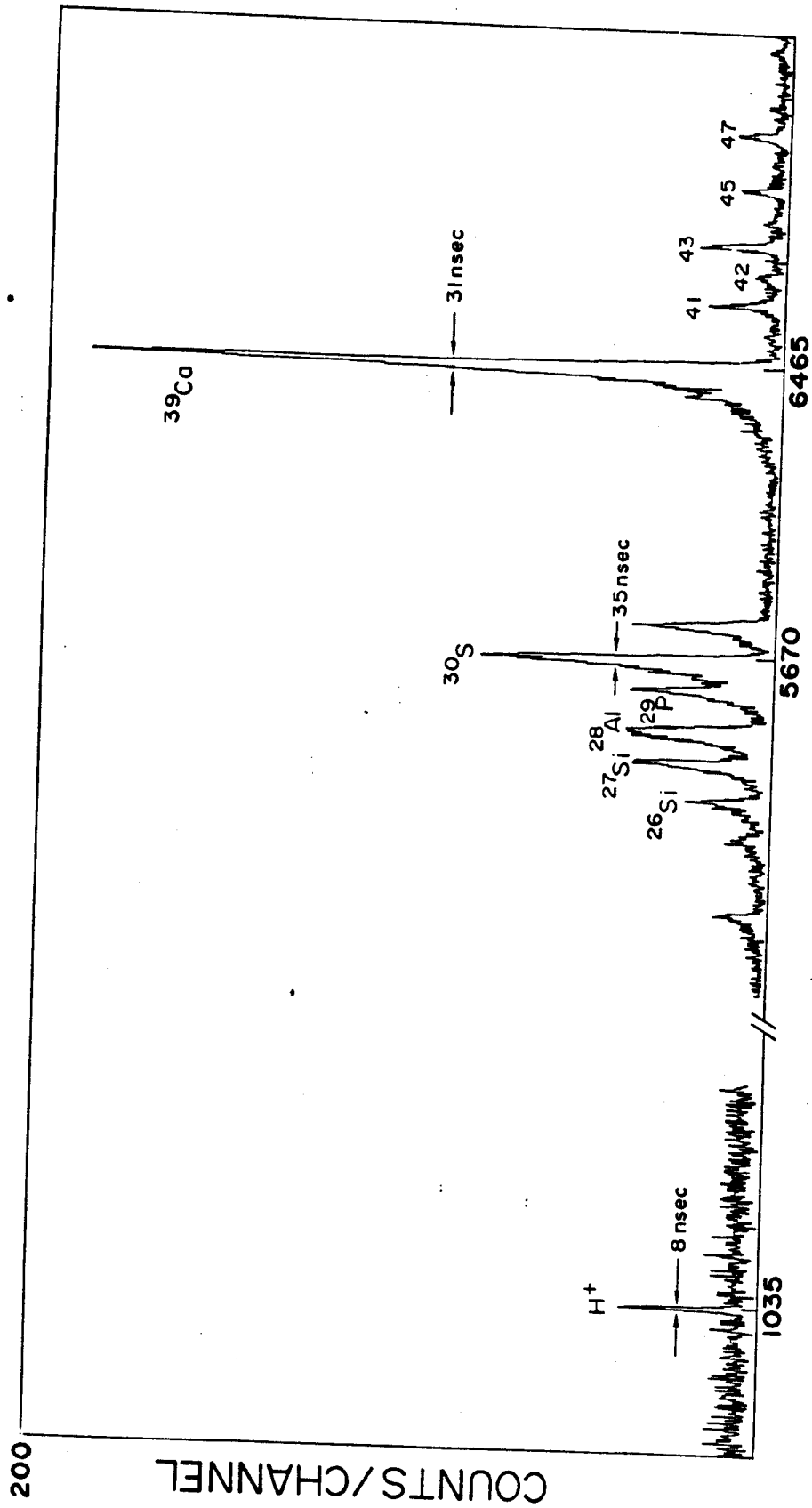

Figure 4-1. Comparison of peak width for KCl spectrum.

energy recoils should transform into shorter TOF events, and this is not what one observes in the accumulated TOF spectra; in fact, the converse seems to be true. That is, the low energy events seem to be the more probable events to be detected. The entire puzzle is especially intriguing, since in the early days of development of SIEGFRIED and its forerunners it was not known for sure whether recoils from β decays would be energetic enough to escape the surface on which they were deposited (Ed76), (Ma74). It appears, however, that not only are the recoils energetic enough to free themselves, but also the recoil energy is a significant contribution to the peak broadening.

Just how important are broadening effects such as electronic timing contributions in our measurements is a reasonable concern that we will deal with briefly here. A very rough argument for nanosecond range precision can be made by consideration of the performance specifications for the various NIM modules used for the TOF measurements. This is not quite so convincing as an internal measure or upper bound on intrinsic broadening. Happily, nature sees fit to provide us with just such a means to estimate an order of magnitude figure of merit. Referring to Figure 4-1, it is found that a narrow peak occurs at exactly the position predicted for an H^+ ion. Obviously, a proton is the result of a neutron undergoing a β decay and it seems a bit far-fetched to hypothesize neutrons being transported

and deposited on the collection plate; however, the cluster molecules are somehow formed from saturated hydrocarbons (e.g., C_6H_6), so there is certainly an abundant source of hydrogen atoms at the collection site. The exact mechanism for how the H^+ ions result from decay-related events is certainly not clear. However, the recoil energies involved in a "typical" β decay of medium-light nuclei are on the order of a few hundred electron volts. When one compares such recoil energies with typical carbon-hydrogen bond energies, which are roughtly 5 electron volts, the dissociation and ionization of a hydrogen atom from a recoil-bearing cluster is a plausible occurrence. Furthermore, in a number of spectra taken by a group at Orsay on a TOF system much like SIEGFRIED (Be78) a large, prominent spike is also assigned to the H^+ ion.

Accepting this assignment we can use the full width at half maximum (FWHM) to obtain an estimate of the intrinsic broadening effects due to the electronics. As shown, the H^+ ion has a FWHM of 8 nsec which represents a real limit on the peak broadening. In comparison, the mass groups at longer times of flight have FWHM's of about 4-5 times that of the H^+ peak. As we intend to show, the peak widths result from the spread in recoil energy that the daughter nucleus has after the β decay.

Another aspect of the TOF spectra that is especially intriguing is the overall shape of the peaks. This is

most easily seen in the large, isolated peaks corresponding to ^{39}Ca in Figure 4-1 and ^{23}Mg in Figure 3-1 and 3-5. All exhibit a long, exponential-type tailing on the short TOF side with a very sharp drop-off on the higher channel side. This distinctive feature seems to just elicit further investigation.

As a first step in the analysis, we decided to attempt to fit the TOF spectra with the program SAMPO, since it is a fairly flexible and easily run data analysis routine. SAMPO is a Fortran routine written and developed by J. T. Routti and S. G. Prussin (Ro69) to perform automatic data-analysis of γ-ray spectra. The routine is familiar to spectroscopists involved in Ge(Li) work but is probably rather foreign to mass spectroscopists in general. In order to elucidate our fitting results, a brief description of the analysis routine and the associated terminology will be given here.

In SAMPO the peak shape is approximated by a function that is basically a Gaussian with possible high- and/or low-channel tailing that "goes" as exponentials. The amount of tailing is determined by the distance in channel number from the centroid to the points at which the Gaussian is joined to the appropriate exponential. At these junctions the function and its first derivatives are continuous; as a result, the complete peak shape, aside from the normalization, is specified by three parameters:

(1) CW, the width of the Gaussian, (2) CL, the slope parameter of the low-channel exponential tail and (3) CH, the parameter of the high-channel tail. The significance of the magnitudes of these shape parameters is very straightforward: (1) a large CW means a wide Gaussign contribution, (2) a large CL yields a fast rise on the low-channel side, and (3) a large CH gives a rapid fall-off of the peak on the high-channel side.

Shown in Table IV-1 are the results of a SAMPO fit for the KCl spectrum of Figure 4-1. As indicated by the χ^2 for each, the fitting routine has proved to be well suited to deal with the rather asymmetric shapes. The CW's for all the identified species except the ^{28}Al case are very large. (CW as was discussed earlier, is the width parameter for the Gaussian contribution to the peak shape.) The magnitudes of the CW's shows a significant broadening effect in the TOF peaks. The low-channel tail parameter (CL) for the peaks are generally small and reflect a long, slow drop-off on the shorter TOF side. Especially striking is the size of CH for masses 26 through 39, excluding the ^{28}Al. All the CH's for this set are greater than 5; in fact, all except the ^{27}Si case are greater than 10! This indicates that the exponential fall-off on the high-channel side of the peak is very, very rapid. In fact, the large size of the CH's implies some type of cutoff -- a limit on the maximum time-of-flight allowed. If we

Table IV-1. Results of SAMPO Fitting of KCl Spectra.

A	Centroids	σ	CL	CH	CW	E_β (MeV)	R (eV)	% Fermi	CH/CL
^{26}Si	5515	1.08	1.81	15.9	6.16	3.81	380.8	1.00	8.8
^{27}Si	5619	1.05	1.04	6.37	4.74	3.79	362.1	.640	6.12
^{28}Al	5704	.99	.14	.45	2.92	2.86	213.4	0.0	3.2
^{29}P	5809	1.06	4.6	24.1	7.5	3.92	359.0	.815	5.24
^{30}S	5892	1.01	2.0	14.8	7.4	4.44	434.5	1.0	7.4
^{31}S	5983	.945	3.93	18.64	9.3	4.37	408.6	.815	4.74
^{29}Ca	6668	1.22	2.81	62.36	8.2	5.5	494.0	.648	22.2
41	6836	1.16	2.78	1.13	3.12	----	-----	-----	.41
43	6992	1.08	6.9	6.2	6.45	----	-----	-----	.90

FWHM = 2.355 x CW

equate the time of flight with the total energy of the recoil ion, as shown in Appendix I, the TOF is inversely proportional to the kinetic energy of the ion. In light of this, it is easily seen that the maximum TOF corresponds to a minimum allowed kinetic energy, that acquired by acceleration across the gap region.

To sum up the results of the fitting briefly, the peak shapes predicted by SAMPO will display a long tailing for the shorter TOF's, a wide Gaussian portion and a very fast fall-off on the high time side. A glance at the KCl spectrum readily exhibits this predicted behavior. Obviously there must be a reason for these asymmetric peak shapes, although the causes may not be immediately pinpointed. Nonetheless, the simplest hypothesis concerning the TOF peaks seems to be that the initial recoil energy of the daughter nucleus is somehow related to the observed spectral shapes. If this is so, then we can develop a quantitative relationship between the observed peak shape parameters and the recoil energy of the daughter nuclei.

Obviously, the broadening of the mass peaks is not an electronic effect. Is it reasonable to attribute the effect to the initial recoil energy of the daughter nuclei? As is shown in Appendix I, using a gross model of the SIEGFRIED system, we can estimate the time-of-flight of a singly charged ion of mass number A and initial recoil energy R by the expression:

$$TOF = m^{1/2} \left\{ \frac{\ell - d}{[2(E+R)]^{1/2}} + \frac{1.41d}{E} \left[\sqrt{R+E} - R^{1/2} \right] \right\} \quad (4\text{-}1)$$

Rigorously $R = 1/2MV_z^2$ where V_z is the initial velocity in the z direction, that is, in the direction of the flight tube axis. In Table IV-2 are the results of times of flight calculated for the mass set observed in the KCl spectrum. R is the maximum initial recoil energy, T(R) the corresponding TOF, T(O) the TOF for zero initial recoil, and ΔT the difference between T(O) and T(R). The TOF differences are all in the neighborhood of a few hundred nanoseconds. Considering our timing resolution to be of the order of nanoseconds, it is imminently plausible that the recoil energy effect is a significant contribution to the broadening.

We have argued that the peak shape, especially the broadening is because of the initial recoil energy of the measured mass species; if that is so, then it seems reasonable to attempt to develop a quantitative relationship between some measured peak shape parameters and the recoil energy of the ion. First, we need to have some rough form of the parameterization. If we consider the ions drifting along the flight tube, with negligible time of acceleration (correct to ≈3%, see Appendix I) then we can write:

Table IV-2. Calculated TOF's for KCl Spectrum (in nsec).

A	R	TOF(R)	TOF(O)	ΔT	$\Delta T/T_{mean}$
26	381	5055	5244	189	.036
27	362	5160	5344	184	.034
28	213	5323	5442	119	.022
29	359	5349	5539	190	.034
30	434	5406	5633	227	.040
31	409	5507	5726	219	.038
39	494	6134	6423	289	.045

$$E = 1/2mv^2 = 1/2m \frac{\ell^2}{t^2} \qquad (4\text{-}2)$$

E is the ion kinetic energy, v its velocity, m the mass, ℓ, the flight length and t the time of flight.

Now suppose an ion starts with zero recoil energy, then $E = qV \equiv E_o = 1/2mv_o^2$, where V is the electrostatic potential on the collection plate and q is the charge on the recoil ion. If the ion starts out with the maximum recoil energy, with zero transverse momentum ($p_z^2/2m = R$, R the maximum recoil energy), then $E = E_o + R = 1/2mv^2 \approx 1/2m\ell^2/t_1^2$.

So we have

$$E_o = 1/2m\ell^2/t_o^2 \qquad (4\text{-}3)$$

$$E_1 = 1/2m\ell^2/t_1^2 \qquad (4\text{-}4)$$

$$E_1 - E_o = R = 1/2m\ell^2\left(\frac{1}{t_1^2} - \frac{1}{t_o^2}\right) \qquad (4\text{-}5)$$

If we make the assumption that the measured TOF is linear in channel number and the spread is proportional to the FWHM (or equivalently to CW from SAMPO fitting), we can write:

$$t_o = K(CP + CW) \tag{4-6}$$

$$t_1 = K(CP - CW) \tag{4-7}$$

$$t_o^2 = K^2(CP^2 + 2CP\ CW + CW^2) \tag{4-8}$$

$$= K^2CP^2(1 + 2CW/CP + CW^2/CP^2) \tag{4-9}$$

Similarly,

$$t_1^2 = K^2CP^2(1 - 2CW/CP + CW^2/CP^2) \tag{4-10}$$

Since typical values of CW/CP are on the order of 10^{-3}, we can drop the $(CW/CP)^2$ terms.

Using the binomial theorem and retaining terms to first order, we have

$$\frac{1}{t_1^2} \approx \frac{1}{K^2CP^2}(1 + 2CW/CP) \tag{4-11}$$

$$\frac{1}{t_o^2} \approx \frac{1}{K^2CP^2}(1 - 2CW/CP) \tag{4-12}$$

$$R = \frac{m^2}{2}\left[\frac{1}{t_1^2} - \frac{1}{t_o^2}\right] = \frac{m\ell^2}{2}\frac{1}{K^2CP^2}\left(\frac{4CW}{CP}\right) \tag{4-13}$$

$$R = \alpha A \frac{CW}{CP^3} \tag{4-14}$$

This last expression is the form that will be used to relate the recoil energy to the TOF peaks parameters CW and CP.

We now have a parametric form to test. Next we need some experimental cases to apply it to. Since we are really working in a new area, it is obvious that there are certain criteria for the spectra we will attempt to fit. We require fairly high statistics in each peak and that the decays be fairly simple; also we prefer as high a multiplicity of peaks in the spectrum as is obtainable. The reasons for these conditions are fairly obvious; we are in the position of hypothesizing a relationship that we believe can be expressed by a simple functional relationship. Now, in order to prove or, at least further, this view, we must start with the most reasonable set of tests available. The KCl and Al spectra come closest to fulfilling our rather loose conditions. The Al target has been the standard for our runs and is well understood, while the KCl spectrum has a fair multiplicity of single species, peaks, good statistics and the "characteristic" shapes of TOF peaks occurring in a number of instances.

The actual form of the equation used for the fitting was

$$y_i = ax_i + b \qquad (4\text{-}15)$$

$$x_i = CW/(CP)^3 \cdot A \quad \text{(CP in kilochannels)} \qquad (4\text{-}16)$$

y_i = Recoil energy of species i

A linear least squares fit was performed on three known cases, and the resulting parameters were used to predict the recoil energy of the members of the set not included in the least squares fitting. The predicted values were then compared with the known values.

The maximum recoil energy of a daughter nucleus with mass number A was calculated using the following equation:

$$R = \frac{537}{A} (E_o + 1.022)) \qquad (4\text{-}17)$$

where

E_o is the maximum kinetic energy of the β particle in MeV

A is the mass of the recoil in amu

R is the maximum energy of the recoil in eV

(For the derivation see Appendix II.)

The first example of the fitting is for the KCl spectrum Our procedure was to choose two sets of three peaks as the "known" energies and predict energies for the remaining peaks in the spectra. The first set chosen for the

calibration corresponds to ^{26}Si, ^{27}Si and ^{30}S. In Table IV-3 are the results of a linear least squares fit to the recoil and decay energies for this set. The predicted decay energies are calculated from the fitted recoil energies according to the formula

$$E_o = \sqrt{0.261 + \frac{A \cdot R}{537}} - 0.511 \qquad (4\text{-}18)$$

(with R in eV and E_o in MeV)

The fit for this set is fairly good, χ^2 for the standards is 1.1, and the largest deviation is 4%. The results of applying the equation $R_i = ax_i + b$ to the remaining peaks in the spectrum are given in Table IV-3: the errors in the recoil energy are all in the neighborhood of 15%, the fit to the decay energies closer to 10%. The worst fit is for the ^{29}P case, which is not well separated from the tail of the ^{30}S.

The mass-28 peak actually gives a somewhat better fit than was expected, considering the decay scheme of ^{28}Al, shown in Figure 4-2. The β decay of ^{28}Al is to the 2^+ excited state of ^{28}Si which decays via a γ ray to the 0^+ state. Also the decay of the ^{28}Al is by negatron (β-) decay whereas the rest of the decays we observe are by positron decays. Since the collector plate is 10-mil

Table IV-3. Fit to KCl Spectra Recoil Energies (no F-GT Correction).

Calibrated

A	R (eV)	y^{fit} (eV)	% Error	E_o (MeV)	E^{fit} (MeV)	% Error
26	380.	497.	4.5	3.81	3.90	2.4
27	362.	355.	1.8	3.79	3.74	1.3
30	434.	424.	2.4	4.44	4.38	1.3

$X^2 = 1.1$

Predicted

A	R (eV)	y^{fit} (eV)	% Error	E_o (MeV)	E^{fit} (MeV)	% Error
28	273.	302.	11.	2.86	3.08	7.7
29	359.	428.	19.	3.92	4.32	10.
31	410.	473.	15.	4.37	4.74	8.5
39	494.	423.	14.	5.5	5.05	8.2

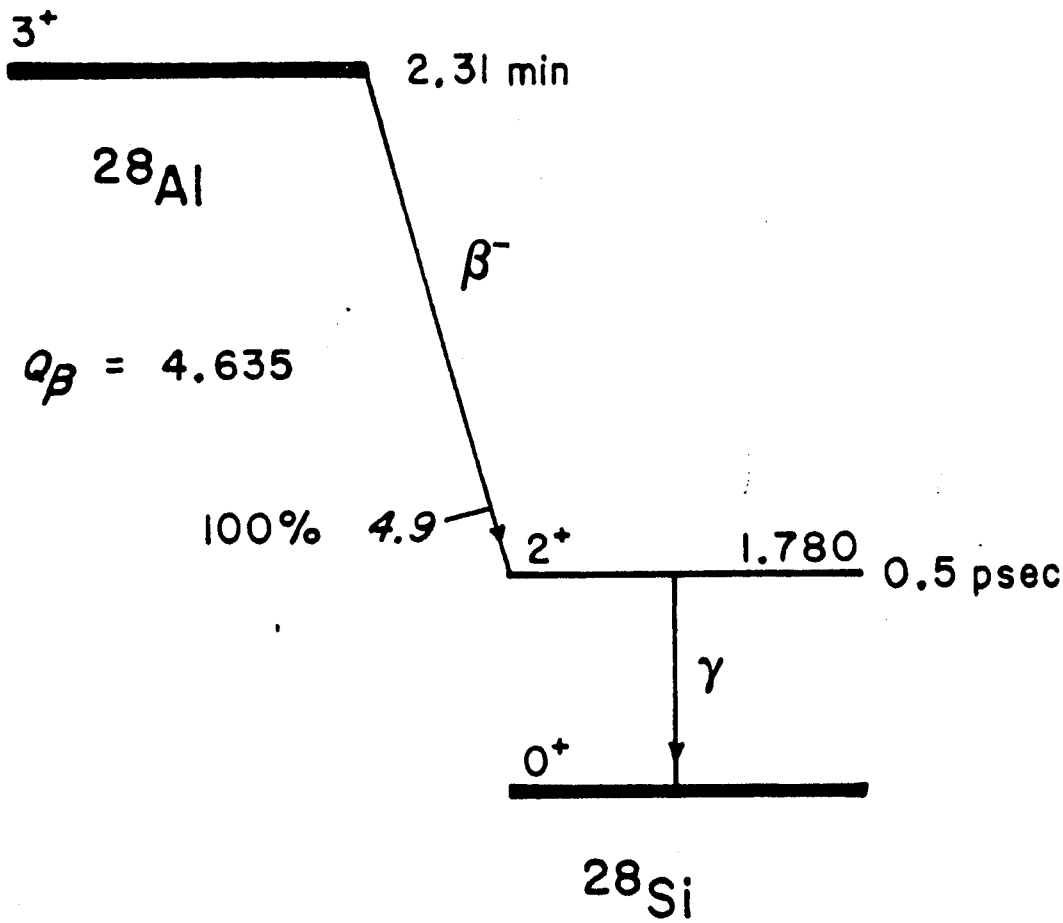

Figure 4-2. Decay of ^{28}Al.

stainless steel, it will stop β's of an energy of less than about 1 MeV, which means that the lower energy events are discriminated against; however, the plastic (NE-102) has roughly a 30% efficiency for detection of γ rays of energy 1.8 MeV, so that if the γ ray is emitted in the "right" direction, it has some probability for serving as a valid start signal and can result in a detectable TOF event. The estimation of the γ detection efficiency was accomplished by using a nomogram developed by Roulstan and Naqui (Ro57). In the case of the positron-emitters, even if the low-energy β's are stopped by the collector plate, the accompanying annihilation radiation is suitable for serving as a start event. Using the same procedure mentioned earlier, the gamma efficiency for 511-keV annihilation radiation is about 50%.

The second case we attempted to fit with our recoil energy parameterization was the TOF spectrum resulting from 70-MeV ^{3}He on a pure aluminum target. Unfortunately there are only four peaks with reasonable statistics and shape. The ^{28}Al peak is very broad and shaped distinctly differently from the common TOF peaks, and the ^{29}P peak has very poor statistics. The peaks chosen for the "known" energies are the three corresponding to masses 23, 25, and 27, respectively; the results of these fits are given in Table IV-4. The χ^2 for this fit was 7.4, and, as shown, the fit errors are in the neighborhood of a few percent.

Table IV-4. Fit for Al Spectrum -- No F-GT Correction.

A	R (eV)	y^{fit} (eV)	% Error	E_o (MeV)	E^{fit} (MeV)	% Error
23	287.	286.	0.3	3.0	3.03	1.0
25	299.	331.	11.0	3.26	3.45	6.0
27	362.	325.	10.0	3.79	3.56	6.0

Fermi and Gamow-Teller Distributions

One assumption that is implicit in the parametric treatment of the recoil energy is that all allowable energies are equally probable and all the various decays have the same initial energy distributions. This is not actually true, for, as is known from β-decay theory, the distribution function for the recoil energy is dependent upon the "type" of decay the parent nucleus undergoes. I will not endeavor to present a full treatment of β-decay theory here, there being a large number of well-known and more appropriate texts for such a task. However, I will give a somewhat pedestrian and brief discussion of general results and terminology from what is called allowed β-decay theory.

In the β-decay of a nucleus, an electron and an antineutrino are emitted, and each of these particles has a spin 1/2. If the total spin of the decaying nucleus is unchanged, then, in order to conserve total angular momentum the electron and antineutrino must have antiparallel spins. This type of decay is often called a "Fermi" decay. If the total spin of the parent changes by 1 (in units of $\hbar$), then the electron and antineutrino must carry off one unit of angular momentum, i.e., they have parallel spins. This type of decay is known as "Gamow-Teller" decay. Common terminology in β-decay theory attributes Fermi decay solely

to a "vector" interaction and Gamow Teller to an "axial-vector interaction." Because these two interactions are "effectively" different, the probability that a recoiling nucleus has a given energy is dependent upon the type of interaction that gives rise to the decay.

In Figure 4-3 are shown the distribution functions for the recoil energies corresponding to the two types of decay considered here. The distribution functions for both cases are skewed towards higher energies, but the one corresponding to the so-called Fermi decay is obviously more sharply peaked, favoring higher-energy recoils. When one takes into consideration these two distributions, it becomes reasonable to ask whether the effects of the initial energy distribution are in some way contained in the observed peak shapes. If that is the case, then, even if there is only a gross relationship, it is very useful and highly intriguing. Assuming the initial energy distribution effects are somehow preserved, we need to quantify the influence of the distribution upon the TOF peak shapes. The majority of decays observed are actually mixed, that is, they result from a combination of the Fermi and Gamow-Teller decay modes. In an attempt to take this account, we have included as a multiplicative fixed parameter the quantity, $D \equiv (f_F + \alpha f_{GT})$ where f_F and f_{GT} are the fractions of transition probability due to the Fermi and Gamow-Teller modes, respectively. The factor α is a strength parameter that

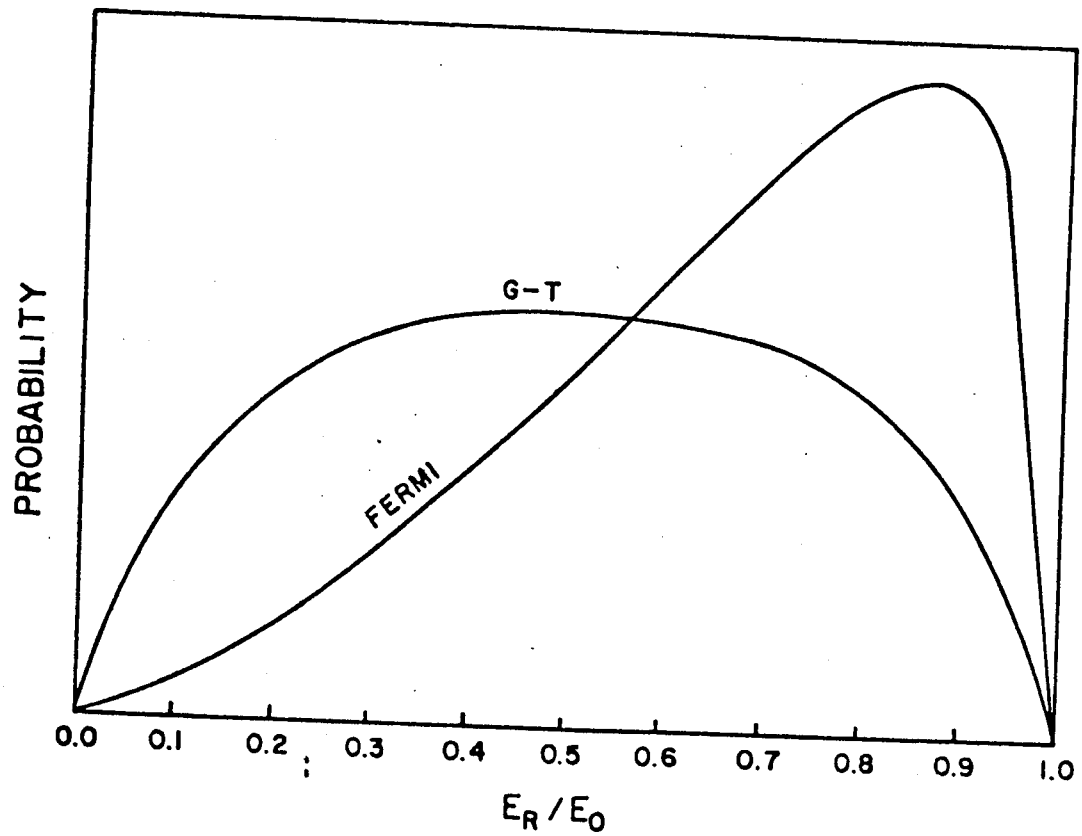

Figure 4-3. Fermi-Gamow-Teller recoil energy distributions.

is a measure of the relative contribution of the Gamow-Teller mode to the FWHM of a composite energy distribution. (It is estimated by taking the ratio of FWHM's for the two distributions shown in Figure 4-3. A rough estimate in most cases gives $\alpha \approx 0.5$.) The quantities f_F and f_{GT} can be found if the ft value of the decay is known.

If we define $|M_F|$ and $|M_{GT}|$ as the matrix elements for the vector and axial vector interaction, and C_V and C_A as dimensionless coupling constants for the vector and axial vector interactions, then

$$ft = \frac{6143}{|M_F|^2 + \left(\frac{C_V}{C_A}\right)^2 |M_{GT}|^2} \qquad (4\text{-}19)$$

(with $C_A\, C_V \approx 1.25$)

Now, f_F and f_{GT} are defined as

$$f_F = \frac{M_F^{\,2}}{|M_F|^2 + \left(\frac{C_V}{C_A}\right)^2 |M_{GT}|^2} \qquad (4\text{-}20)$$

(with $f_{GT} = 1 - f_F$)

So in order to obtain f_F and f_{GT}, we need the ft value for the decay and a value for either $|M_F|^2$ or $|M_{GT}|^2$. In

most cases of interest to us, the decays will be simple mirror transitions or at most decays that are classified as allowed, in which instances there are simple rules to calculate $|M_F|$. The ft values can be calculated, (see (Wu66)) or obtained from the literature. The combination ft and $|M_F|$ allow one to calculate f_F and f_{GT}, which represent the fraction of decay strength due to the Fermi and Gamow-Teller decay modes, respectively.

In Table IV-5 are given the ft values and calculated values of $|M_F|$, f_F, f_{GT}, and D for all the known decays observed as described earlier in this chapter is followed, except now the independent variable is $D_A \cdot A \cdot \frac{CW}{CP^3}$, where D_A is totally determined by the particular decay. The results of this new parameterization applied to the KCl spectrum are given in Table IV-6. χ^2 for the linear least squares fit to the "known" cases was 1.8, not significantly different from the simpler initial parameterization, perhaps a little worse. The same seems to hold true for the fit to the "unknowns." However, referring to Table IV-7 where the results of the new parametric fit for the Al spectrum are given, a very obvious improvement in the fit to the "known" peaks is evidenced. In fact, χ^2 for this fit is 0.04, a very large and significant reduction from the χ^2 of 7.4 for the simpler parametric form. But the fit to the ^{27}Si "unknown" is very poor in this instance.

Table IV-5. Fermi-Gamow-Teller Parameters for Peaks in KCl Spectrum.

A	ft	$\|M_F\|^2$	f_F	f_{GT}	D	x'
26	3162	2	1.0	0.0	1.0	0.97
27	3981	1	0.65	0.35	0.85	0.61
28	7943	0	0.0	1.0	0.58	0.26
29	5012	1	0.82	0.18	0.92	1.05
30	3162	2	1.0	0.0	1.0	1.12
31	5012	1	0.82	0.18	0.92	1.28
39	3981	1	0.65	0.35	0.85	0.94

Table IV-6. Recoil Fit for KCl Spectrum (With F-GT Correction).

A	R (eV)	R^{fit} (eV)	% Error)	E_o (MeV)	E^{fit} (MeV)	% Error
Calibrated						
26	381.	401.	5.	3.81	3.92	3.0
27	362.	356.	1.6	3.79	3.75	1.0
30	434.	420.	3.4	4.44	4.36	1.8
Predicted						
28	273.	308.	13.	2.87	3.53	23.
29	360.	411.	14.0	3.92	4.23	8.0
31	409.	440.	8.0	4.37	4.55	4.0
39	494.	397.	20.0	5.5	4.88	11.0

Table IV-7. Fit to Al Spectrum Recoil Energies (With F-GT Correction).

A	R (eV)	R^{fit} (eV)	% Error	E_o (MeV)	E^{fit} (MeV)	% Error
23	287.	284.	.7	3.0	3.01	.48
25	299.	297.	.8	3.26	3.24	.61
27	362.	362.	.1	3.79	3.788	.05

CHAPTER V

MODELING THE TOF SYSTEM

I. Introduction

The results of the empirical fitting to the observed recoil energies in the previous section were encouraging enough to elicit further investigation. As a means of theoretically justifying our assumption about the recoil energy contribution to the peak broadening, we decided to mathematically model our TOF system and the resulting particle trajectories.

The first step in modeling our TOF system was to obtain a reasonable set of electric fields. The system is made up of elements of finite lengths and edges whose effects should not be totally ignored. As with most practical problems, analytic solutions exist only for idealized cases. For real geometries we often have to settle for approximate solutions. To this end numerical methods are especially well-suited. To obtain the electrostatic potentials for our system we have to solve Laplace's equation subject to the appropriate boundary conditions. The iterative technique of relaxation is a standard method

for obtaining approximate solutions to Laplace's equation. Once we have a reasonable set of fields, we can calculate particle trajectories. This means that we have to integrate equations of motion for charged particles. To accomplish this we used a combination of Runge-Kutta and Predictor-Corrector algorithms. Since these numerical methods are an integral part of our modeling study, we will present a discussion of them in some depth. This is especially true for the relaxation methods we employed because of what we feel is their growing importance in this age of digital computers.

II. Relaxation Techniques

A. Preliminary

The solution of Laplace's equation for a system of conductors is one of the most common problems in electrostatics. Students are often taught the usual analytic methods of solution: images, Green's functions, and expansions in orthogonal functions. The powerful yet inelegant numerical techniques are rarely presented as alternate approaches. For the more complicated numerical techniques, this exclusion is understandable. However, the relaxation technique, which we shall discuss here, is so simple and well-suited to boundary-value problems, that once learned, it provides a valuable tool for constructing

solutions for many common and specific problems. When used in conjunction with digital computers available today, relaxation techniques are able to handle problems that are beyond the scope of practical analytic solution.

In this section we present a straightforward discussion and derivation of relaxation and the related over-relaxation techniques. We then apply these techniques, both to simple problems such as would arise in a classroom and also to slightly more complicated problems such as have arisen from our own experimental work.

Occasionally, in discussions of Laplace's equation, students are told that it implies that the potential at a given point is the average of the potential on a surface enclosing the point. Then, to demonstrate this, the potential at the center of a charged, hollow, spherical conductor is shown to be the same as the average on the surface. Such an example serves the purpose well enough for the specific case of spherical symmetry, but the implications of Laplace's equation need not be so restricted. We feel that it is reasonable to demonstrate to students that the general equation

$$\nabla^2 \Phi = 0, \qquad (5\text{-}1)$$

can be interpreted as a differential statement of the fact that the solution at a specific point is just the <u>average</u>

of the solutions over a surface of any shape surrounding the point of interest. If such a demonstration can be easily given, it will greatly enhance and supplement specific examples. (As will be shown, application of relaxation techniques to boundary-value problems in electrostatics is intimately and obviously dependent upon the differential validity of the averaged nature of solutions to Laplace's equation.)

The presentation of relaxation methods in electricity and magnetism texts is nearly nonexistent. A notable exception is the introductory text, Volume II of the Berkeley Physics Course. Yet even here the student must delve into the recesses of an appendix on advanced problems. There a recipe, applicable only to a two dimensional Cartesian problem, is given. The basis for the prescription and its extension to other orthogonal systems is not discussed. With a few elementary preliminaries we will attempt to correct such exclusions and present relaxation techniques in a manner that students of electrostatics can appreciate and employ, having access to only modest sized computer.

B. Mathematical Preliminaries

To those of us who worked our way through differential calculus with mild chagrin, the definition of a derivative is perhaps familiar yet seldom used. However, for numerical solutions the finite divided-differences that define a

derivative as a limit are essential to replacing a differential equation by an analog algebraic expression.

Recalling the definition of the derivative at a point x_o, we have

$$\left.\frac{df(x)}{dx}\right|_{x=x_o} = \lim_{\Delta x \to o} \frac{f(x_o+\Delta x) - f(x_o)}{\Delta x} \qquad (5\text{-}2)$$

This expression gives an approximation to the derivative when Δx is small; that is,

$$\left.\frac{df(x)}{dx}\right|_{x=x_o} = \frac{f(x_o+\Delta x) - f(x_o)}{\Delta x} . \qquad (5\text{-}3)$$

Of course, this is an approximation and the associated error is on the order of Δx. As shown in the Appendix IV, a better approximation is given by

$$\left.\frac{df(x)}{dx}\right|_{x=x_o} = \frac{f(x_o+\Delta x) - f(x_o-\Delta x)}{2\Delta x}; \qquad (5\text{-}4)$$

and for the second derivative,

$$\left.\frac{d^2f(x)}{dx^2}\right|_{x=x_o} = \frac{f(x_o+\Delta x) - 2f(x_o) + f(x_o-\Delta x)}{(\Delta x)^2} \qquad (5\text{-}5)$$

These last two expressions have associated errors on the order of $(\Delta x)^2$, which shows the advantages of choosing Δx small. The extension of these expressions to partial derivatives is straightforward and given in Appendix IV.

Now let us consider Laplace's equation for a two-dimensional Cartesian system, at the point (x_o,y_o):

$$\left.\frac{\partial^2\Phi(x,y)}{\partial x^2}\right|_{\substack{x=x_o\\y=y_o}} + \left.\frac{\partial^2\Phi(x,y)}{\partial y^2}\right|_{\substack{x=x_o\\y=y_o}} = 0. \qquad (5\text{-}6)$$

The analogous expression in terms of finite differences is

$$\frac{\Phi(x_o+\Delta x,y_o) - 2\Phi(x_o,y_o) + \Phi(x_o-\Delta x_o,y_o)}{(\Delta y)^2} +$$

$$\frac{\Phi(x_o,y_o+\Delta y) - 2\Phi(x_o;y_o) + \Phi(x_o,y_o-\Delta y)}{(\Delta x)^2} = 0. \qquad (5\text{-}7)$$

Rearranging this last expression, we have

$$\Phi(x_o,y_o) = \frac{1}{2(1+(\frac{\Delta x}{\Delta y})^2)} \{\Phi(x_o+\Delta x,y_o) + \Phi(x_o-\Delta x,y_o)$$

$$+ (\frac{\Delta x}{\Delta y})^2 \ (\Phi(x_o,y_o+\Delta y) + \Phi(x_o,y_o-\Delta y))\}. \qquad (5\text{-}8)$$

If we choose $\Delta x = \Delta y \equiv h$ we obtain the simple expression,

$$\Phi(x_o,y_o) = \frac{1}{4} \{\Phi(x_o+h,y_o)+\Phi(x_o-h,y_o)+\Phi(x_o,y_o+h)+\Phi(x_o,y_o-h)\} . \qquad (5\text{-}9)$$

this makes it clear that the potential at $x_o,y_o)$ is equal to the average of the potentials at points around (x_o,y_o).

Furthermore, it is simple to obtain equivalent expressions when we need to deal with different coordinate systems. Consider the Laplace equation for an axisymmetric system in cylindrical coordinates, $\Phi = \Phi(\rho,z)$:

$$\nabla^2\Phi = \frac{\partial^2}{\partial\rho^2} \ \Phi(\rho,z) + \frac{1}{\rho}\frac{\partial\Phi}{\partial\rho}(\rho,z) + \frac{\partial^2\Phi}{\partial z^2}(\rho,z) = 0. \qquad (5\text{-}10)$$

At the point (ρ_o,z_o) the equivalent finite-difference expression is

$$\frac{\Phi(\rho_o+\Delta\rho,z_o)+\Phi(\rho_o-\Delta\rho,z_o)-2\Phi(\rho_o,z_o)}{(\Delta\rho)^2}+\frac{1}{\rho_o}\,\frac{\Phi(\rho_o+\Delta\rho,z_o)=\Phi(\rho_o=\Delta\rho,z_o)}{2\Delta\rho}$$

$$+\frac{\Phi(\rho_o,z_o+\Delta z)+\Phi(\rho_o,z_o-\Delta z)-2\Phi(\rho_o,z_o)}{(\Delta z)^2}=0\,. \qquad (5\text{-}11)$$

Rearrangement yields

$$\Phi(\rho_o,z_o)=\frac{1}{2(1+(\frac{\Delta\rho}{\Delta z})^2)}\{\Phi(\rho_o+\Delta\rho,z_o)(1+\Delta\rho/2\rho_o)+\Phi(\rho_o-\Delta\rho,z_o)(1-\Delta\rho/2\rho_o)$$

$$+(\frac{\Delta\rho}{\Delta z})^2\,(\Phi(\rho_o,z_o+\Delta z)+\Phi(\rho_o,z_o-\Delta z))\}\,. \qquad (5\text{-}12)$$

In this last equation it appears that we have a singularity for $\rho_o = 0$, but for axial symmetry,

$$\left.\frac{\partial\Phi}{\partial\rho}\right|_{\rho=0}=0\,. \qquad (5\text{-}13)$$

Therefore, by L'Hôpital's rule,

$$\lim_{\rho_o \to 0} \frac{1}{\rho_o} \frac{\partial \Phi}{\partial \rho}\bigg|_{\rho_o} = \frac{\partial^2 \Phi}{\partial \rho^2}\bigg|_{\rho_o} \quad . \tag{5-14}$$

At $\rho = 0$, LaPlace's equation is

$$2 \frac{\partial^2 \Phi}{\partial \rho^2} + \frac{\partial^2 \Phi}{\partial z^2} = 0 \quad , \tag{5 15}$$

and since (from Equation 5-4),

$$\frac{\partial \Phi}{\partial \rho}\bigg|_{\rho=0} = 0 \quad , \tag{5-16}$$

$$\Phi(0+\Delta\rho, z_o) = \Phi(0-\Delta\rho, z_o) \quad . \tag{5-17}$$

Rearrangement of the finite-difference equation equivalent to Equation 5-15 gives, for $\rho_o = 0$.

$$\Phi(0,z_o) = \frac{1}{2(2+(\frac{\Delta\rho}{\Delta z})^2)} \{4\Phi(\Delta\rho, z_o)+(\frac{\Delta\rho}{\Delta z})^2(\Phi(0,z_o+\Delta z)$$

$$+ \Phi(0,z_o-\Delta z))\} \quad , \tag{5-18}$$

which yields the starting point for applying relaxation techniques.

C. Techniques for Calculation

If one employs the appropriate expressions for the potential given in the preceding section, boundary-value problems become very amenable to iterative techniques of solution such as relaxation and its extension, overrelaxation. To employ either of these, our first step is to replace the continuous region of interest with a grid network as shown in Figure 5-1. For convenience we set up the grid so that conductor and boundary surfaces lie along grid lines. Next we make guesses for the value of the potential at every point that is not fixed by the problem. Such points will be called "free" points. A convenient initial guess for the free points would be all zeroes; although this will work, it is very inefficient. Intuitively, it seems that an initialization of the free points based on the analytic solution to a similar but less difficult problem is a reasonable first guess.

Relaxation consists of replacing the value of the potential at a particular free point by the average of its neighboring points according to Equation 5-8, or 5-12 and 5-18, whichever is appropriate to the coordinate-system. This procedure is applied to each free point in the network,

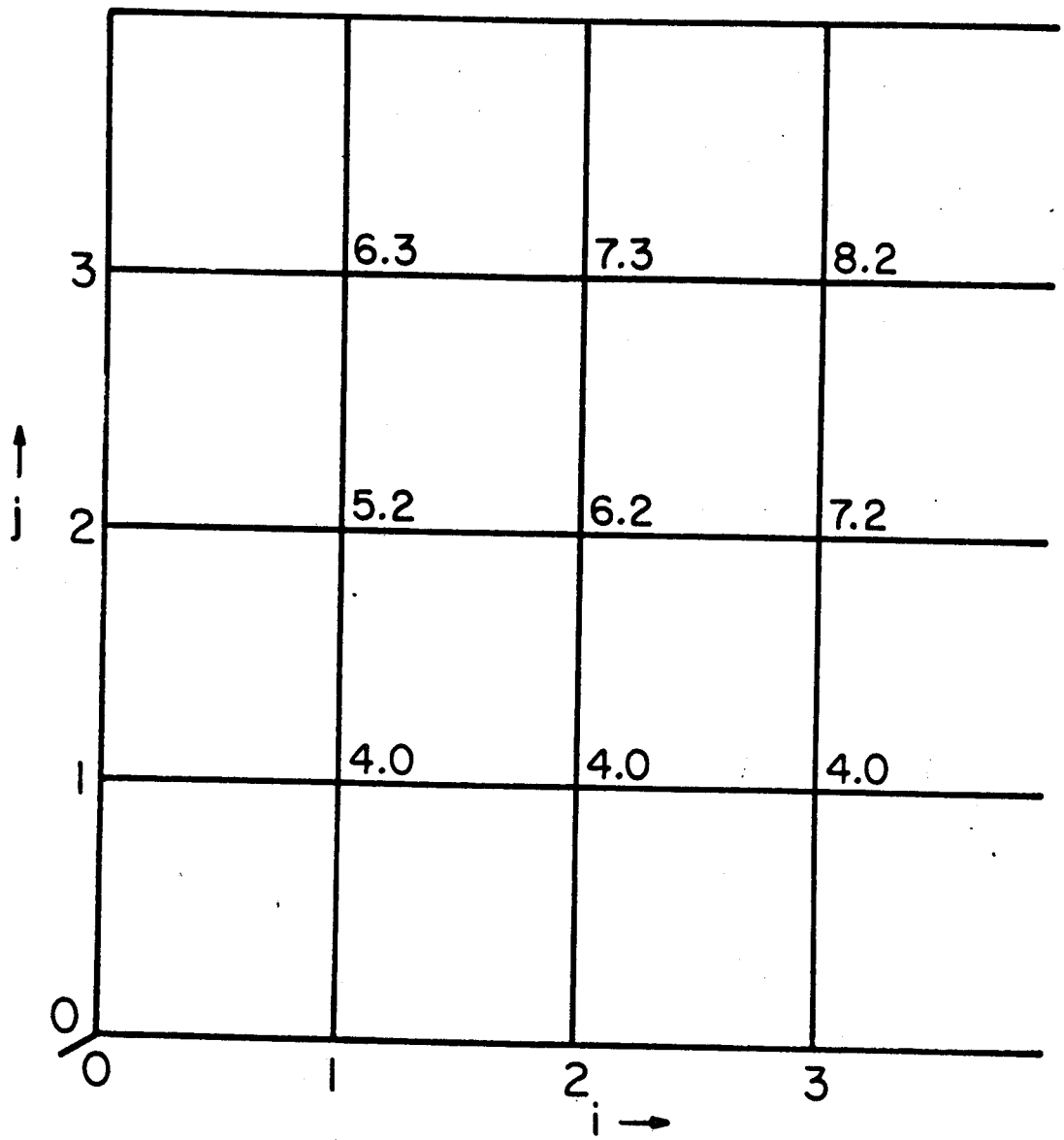

Figure 5-1. Two-dimensional x-y grid with $\Phi_{i,j}$'s at free points after one iterations. The grid spacing is the same in the x and y directions. $x = i\Delta$, $y = j\Delta$, where i, j are integers.

constituting one iteration. Iterations are continued until a reasonable convergence criterion is met. We have monitored the maximum percent change effected through one iteration.

For the Laplace problem it has been found that a modification of relaxation, called successive over-relaxation (SOR), may significantly accelerate convergence (Am69), (Fo60). Here the change in the distribution of values obtained from each iteration of relaxation is similar to a diffusion process; i.e., SOR acts to enhance the diffusing corrections by "amplifying" the averaging process.

To utilize SOR one must choose a relaxation factor, $1 < \omega < 2$. For the case of equal ρ and z mesh steps, an estimate of the optimum ω can be obtained from the expression

$$\omega_{opt} \approx \frac{2}{1+|\sin\Delta|} , \qquad (5\text{-}19)$$

where Δ is the mesh step size.

Denoting Φ_{ij}^{ℓ} as the value at (i,j) obtained from the ℓth iteration of ordinary relaxation, we get an "over-relaxed" value of Φ_{ij}^{SOR} by applying

$$\Phi_{ij}^{SOR} = (1-\omega)\Phi_{ij}^{\ell-1} + \omega\Phi_{ij}^{\ell} . \qquad (5\text{-}20)$$

Then we replace Φ_{ij} by Φ_{ij}^{SOR}. Choosing $\omega = 1$, reduces over-relaxation to relaxation.

Perhaps an example will more fully demonstrate. Refererring to Figure 5-1, suppose the values shown at each point were obtained after five iterations. Consider the point, (i = 2, j = 2); $\Phi_{22}^{5} = 6.2$, and using Equation 5-8, we obtain

Relaxation Step:

$$\Phi_{22}^{6} = 1/4(4.07+7.3+5.2+7.2) = 5.925 \ . \qquad (5\text{-}21)$$

If we are using only relaxation, we would move to the next point and compute the average of its neighbors. However, if we are using SOR with $\omega = 1.5$, our next step is

Over-Relaxation Step:

$$\Phi_{22}^{SOR} = (1-1.5)\Phi_{22}^{5} + 1.5\ \Phi_{22}^{6}$$

$$= -.5 \cdot 6.2 + 1.5 \cdot 5.925$$

$$= 5.7875 \qquad (5\text{-}22)$$

Next we take Φ_{22}^{6} to be 5.7875 and move on to the next point to repeat the procedure.

D. Applying Relaxation and Successive Over-Relaxation

A typical problem in electrostatics that is easily solved analytically is the case of two coaxial infinitely long cylinders held at different potentials. Referring to Figure 5-2, the closed form of the solution is found to be

$$\Phi(\rho) = (\Delta V/\ell n(a/b))\cdot \ell n(\rho/b) \ . \qquad (5\text{-}23)$$

This case provides an instructive application of the techniques and a simple means of comparing the convergence rates of relaxation and SOR.

We mock-up the infinite length by fixing the potential, at both ends of a finite coaxial length, to be the analytic solution. An equal ρ and z mesh size of 0.25 was employed. One hundred iterations were performed with a Xerox Σ-7 computer, first using ordinary relaxation and then SOR with $\omega = 1.75$. In both cases an initialization of $\Phi(\rho) = 50/(1+\rho)$ was used. The results for each, with their respective errors, at representative ρ points are given in Table V-1, after 10, 50, and 100 iterations. In the right-hand column the exact values from an analytic solution are given for comparison. Inspection of the table makes it apparent that the SOR method converges much more rapidly than the relaxation technique ($\omega = 1.0$). The time saved in computing can be significant.

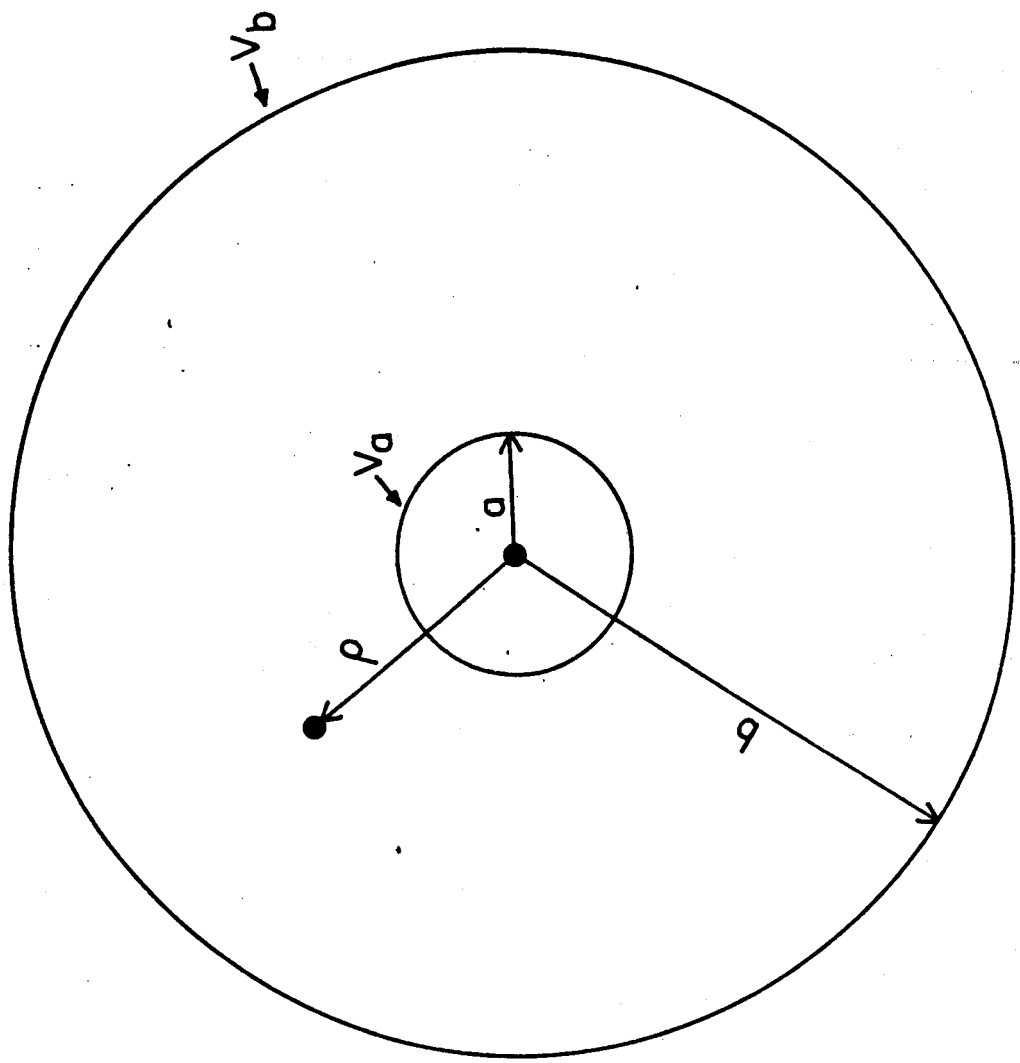

Figure 5-2. Cross section of infinitely long coaxial cylindrical conductors. The inner conductor has radius a = 1.0 and is held at Φ_a = 100; the outer conductor has radius b = 10.0 and is held at Φ_b = 0.0. The analytic solution is given in the text. $\Delta\Phi = \Phi_a - \Phi_b$.

Table V-1. Comparison of Relaxation and SOR Results for Infinite Coaxial Conductors.

	Numerical Value	% Error	Numerical Value	% Error	Exact Solution
	$\omega = 1.0$		$\omega = 1.75$		
	After 10 Iterations				
1.5	53.67	34.9	72.92	11.5	82.334
5.5	7.74	70.2	13.30	48.8	25.964
9.5	2.36	6.1	1.40	36.9	2.228
	After 50 Iterations				
1.5	69.90	15.1	81.31	1.3	82.334
5.5	8.92	65.6	23.92	7.9	25.964
9.5	1.2	46.2	2.05	7.9	2.228
	After 100 Iterations				
1.5	75.09	8.9	82.33	0.069	82.334
5.5	12.40	52.3	25.80	0.62	25.964
9.5	1.08	51.6	2.21	0.64	2.228

As an example of the usefulness of the SOR technique the example of a finite cylindrical conductor coaxial with a larger radius and longer closed cylinder held at a different potential has been solved. This geometry is shown in Figure 5-3. Such a deceptively simple looking problem is beyond closed form solution, but by employing SOR methods (Equation 5-12 and 5-18) the problem can be solved in short order. The matrix map of solutions results in the equipotentials plotted in Figure 5-4.

In Figure 5-5 we show a second cylindrically symmetric system that is intractable by analytic methods, yet presents no real difficulties for an SOR treatment. (This particular case is actually a prototype of an electrostatic particle focusing system that we employ in a recoil-mass time-of-flight spectrometer.) The potentials obtained from an SOR treatment of the appropriately scaled system will be used in calculating trajectories in such a region. The equipotentials that result from an SOR solution of this electrostatic problem are shown in Figure 5-6.

After gaining some experience in field calculations and the estimation of the best relaxation factor to use, we began the calculation of the potentials that correspond to our TOF system. The calculations were accomplished in two parts: (1) the acceleration zone and (2) the drift zone. This was possible because the grounded mesh separating the acceleration zone provides a natural boundary surface for

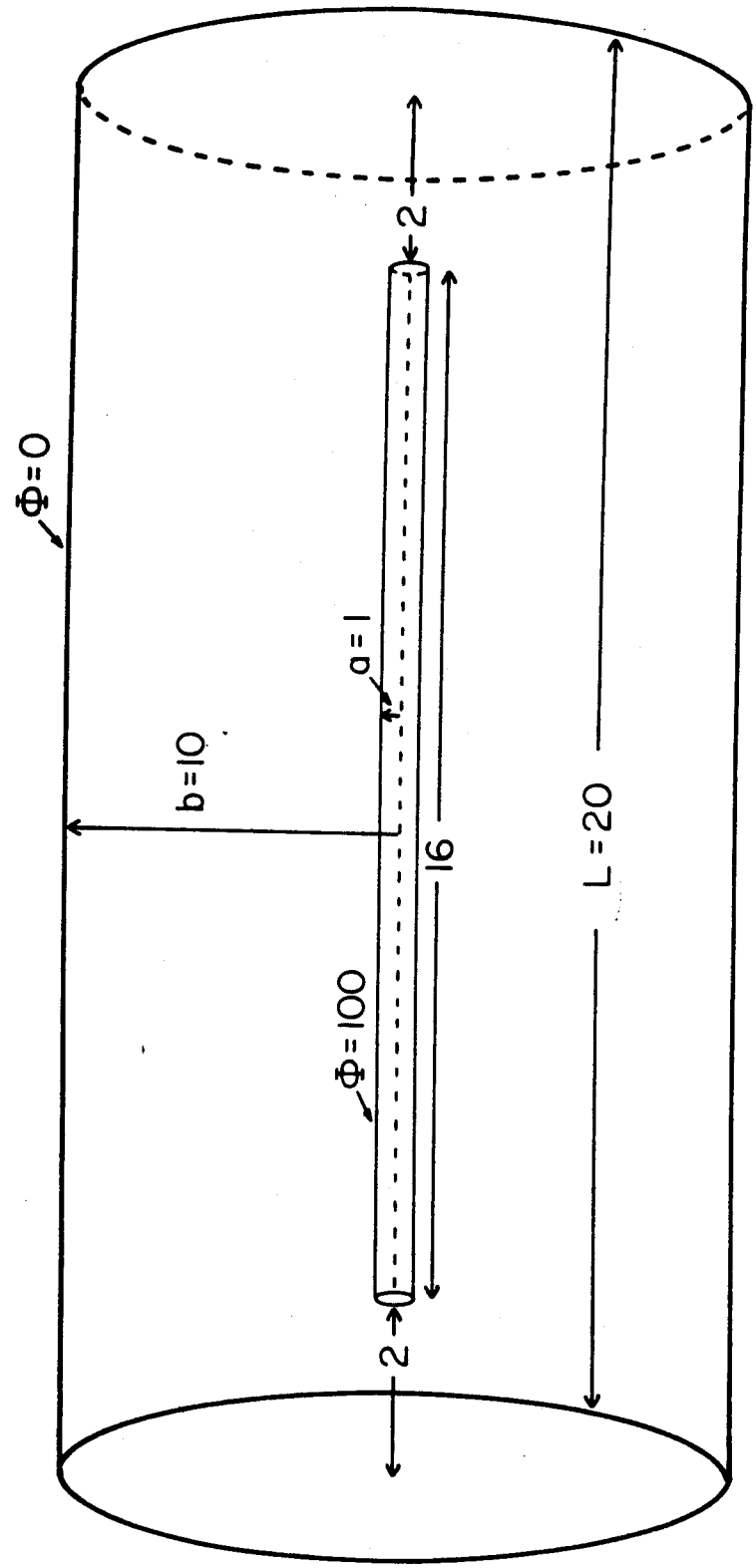

Figure 5-3. Finite cylindrical conductor held at Φ = 100, enclosed in larger grounded cylinder.

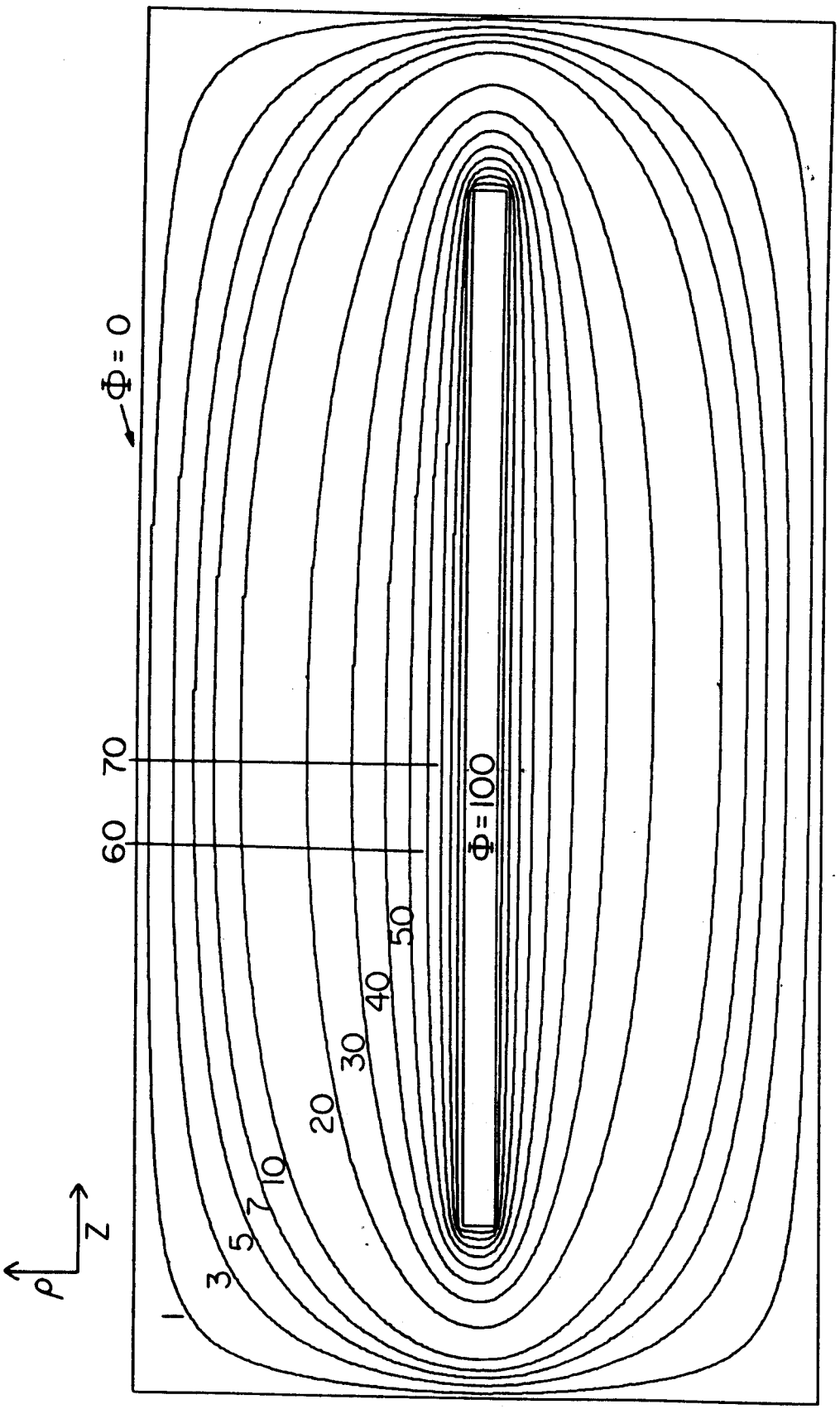

Figure 5-4. Equipotentials resulting from SOR solution to problem geometry of Figure 5-3.

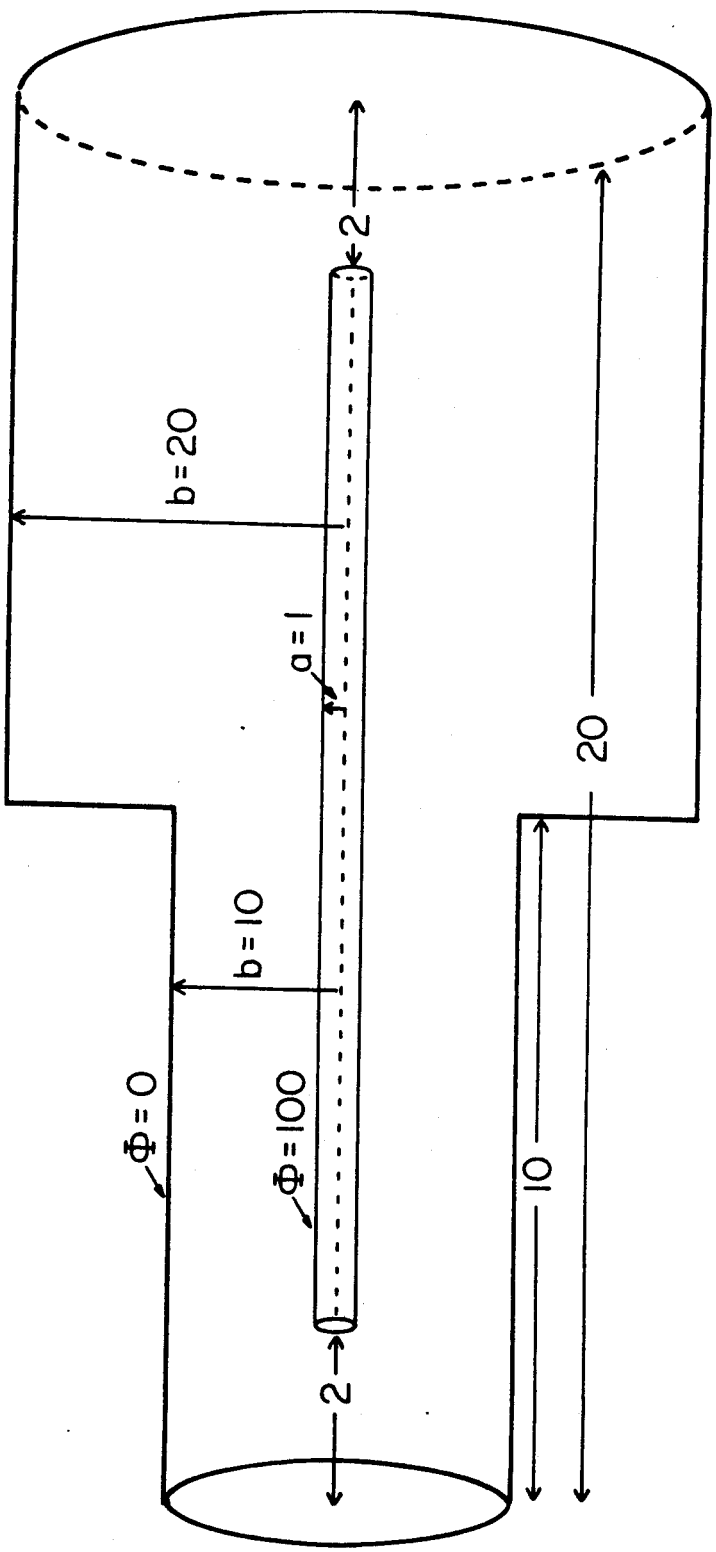

Figure 5-5. Finite cylindrical conductor (with Φ = 100) enclosed in grounded outer conductor that abruptly expands radius by a factor of two.

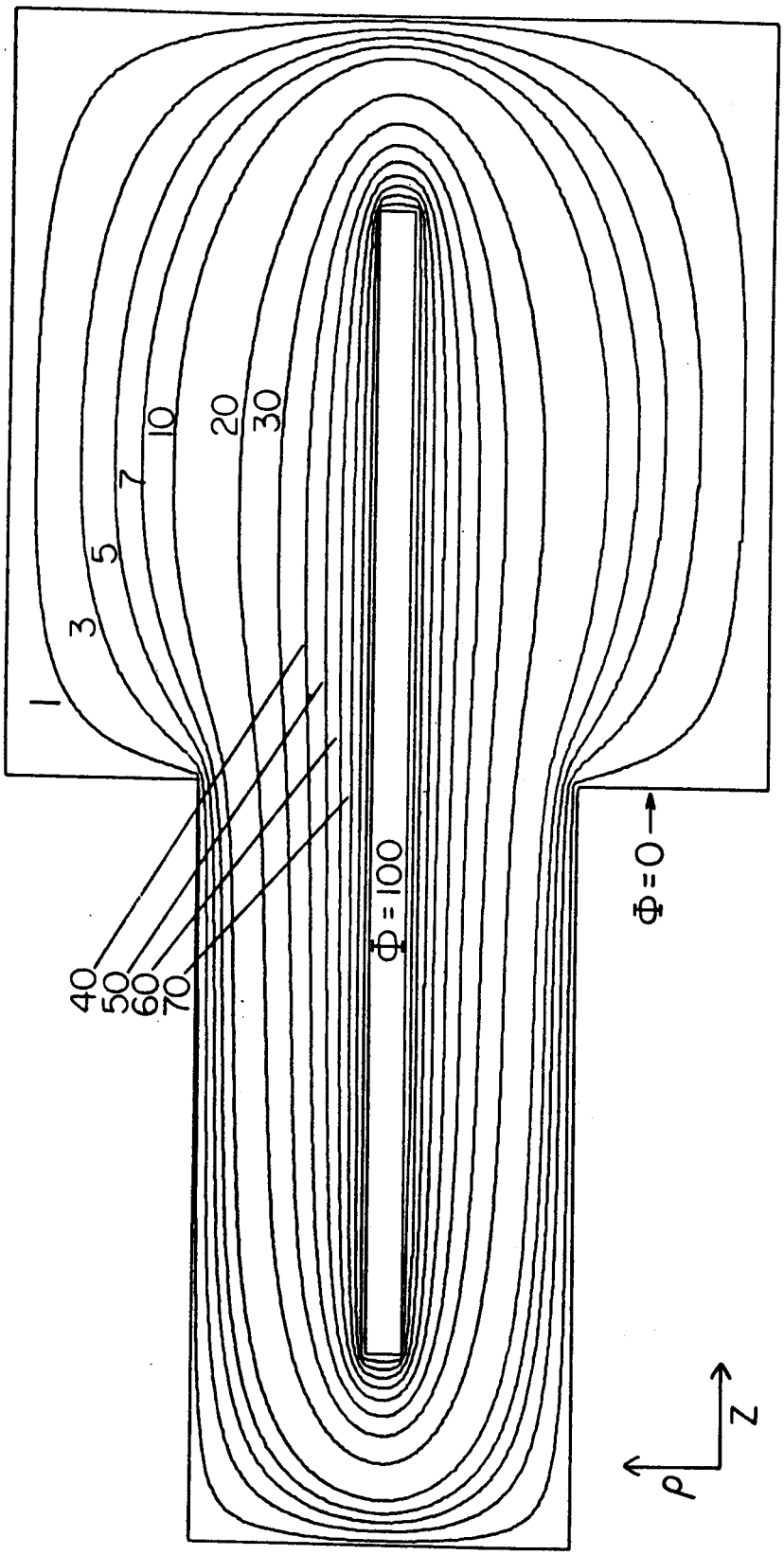

Figure 5-6. Equipotentials resulting from SOR solution to problem geometry of Figure 5-5.

both regions. This allows us to use the mesh plane as a boundary surface for both portions of the calculation.

Acceleration Zone

The acceleration region consists of a circular stainless steel plate held at 6 kV, a fine wire mesh disc at ground and a boron nitride (BN_3) insulating support connecting the two plates. Basically it is a cylindrical capacitor with a dielectric "ring" connecting the two plates. The radii of the charges plate and the mesh disc were both 1.83 cm. The length of the dielectric and therefore, the separation of theplates was 1.67 cm. The thickness of the insulating support was 0.47 cm. The inclusion of the eielectric in our model complicates the calculation somewhat since we no longer have pure Dirichlet boundary conditions on all surfaces. At the surface of the dielectric we have Neumann boundary conditions. Dirichlet boundary conditions mean that the value of the function is specified on a particular surface while Neumann boundary conditions mean that a condition on the derivatives of the function are specified. In electrostatics the relevant Neumann boundary condition is that the normal component of the electric displacement vector, D_n must be continuous. As a result the averaging equation for the potential presented in the previous section is not valid at the surface of the

dielectric. However the continuity of the normal component of the electric displacement can be translated into an equivalent expression using the finite divided differences of the potentials. Using this method one can then obtain a new expression for the potential at the surface of the dielectric. The relevant equation is

$$\Phi_{i,j} = (\Phi_{i-1,j} + \varepsilon_D \cdot \Phi_{i+1,j})/(1 + \varepsilon_D) \qquad (5\text{-}24)$$

where ε_o and ε_D are the dielectric constants for vacuum ($\varepsilon_o = 1$) and BN_3 ($\varepsilon_D = 4.08$), respectively. This expression was used at the inner and outer surfaces of the dielectric. A further complication in this treatment was that the Neumann condition on the outer surface leaves the potential unfixed on any surface in the rho direction which is an unstable situation. There are a number of ways to deal with this problem (see (Ac70)), the easiest and most straightforward is to "enclose" the entire acceleration zone in a large cylindrical box at a fixed potential. Physically this is very reasonable since in actuality the acceleration zone is encased in a vacuum chamber that is held at ground. This was the approach we chose to utilize. Our mesh step was .0235 cm enabling us to place 20 nodes in the insulator along the ρ direction. Two hundred iterations were performed until the maximum fractional change in the mesh was less than a part in 10^4. Shown in

Figure 5-7 is the equipotentials resulting from the over-relaxation calculations for the acceleration zone. The first nine lines represent drops in potential of 0.6 kV as one moves from left to right -- the direction of motion for a positively charged species. The spacing of these equipotentials is fairly regular which indicates the electric field strength is uniform. This is especially true along the axis of symmetry ($\rho = 0$) as can be seen from Figure 5-8. The top curve is a plot of the Z component of the electric field (at $\rho = 0$) as a function of distance from the charged plate. This component is relatively constant throughout the acceleration zone, the total drop in field strength is about 5% of the maximum. From these considerations one would expect a positively charged ion to undergo a uniform acceleration in the Z direction. Now if we follow one of the equipotentials in the first half of this zone it begins to bow slightly as we move away from $\rho = 0$. This indicates the presence of a ρ component of the electric field. The lower curve in Figure 5-8 shows the ρ component of $\vec{E}$ as a function of the distance from the symmetry axis. This particular curve was calculated at $Z = .5$ cm. As required by the Neumann boundary conditions the electric displacement normal to the surface is continuous at the interface of facuum and the dielectric. However, the electric field component normal to the surface has a discontinuity at this interface. This implies the

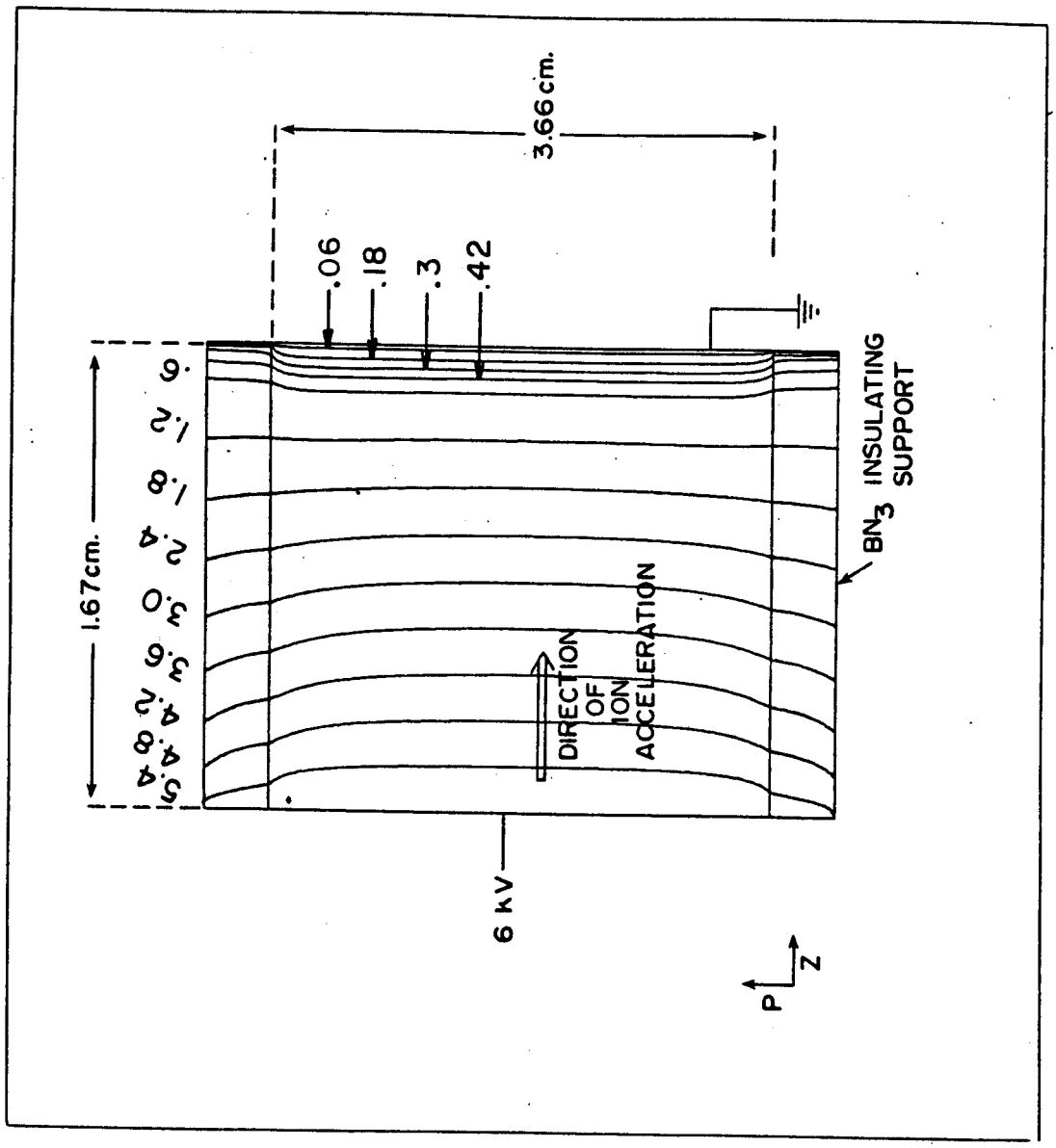

Figure 5-7. Equipotentials in the acceleration zone calculated by overrelaxation method.

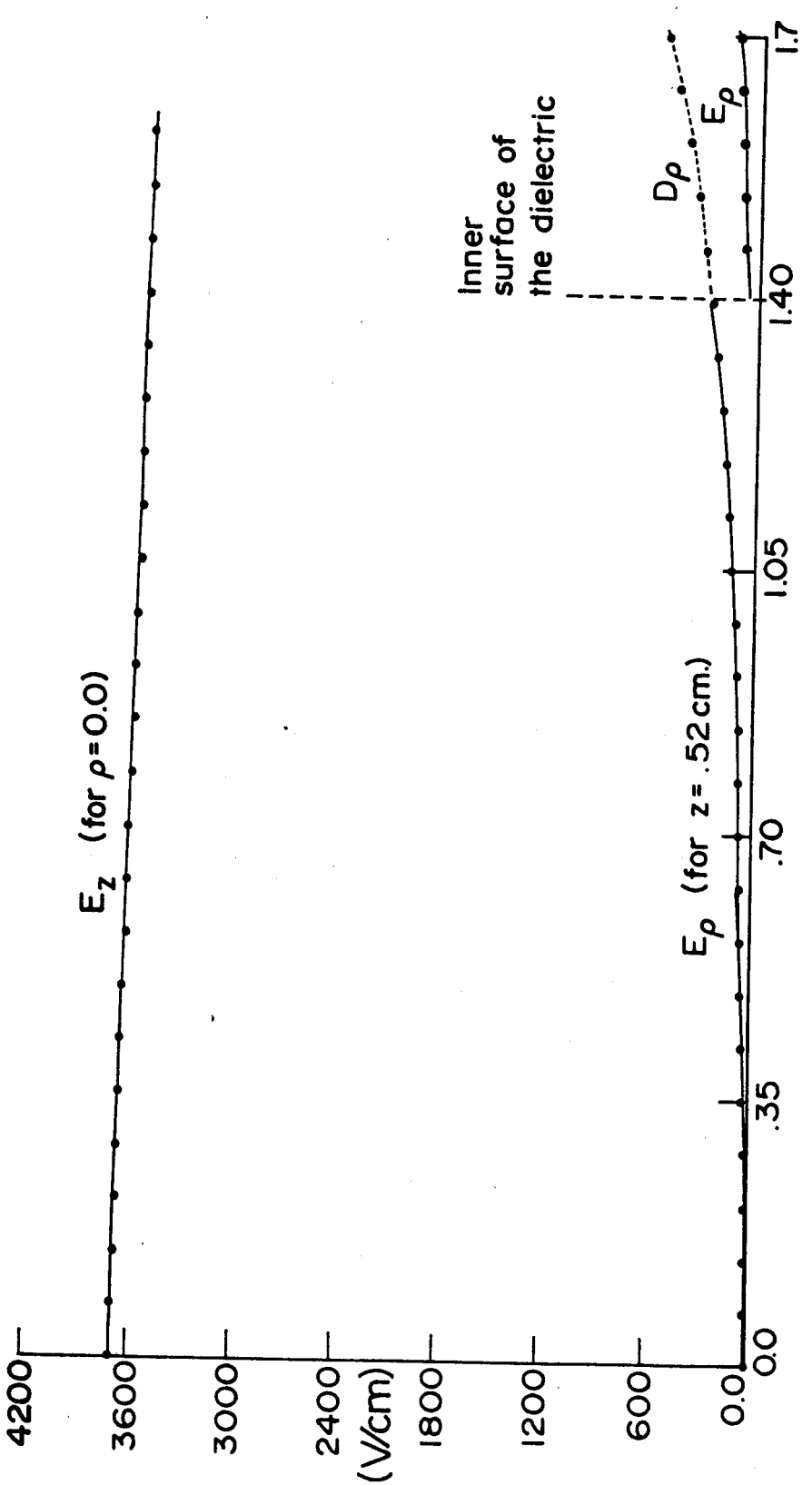

Figure 5-8. Example of Z and ρ components of the calculated electric field in the acceleration zone. For E_z curve x = z, for E_ρ curve x = ρ.

presence of a surface charge. There is indeed a surface charge, it is the induced polarization charge resulting from the external applied E field.

The ρ component of the field is much weaker than the Z component, its maximum value is about .08 times the Z part. Nonetheless it is a defocusing mechanism through much of the acceleration zone. This effect is most pronounced in the first three quarters of the region. Also the field in the ρ direction increases as the distance from the center increases. Therefore particles starting out far from the center of the collection plate should be most strongly affected. This is one reason for focusing the spray on center as best as possible.

Drift Zone

Once the recoil ions have passed through the wire mesh disc it enters the drift zone region. The region is made up of a small radius wire (0.0025 cm) concentric with a much larger radius pipe. Ideally this was meant to provide a logarithmic potential to focus the recoils onto the CEMA detectors at the end of the flight path. It was hoped that only an electric field in the ρ direction would result from this configuration. Unfortunately the wire can't be infinitely long so it has to start and end somewhere. This means that near the end of the wire the field are not purely functions of ρ, they have a dependence on Z that is very

difficult, if not impossible, to determine analytically. Another nonideal aspect to the real geometry is a sudden expansion in the radius of the outer conductor. This expansion, which occurs about 1/3 m from the acceleration region, results in a change in radius from 1.83 cm to 5.2 cm. This discontinuity preserves the symmetry in the ρ direction but definitely destroys the Z symmetry in the area of the expansion. Hereafter I will refer to the area of the radius change as the expansion region. Obviously we must again employ numerical methods to solve Laplace's equation for the potentials in the flight tube. In setting up the problem there are immediate differences from the calculation on the acceleration zone. The first difference is an advantage. In the flight tube region there are only conducting boundaries to deal with, so only Dirichlet conditions are relevant. This means the relaxation codes are a bit simpler. The second difference is a practical disadvantage. As we pointed out earlier the step Δ should be scaled to characteristic linear dimension of the problem geometry. However in the flight tube region the most obvious scale is the radius of the wire -- 0.0025 cm. But if we used a Δ = 0.0025 cm for our .5 cm x 100 cm system we would require an array of nearly 80 <u>million</u> elements -- totally unrealistic for our computer. Increasing the step size alleviates the problem of array size only at the expense of potentially large errors creeping into the

calculation since the error goes as the square of the step size. In our studies on the relaxation technique applied to the geometry of Figure 5-3 we found that the potentials approached the idealized infinite wire case as we moved away from the wire end. At a distance on the order of the separation of the wire from the ground plane the potentials calculated are well approximated by a logarithmic form. In the flight tube the separation of the wire and the ground disc is about 7 cm so after roughly 10 cm down the wire we thought that the use of a logarithm in ρ would sufficiently describe the potential field distribution. This effectively reduced the number of array elements required for the Z direction. We still had to contend with the problem of the small radius of the wire for the remaining regions. Following a more intuitive than rigorous argument we decided to use the actual wire voltage as the boundary value for the appropriate $\rho = 0$ points (i.e., points in the wire) and to use a boundary at one small step size from the $\rho = 0$ points. The fixed value of the potential on this surface was obtained from the logarithmic form discussed previously. Basically we replaced the "real" wire with a "pseudo"-wire of a more manageable radius. This final approximation allows us to reduce our array size to a realistic number for computation. The final mesh step size was 0.0235 cm. In the expansion region we again used the method of employing the logarithmic form for the potential at a reasonable

distance from the radius expansion. The results of the calculations are shown in Figure 5-9 as a number of equipotentials. The effect of the wire ends are clearly displayed at both ends. At the end nearest the acceleration zone the equipotentials resemble cylindrical waves, the corresponding electric fields will have both ρ and z components. So in this region the ESPG is not focusing only in the radial direction. In fact, near the axis of the wire the effect of the particle guide is to accelerate predominately in the z direction. At the other end the field acts to focus the particles on the CEMA detectors and also to deaccelerate them in the z direction. At the expansion region we can easily see the field "response" to the sudden radius change, the equipotentials seem to "expand" to fill the suddenly enlarged region of space available. The effect of this part of the fields will be a perturbation on particle trajectories that had been established as stable by the time they reach this part of the system. In a sense we can view the expansion as resulting in an easing of the attractive force that a charge particle "feels" as it passes through this region. The net effect is a defocusing of particles that had made it down a third of the flight path length. In the remaining regions the equipotentials are parallel to the wire with no real z dependence as we should expect. These regions, away from the discontinuities, make up about 80% of the system length and act to focus in the radial direction only.

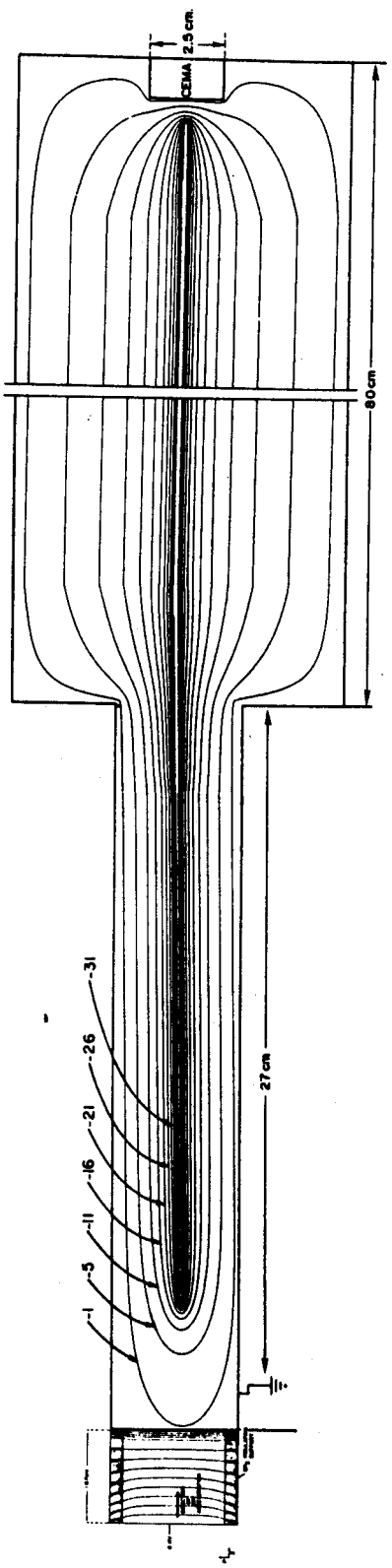

Figure 5-9. Equipotentials in the drift zone calculated by overrelaxation method.

Calculation of Particle Trajectories

The relaxation calculations just described allow us to obtain the electrostatic forces acting on a charged particle passing through our system. We are now in a position to calculate particle trajectories. This means we will integrate an appropriate set of equations of motion. For our case this set will be the Lagrange equations for a charged particle in an external electric field. In cylindrical coordinates we have

$$m \frac{d^2\rho}{dt^2} = \rho\dot{\phi}^2 - q \frac{\partial \Phi}{\partial \rho} \tag{5-25}$$

$$m \frac{d^2}{dt^2} (\rho^2\dot{\phi}) = -q \frac{\partial \Phi}{\partial \phi} \tag{5-26}$$

$$m \frac{d^2z}{dt^2} = -q \frac{\partial \Phi}{\partial z} \tag{5-27}$$

For our case the electrostatic potential, Φ is independent of the angle ϕ so the quantity $m\rho^2\dot{\phi}$ is a constant of the motion. Actually this quantity represents the angular momentum of the particle about the z axis, so we have

$$L = m\rho^2\dot{\phi} \tag{5-28}$$

This constant reduces the number of equations to be solved to two and allows us to eliminate the variable $\dot{\phi}$ from the remaining set. The resulting equations, after some simple algebraics are:

$$\frac{d^2\rho}{dt^2} = \frac{L^2}{m^2\rho^3} - \frac{q}{m}\frac{\partial\Phi}{\partial\rho} \qquad (5\text{-}29)$$

$$\frac{d^2z}{dt^2} = -\frac{q}{m}\frac{\partial\Phi}{\partial z} \qquad (5\text{-}30)$$

The electrostatic potentials and their derivatives are obtained from our calculated potentials by interpolation. We have used a Lagrange double 3-point form which is discussed in more detail in Appendix III.

Now we must choose a method for integrating the equations of motion. The most common numerical algorithms are the Runge-Kutta and the Predictor-Corrector methods. Each of these are prototypes of a general class of integrators. Even though these approaches are well documented and developed, the treatments are all in numerical analysis texts. For the sake of clarity I will give a brief description and comparison of the Runge Kutta and Predictor-Corrector algorithms.

For this discussion we will restrict ourselves to first

order equations since the extension to higher order equations is straightforward. By definition a first order equation has the form

$$\frac{dy}{dx} = f(x,y) \tag{5-31}$$

We want to obtain a solution y(x) that satisfies (5-31) and a specified initial condition. Since we can't solve for y(x) analytically, we approximate the true solution at discrete subintervals of the independent variable x. Considering equal sized subintervals the step size, Δ is

$$\Delta = \frac{b-a}{n} \tag{5-32}$$

where n is the number of subintervals and [a,b] is the range of the integration. With this defintion of the step size, our problem is to obtain approximations, y_i to y(x) at a set of base points, x_i where

$$x_i = x_o + i\Delta \qquad i = 0, 1,2,\ldots n \tag{5-33}$$

and

$$y_i \simeq y(x_i) \tag{5-34}$$

The various procedures to accomplish this goal can be divided into two groups, one step and multistep methods. Runge-Kutta methods are a common example of one step methods. These allow one to calculate y_{i+1} using only the differential equation and information at the point x_i, (i.e., y_i). Multistep methods require values of y_i and $f(x_i, y_i)$ for several different points, earlier and possibly later points. The predictor-corrector methods are a class of multistep methods.

All Runge-Kutta methods have the form

$$y_{i+1} = y_i + \Delta \cdot g(x_i, y_i, \Delta) \tag{5-35}$$

Here g is simply an approximation to f(x,y) on the subinterval $x_i \leq x \leq x_{i+1}$. The usual procedure is to express g as a linear combination of derivative evaluations on the integration interval. Each evaluation is used to predict a better estimate of y_{i+1} which will then be used to obtain an improved derivative estimate. For our calculations we started with a fourth order method due to S. Gill (Ca69). The algorithm is

$$y_{i+1} = y_i + \frac{\Delta}{6}(K_1 + a_i \cdot K_2 + a_2 \cdot K_3 + K_4) \qquad (5\text{-}36)$$

with

$$a_1 = 2(1 - 1/\sqrt{2}) \qquad (5\text{-}37)$$

$$a_2 = 2(1 + 1/\sqrt{2}) \qquad (5\text{-}38)$$

$$K_1 = f(x_i, y_i) \qquad (5\text{-}39)$$

$$K_2 = f(x_i + \Delta, y_i + \Delta \cdot K_1/2) \qquad (5\text{-}40)$$

$$K_3 = f(x_i + \Delta/2, y_i + (-\frac{1}{2} + 1/\sqrt{2})\Delta K_1) \qquad (5\text{-}41)$$

$$K_4 = f(x_i + \Delta, y_i - \Delta \cdot K_2/\sqrt{2} + (1 + 1/\sqrt{2})\Delta \cdot K_3) \qquad (5\text{-}42)$$

The K's are evaluated successively in ascending order. Although the formulas appear a bit long when translated into a computer code the algorithm is very simple and compact.

The predictor-corrector algorithms are more complex than the corresponding Runge-Kutta routines. For the sake of brevity, we will present a cursory description. For a fuller and more rigorous discussion see (Ha62). The

first step in the predictor-corrector method is to fit a polynomial to the three most recent points of the derivative then extrapolating this polynomial to the next step and integrating the fitted polynomial to obtain an increment that gives y_p. This y_p is the predicted value. This value is then used in the original differential equation to obtain a better estimate of the derivative at the point we previously extrapolated to, i.e., x_{i+1}. Now we again fit a polynomial but this time to our new derivative estimate and the derivative at earlier points. We integrate under this new polynomial to obtain a second estimate of y at the next x step. This second estimate is called the corrected value, y_c. Next we check the difference between y_p and y_c. If it is too large we can repeat the procedure with a smaller step size. If too small we can proceed with a larger step size. The most important point to note is that at each step forward we have available an internal measure of the accuracy of the integration. The measure is the difference between the predicted value and the corrected value. One disadvantage of the multistep method is that one must use another method to start the integration. This is because in the very first part of the algorithm a polynomial is fitted to earlier points that are not available at the outset. For our computations we started with the Gill form of the Runge-Kutta routine. After advancing three steps with the Runge-Kutta routine

we then switched over to Hamming's Predictor-Corrector method (Ca69). The form of this algorithm is

Predictor

$$p_{i+1} = y_{i-3} + \frac{4\Delta}{3}(f_i - f_{i-1} + 2f_{i-2}) \qquad (5\text{-}43)$$

Modifier

$$m_{i+1} = p_{i+1} + \frac{112}{121}(c_i - p_i) \qquad (5\text{-}44)$$

Corrector

$$c_{i+1} = 1/8\ (9y_i - y_{i-2} + 3\Delta(f(x_{i+1}, m_{i+1}) + 2f_i - f_{i-1})) \qquad (5\text{-}45)$$

Error

$$e_{i+1} = \frac{9}{121}(c_{i+1} - p_{i+1}) \qquad (5\text{-}46)$$

Final Value

$$y_{i+1} = c_{i+1} - p_{i+1} \qquad (5\text{-}47)$$

The term e_{i+1}, the truncation error, is checked at each step to determine whether the step size should be changed.

If we compare the two algorithms just presented it can be seen that the Runge-Kutta routine requires four separate

evaluations of the derivative term while the Hamming predictor-corrector only needs two evaluations of f(x,y). Generally this difference will mean that the predictor-corrector algorithm should be faster than the Runge-Kutta. In an attempt to see how significant the difference in speed of the two algorithms, we ran our computer routines for each algorithm on a number of different analytical functions.

In Table V-2 are the results of the comparison, in every case the Runge-Kutta algorithm required at least 40% more time than the predictor-corrector routine. This is a significant difference. When we begin calculating trajectories in our calculated fields the derivative evaluations involve a number of interpolations in the field map. These interpolations can be very time-consuming so we want to keep these derivative evaluations to a minimum. This is another advantage of the predictor-corrector method.

For the actual trajectory calculations we used the Hamming method with a variable step size. Whenever the truncation error term was greater than 1×10^{-5} the integration step size was cut in half and the procedure continued. If the error term was less than 1/50 of the upper limit on the error then the integration step size was doubled. This was very useful for our problem since the particle traverses long regions of slowly varying potentials on much of its flight path so the step size can be very large. In the more rapidly changing regions the step size reduces in

Table V-2. Comparison of Speeds for Runge-Kutta vs. Predictor-Corrector Routines.

Function	Time of Calculation for 5000 Steps (in seconds)		
	Predictor-Corrector	Runge-Kutta	RK/PC
tanh(x) - x	15	23	1.5
exp(x) - x - 1.	15	21	1.4
sech(x) - 1.	16	22	1.4
cosech(x) + 1	19	31	1.6
cosh(x) - 1.	15	21	1.4
sinh(x) - x	15	21	1.4
log(x) - x + 1.	16	22	1.4
x + 1/x	16	22	1.4
cos(x)	15	21	1.4
sin(x)	15	20	1.3

response. In addition to the error monitor we checked the constancy of the particle's total energy. Since we have an electrostatic problem the sum of the kinetic and potential energy should be a constant. This was true for our calculations to one part in 10^5. Special care had to be taken in crossing from the acceleration zone into the drift zone. If one does not insure that one of the integration steps "lands" on the grounded disc position then it appears that the electric field in the acceleration region continues to act on the particle a short distance into the weak field zone. The result of this is strong nonconservation of energy and very incorrect results. After integrating down the length of the flight tube the particle's ρ position was checked to determine whether it was within the radius of the CEMA detectors (ρ_{CEMA} = 1.25 cm). If it was, then the time, ρ position and velocities are recorded and the event is considered a successful hit.

CHAPTER VI

THEORETICAL MODELING RESULTS

In the previous chapter we presented the tools that will be required to model a specific time-of-flight peak that has been experimentally observed. In the following section we shall present the formal aspects of the problem. This will include clearer definitions of 1) our approach, 2) the particular isotope chosen for study, and 3) the most effective use of the mathematical tools discussed previously.

1. Approach

Basically our problem is that we have, as a physical observable, a distribution of events as a function of their associated times-of-flight through the SIEGFRIED system. Our goal is to relate the observed distribution to a reasonable set of initial conditions that will be related to the particular isotope of interest. Since we are interested in correlating the particles' initial recoil energy to the observed peak broadening, the kinetic energy is an important initial parameter that must be specified. Also, the source of the recoils is a finite size spot, so we should include

this fact in the initial distribution. Fortunately the source spot is approximately circular and well-centered on the collection plate. After passage through the SIEGFRIED TOF system the initial particle distribution in position and energy is transformed into the observed distribution in time-of-flight. If we denote the initial distribution as $N_o(E,\rho_o)$ and the final distribution $P_f(T)$, then the process of measurement can be represented as shown below:

$$N_o(E,\rho_o) \longrightarrow \text{SIEGFRIED} \longrightarrow P_f(T)$$

Mathematically we will consider the action of SIEGFRIED on the initial distribution as expressed by an integral transform of the form:

$$P_f(T) = \iiint S(E,\rho_o,T,\rho_f)N_o(E,\rho_o)d\rho_o dE d\rho_f \qquad (6\text{-}1)$$

Here $S(E,\rho_o,T,\rho_f)$ represents the transformation of a particular kinetic energy E and position ρ_o distribution in the energy and position interval $dEd\rho_o$. (The effect due to the finite size of the detector is taken into account by integrating over final positions with ρ_f less than or equal to R_{det}, the radius of the CEMA detectors.)

Ideally $S(E,\rho_o,T,\rho_f)$ and $N_o(E,\rho_o)$ would be expressible in a closed form. Then we could merely integrate and solve the problem easily. Even more appropriate would be to

invert our approach: suppose we express our integral transform, Equation 5-1, as

$$P_f(T) = \mathscr{L} N_o(E,\rho_o) \qquad (6\text{-}2)$$

Here $\mathscr{L}$ represents the integral transform operator. Now <u>if</u> an inverse of $\mathscr{L}$ exists, then we can invert the problem. Denoting the inverse by $\mathscr{L}^{-1}$ we get from Equation 6-2

$$N_o(E,\rho_o) = \mathscr{L}^{-1} P_f(T) \qquad (6\text{-}3)$$

This last form says that, by using $\mathscr{L}^{-1}$ on the observed final distribution $P_f(T)$, we can reconstruct the initial distribution function. That is precisely what we would like to do -- if we could.

The problem is that the kernel of the transform, S is not expressible in a simple form. We do know that solving the equations of motion for a set of initial conditions that result from a particular distribution will allow us to follow the time evolution of the distribution. This is the functional effect of S on the initial distribution, but we cannot "find" an inverse, so we are basically solving the problem in an unavoidably roundabout manner. We will assume a given initial distribution, predict a test distribution F(t) and compare this with $P_f(T)$, the observed distribution.

2. Choice for the Study

The particular isotope I have chosen for this modeling study is ^{23}Mg. It is a positron emitter with a half-life of 12.1 sec. The decay energy is typical of isotopes seen by SIEGFRIED (Q_{EC} = 4.056 MeV). 91% of the decay proceeds from the $3/2^+$ ground state of ^{23}Mg to the $3/2^+$ ground state of ^{23}Na. The decay has 70% Fermi fraction and 30% Gamow-Teller fraction (as defined in Chapter IV).

Experimentally ^{23}Mg is seen very strongly in the TOF spectrum resulting from ^{27}Al + 70-MeV ^{3}He (See Figure 3-1). Its TOF peak is the largest feature in the spectrum and is very well separated from other peaks in the spectrum. The shape is typical of TOF peaks we have observed, and the high number of counts in this peak allows us to fit it very well with SAMPO. This gives us good estimates of peak parameters such as the width and the tailing.

Finite Source

To take account of the finite source size we considered the source to be made up of 8 concentric rings. Each has a mean radius of n·(.075 cm) with n = 1,2,...8.

Initial Conditions

An important part of our modeling will be the integration of a large number of particle trajectories. While the integration codes are fast (roughly six complete integrations per minute) we want to be as efficient as possible. A very significant increase in efficiency can be obtained by eliminating initial conditions that result in trajectories that strike the boundaries of the system or are otherwise unreasonable. This is an important consideration and will be the focus of this section.

The maximum initial recoil energy, R is fixed by the decay energy as shown in Appendix II. If we denote the maximum kinetic energy of the electron by T_o (in MeV) and the mass of the recoil by A (in amu) then the maximum kinetic energy of the recoil R (in eV) can be obtained by the following equation from Appendix II

$$R = \frac{537}{A} T_o (T_o + 1.022) \qquad (6\text{-}4)$$

This is a bound on the square of the velocities. For ^{23}Mg the maximum kinetic energy of the electron is 3.03 MeV. (For positron emitters $T_o = Q_{EC} - 2m_e c^2$). The resulting maximum recoil kinetic energy is 290 eV.

By using a gross model of the TOF system and some

simple energy conservation arguments we were able to obtain rough limits on the transverse velocity and the angular momentum. To demonstrate this we use the geometry of Figure 6-1. In region I the electric field has only a Z component, at Z = d is a ground plane and region II has a potential that is purely logarithmic in ρ. This means that a particle of mass m and charge q starting from Z = 0 experiences only accelerations in the Z direction in region I and only ρ accelerations in region II. The system is cylindrically symmetric and so the angular momentum about the Z axis (L) is constant.

Consider a particle of mass m and charge q starting from Z = 0, $\rho = \rho_o$ with an initial kinetic energy R. In cylindrical coordinates

$$R = 1/2m(\dot{\rho}_o^2 + L^2/(m\ \rho_o)^2 + \dot{Z}_o^2) \qquad (6\text{-}5)$$

Since it starts from the plate held at 6 kV its potential energy is 6 keV. Denoting the potential energy by U, we have

$$U_o = 6 \text{ keV}$$

The total energy, E of the particle is conserved so

$$E = R + U_o = \text{constant} \qquad (6\text{-}7)$$

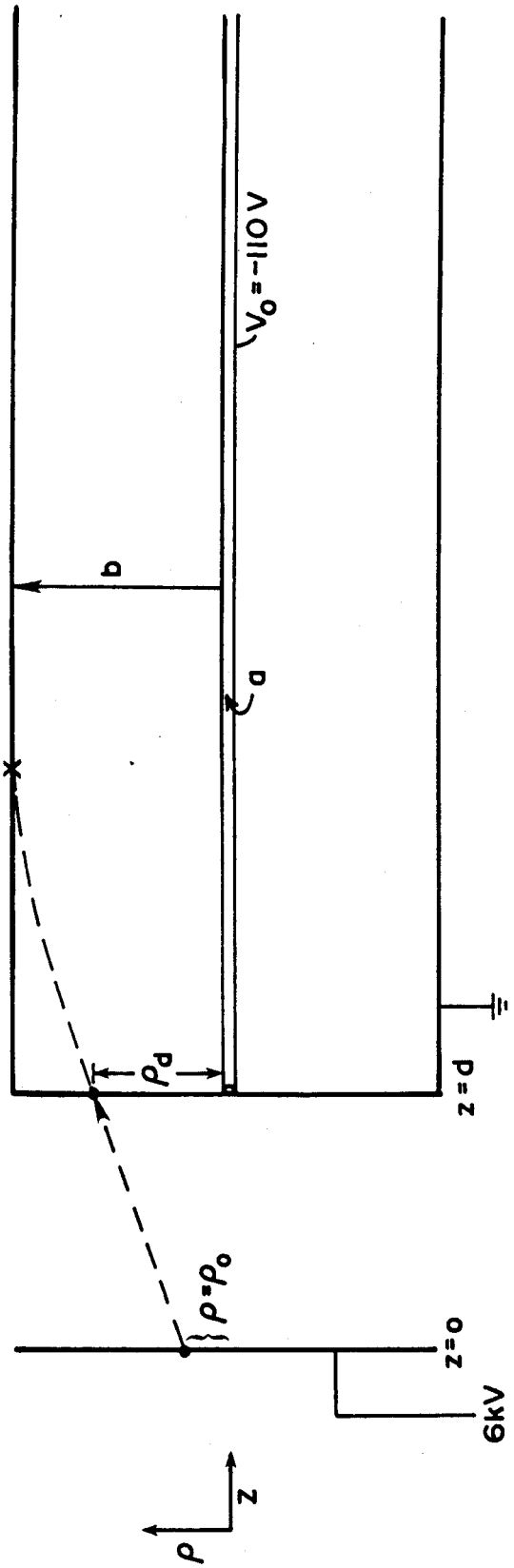

Figure 6-1. Approximate model of the TOF system.

In crossing the region I only the velocity in the Z direction is changed. When the particle reaches the ground plane it has a total Z velocity, $\dot{Z}(d)$

$$\dot{Z}(d) = Z_o^2 + \sqrt{2U_o/m} \tag{6-8}$$

The time necessary to cross region I is t_d, which is obtained in Appendix I as

$$t_d = \frac{md}{U_o}\left\{-\dot{Z}_o + \sqrt{\dot{Z}_o^2 + \frac{2U_o}{m}}\right\} \tag{6-9}$$

The ρ velocity is not constant if the angular momentum is nonzero, at $Z = d$ and $t = t_d$ we have

$$\dot{\rho}(t_d) = \dot{\rho}_d = \sqrt{\dot{\rho}_o^2 + \frac{L^2}{m^2}\left(\frac{1}{\rho_o^2} - \frac{1}{\rho^2}\right)} \tag{6-10}$$

There is drift across the region in the direction given by Equation AI-19, which for $t = t_d$ gives

$$\rho_d = \rho(t_d) = \rho_o \sqrt{\frac{[(\dot{\rho}_o^2 + (L/m\rho_o)^2)t + \dot{\rho}_o\rho_o]^2 + (L/m)^2}{(\dot{\rho}_o\rho_o)^2 + (L/m)^2}} \tag{6-11}$$

Now we consider the particle to be infinitesimally far from the ground disc at Z = d but now in region II where it fields a force due to the logarithmic potential in ρ. We assume the ρ position is given by Equation 6-11 and the ρ velocity by Equation 6-10. Again the total energy is constant but in addition the velocity in the Z direction is also constant so defining T as follows:

$$T = 1/2m\ (\dot{\rho}^2 + L^2/m^2\rho^2) \tag{6-12}$$

Then the quantity

$$T + W = \text{constant} = E_d$$

where W is the potential energy. In region II, W is

$$W = \frac{V_o}{\ell n(a/b)}\ \ell n(\rho/b) \tag{6-13}$$

V_o is the potential on the center wire, a is the radius of the outer conductor. Thus, at the beginning of region II

$$E_d = \frac{m\dot{\rho}_d^2}{2} + \frac{mL^2}{2\rho_d^2} + \frac{V_o}{\ell n(a/b)}\ \ell n(\rho_d/b) \tag{6-14}$$

Defining new quantities T_ϕ and T_ρ as

$$T_\phi(\rho) = \frac{mL^2}{2\rho^2} \tag{6-15}$$

$$T_\rho = \frac{m\dot{\rho}^2}{2} \tag{6-16}$$

we have

$$E = T_\rho(d) + T_\phi(d) + \frac{V_o}{\ell n(a/b)}\,\ell n(\rho_d/b) \tag{6-17}$$

If $\rho = b$, the particle has struck the outer boundary and its ρ velocity $\dot{\rho}$ and potential energy W are both zero, so:

$$E_d = T_\phi(b) \qquad (\text{At } \rho = b) \tag{6-18}$$

From Equation 6-17 we have

$$E_d = T_\rho(d) + T_\phi(d) + \frac{V_o}{\ell n(a/b)}\,\ell n(\rho_d/b) = T_\phi(b) \tag{6-19}$$

From Equations 6-10 and 6-16,

$$T_\rho(\rho_d) = T_\rho(\rho_o) + T_\phi(\rho_o)(1-(\rho_o/\rho_d)^2) \tag{6-20}$$

$$T_\phi(b) = T_\phi(\rho_o)\cdot(\rho_o/b)^2 \qquad (6\text{-}21)$$

Rearranging Equation 6-19 and substituting, we have

$$T_\rho(\rho_o) + T_\phi(\rho_o)(1-(\rho_o/b)^2) = \frac{-V_o}{\ell n(a/b)}\,\ell n(\rho_d/b) \qquad (6\text{-}22)$$

which gives bounds on the initial ρ position and velocity and angular momentum. Suppose initially the angular momentum is zero, then

$$T_\rho^{max}(\rho_o) = \frac{-V_o}{\ell n(a/b)}\,\ell n(\rho_d/b) \quad (\text{for } T_\phi(\rho_o) = 0 \qquad (6\text{-}23)$$

with

$$\rho_d = \dot{\rho}_o t_d + \rho_o \qquad (6\text{-}24)$$

This fixes the bound on the maximum initial ρ velocity. If $L = 0$, any initial velocity less than this maximum will not hit the outer wall. If we want the corresponding maximum angular momentum for $\dot{\rho}_o = 0$, then $T_\rho(\rho_o) = 0$

For $T_\rho(\rho_o) = 0$

$$T_\phi^{max}(\rho_o) = -V_o\,\ell n(\rho_d/b)/\{\ell n(a/b)\cdot(1-(\rho_o/b)^2)\} \qquad (6\text{-}25)$$

with

$$\rho_d = \rho_o \sqrt{1 + \frac{Lt^2}{m\rho_o}} \qquad (6\text{-}26)$$

Equation 6-25 sets a limit on the maximum angular momentum for a given initial ρ value, ρ_o. Actually, Equations 6-23 and 6-25 are transcendental, since T_ϕ and T_ρ enter into the logarithmic term through ρ_d. Nevertheless, they can be solved graphically accurately enough for our purposes. This was done and the results compared with limits on these quantities obtained from the actual numerical integration of the equations of motion as described in Chapter V. The results are given in Table VI-1. T^{pred} are the limits obtained from our simple argument just presented, and T^{num} are the corresponding bounds obtained from the numerical integration. Considering the simplicity of our gross model, the agreement is very good. The most severe deviations occur for larger values of ρ_o, where our assumptions about the field uniformity (pure Z field in region I, pure log(ρ) in region II) are most strained.

Once a simple form such as Equation 6-23 or 6-25 is available to estimate bounds, we can obtain numerical bounds, in a much more efficient manner. This is how the bounding curves shown in Figure 6-2 were obtained. To a precision of less than 1 eV the limits were independent of the Z velocity over the total range of U_Z.

To reiterate the function of these limit curves: they

Table VI-1. Comparison of Bound Values.

T_ρ^{Max} values

ρ_o (cm)	T_ρ^{pred} (eV)	T_ρ^{num} (eV)
.15	26	24
.3	21	19
.45	18	14
.6	14	10

T_ϕ^{Max} values

ρ_o (cm)	T_ϕ^{pred} (eV)	T_ϕ^{num} (eV)
.15	31	29
.3	27	28
.45	23	26
.6	20	24

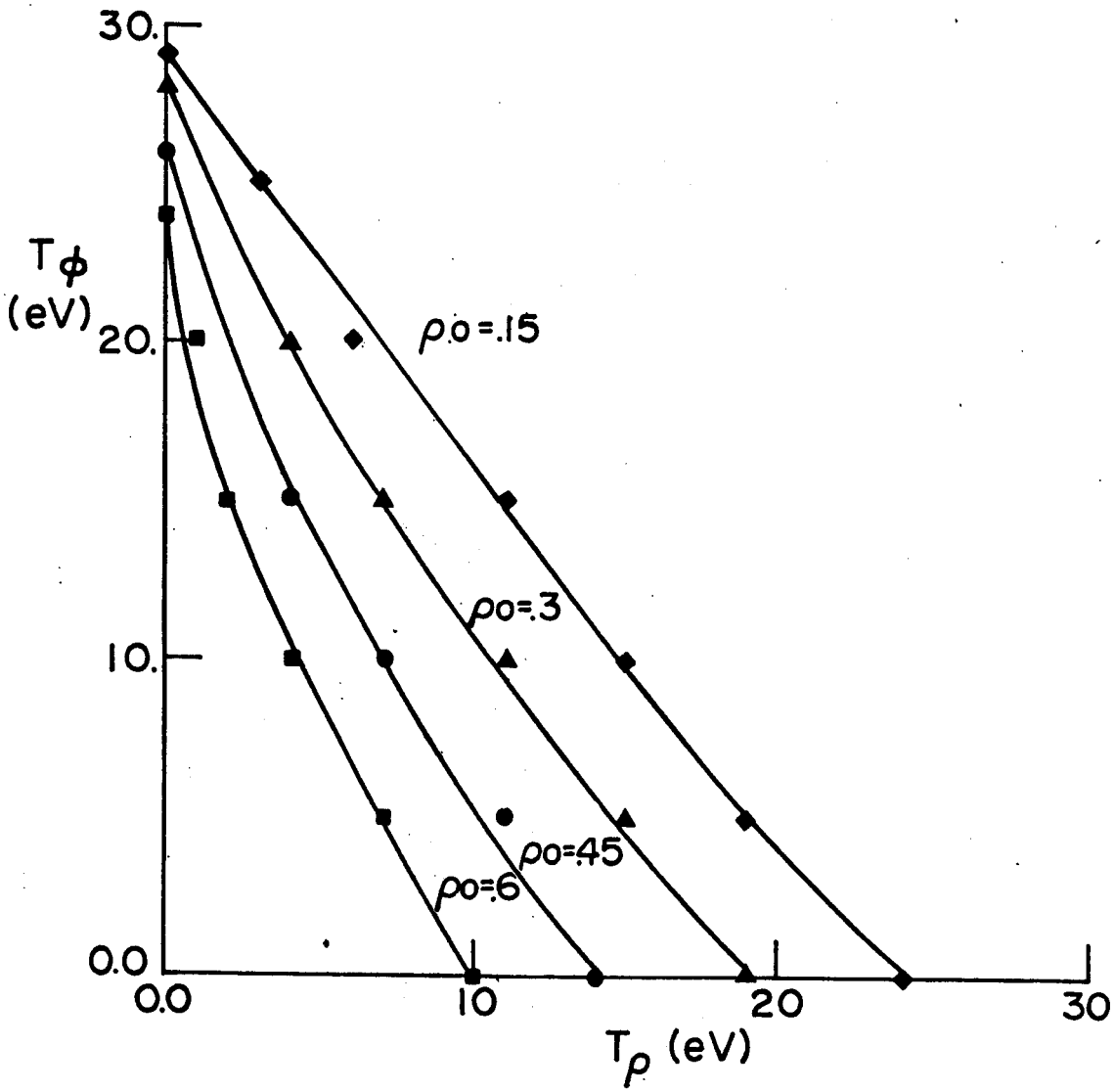

Figure 6-2. T_ρ - T_ϕ bound curves for several initial positions.

allow one to determine quickly if a set of initial velocities and position will lead to a trajectory that cannot span the flight length. For instance, suppose one set of initial conditions we might choose to integrate corresponds to $\rho_o = 0.15$, $T_\rho = 10$ eV, and $T_\phi = 30$ eV. Referring to Figure 6-2, we see that this set determines a point that lies above the bound curve labeled $\rho_o = 0.15$. This tells us that the resulting trajectory will end up striking the wall of the outer conductor and thus eliminates consideration of these initial conditions.

The usefulness of these limit curves cannot be overemphasized. They allowed us to eliminate quickly a very large number of integrations and to focus in great depth on potentially "successful" trajectories. By successful I mean trajectories that end with the final ρ position less than the radius of the CEMA detectors, which was taken as 1.25 cm, and the Z position equal to 110 cm, which is the length of SIEGFRIED.

When an event was successful, the time, initial and final positions, and velocities and total energy were filed. The results are best described graphically as shown in Figure 6-3. The curves here represent successful events for various initial ρ values as functions of the quantities T_ϕ and T_ρ defined earlier. The interpretation of these curves is that, for a set of initial conditions corresponding to a point below the curve (for the associated

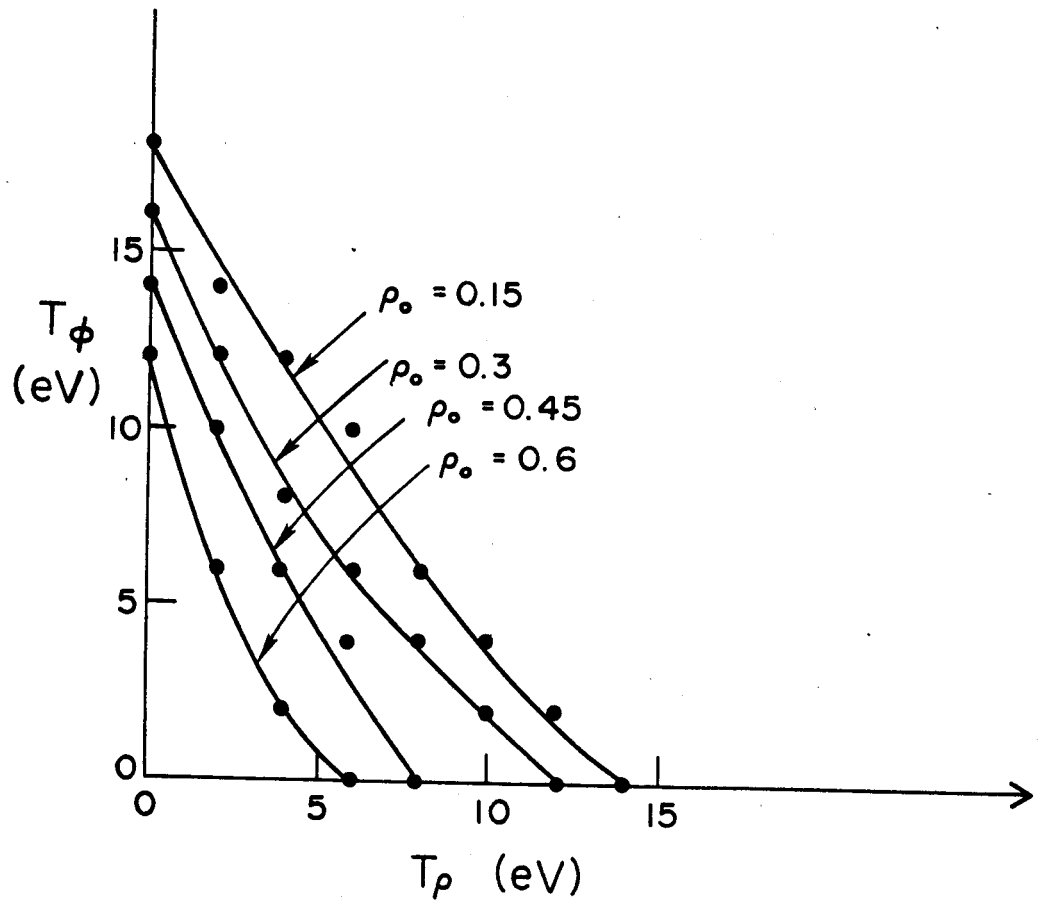

Figure 6-3. T_ρ - T_ϕ hit efficiency curves.

ρ_o value), we will obtain a successful event. In a manner of speaking, these plots represent detector hit efficiency curves. Comparison of Figures 6-2 and 6-3 seems to imply that both the limit curves and the hit efficiency curves have similar structure or relationships between T_ϕ and T_ρ. If one considers the area bounded by a particular curve in either Figure 6-2 or 6-3, we have a measure of the efficiency of the system. Comparing equivalent areas on each graph, it appears that roughly half the particles that make it down the flight tube without striking the outer wall, will be detected.

Although our system contains a number of apparently disruptive elements, the trajectories seem to have a smooth, consistent behavior. This is borne out by Figures 6-4 and 6-5, which are plots of the final ρ position (ρ_f) as a function of the quantity T_ϕ for various values of the ρ velocity. There is apparently some type of harmonic behavior exhibited by these curves. Note that the maximum of each curve appears closer to the origin in Figures 6-4 and 6-5 in a very regular pattern dependent on the ρ velocity. Actually, it appears that all the curves (except $T_\rho = 0$) are very similar but differ in some type of phase factor dependent on T_ρ. It would be a useful exercise to attempt a decomposition of these curves by Fourier decomposition. The sharp takeoff in amplitude shown by the curves in Figure 6-5 suggests some type of Bessel functions might be reasonable for the analysis.

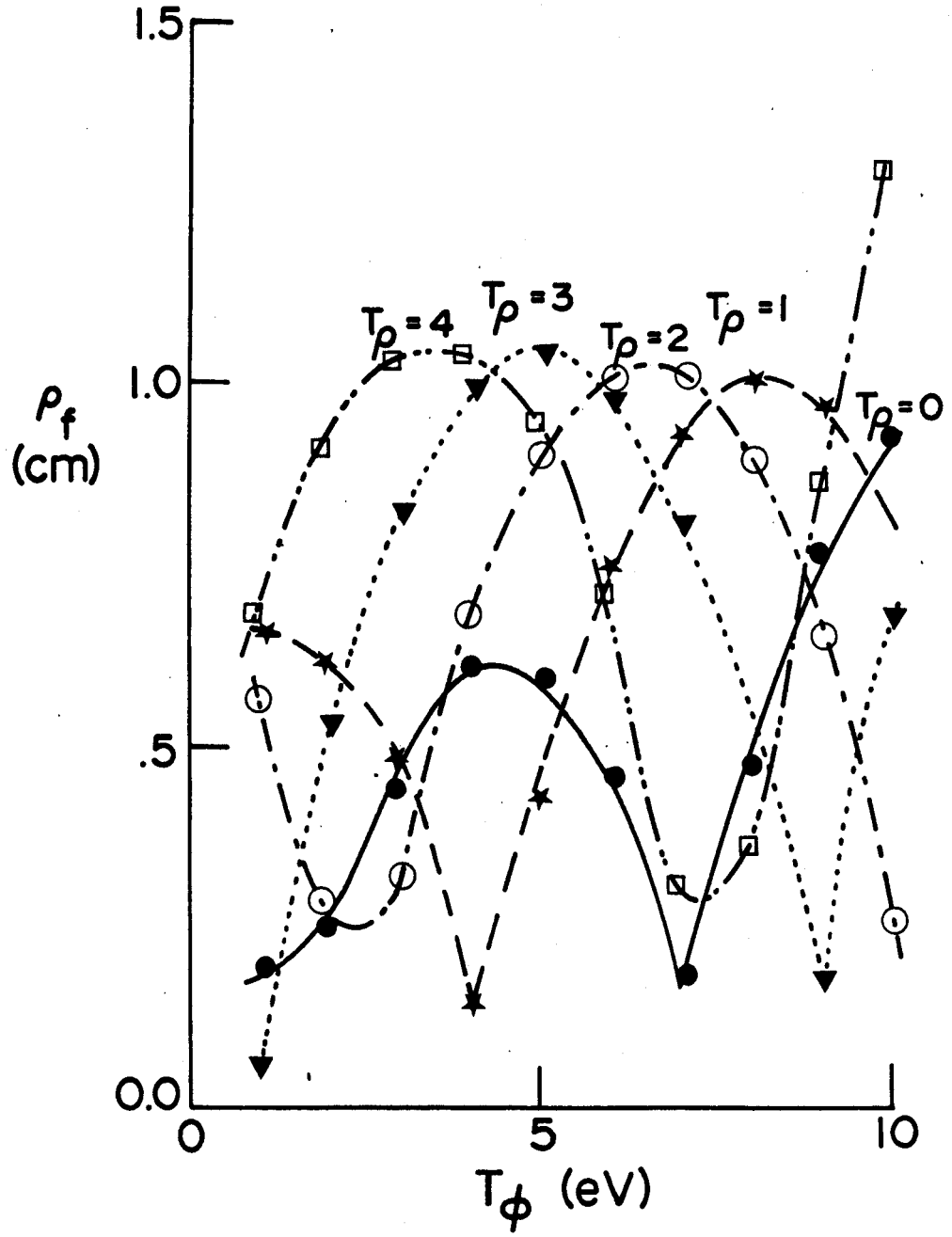

Figure 6-4. Graphs of final ρ position as function of T_ϕ (for fixed initial ρ velocities).

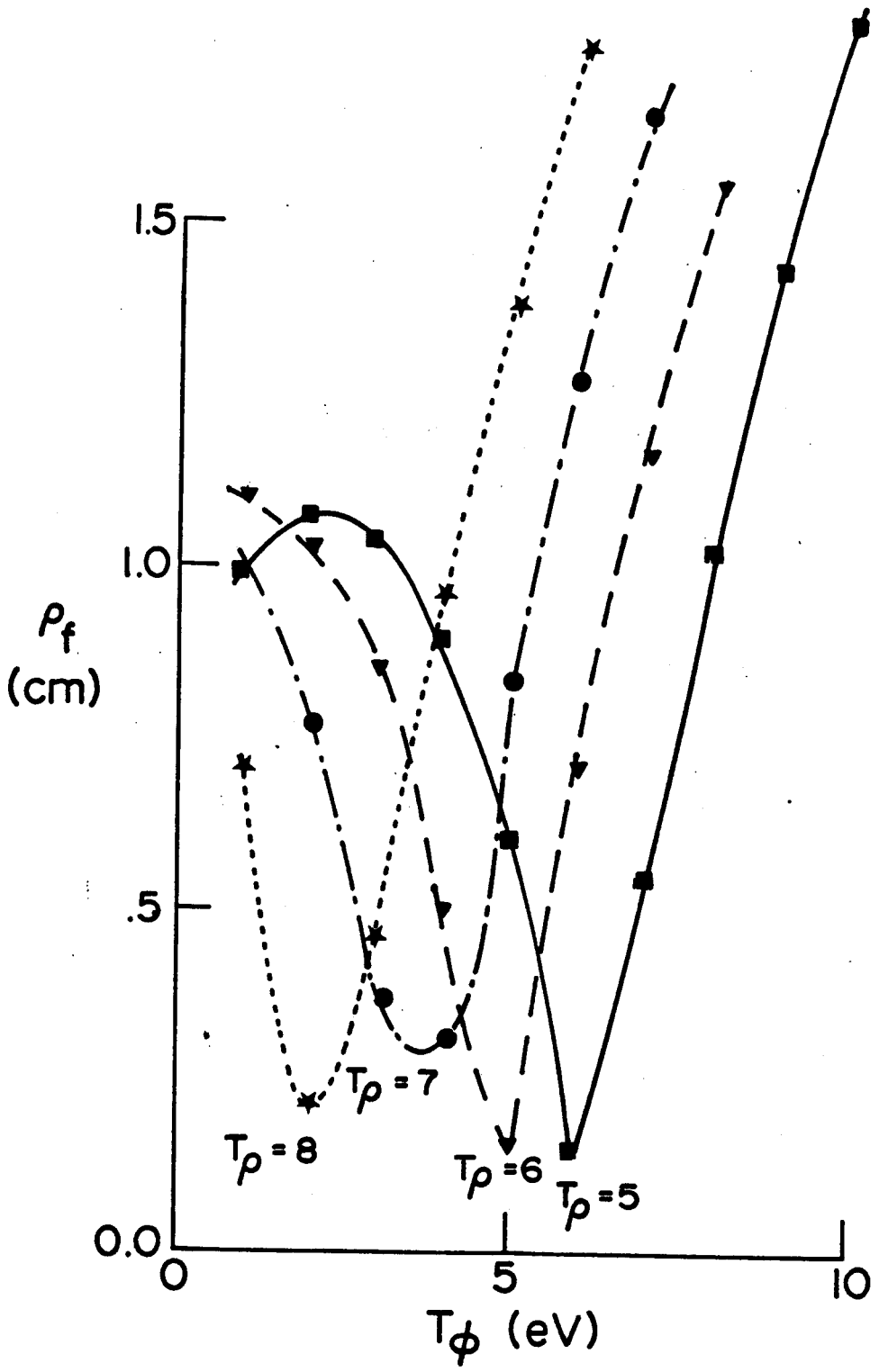

Figure 6-5. Graphs of final ρ position as function of T_ϕ (for fixed initial ρ velocities).

Initial Energy Distributions

In our parametric fits to the observed peak widths discussed in Chapter IV, we assumed various forms for energy distributions for the recoil ions. These forms included (1) a flat energy distribution, (2) a Fermi distribution, (3) a Gamow-Teller decay distribution, and (4) mixed F-GT distributions. To include such distributions in our modeling study means we will be making a number of different choices for the term $N_o(E,\rho_o)$ in Equation 6-1. The flat distribution means that N_o is constant. The Fermi and Gamow-Teller distributions are shown in Figure 6-6. These plots were obtained from formulas given in (Jo63). The distribution function for the mixed decay corresponding to ^{23}Mg is shown in Figure 6-7. Even though we will be using the various distribution functions just mentioned to approximate the solution of Equation 6-1, this does not mean that we will need to reintegrate the equations of motion for each distribution. That would be slow, wasteful and redundant. As stated earlier, our real difficulty lies in obtaining a means of evaluating the effect of the kernel function $S(E,\rho_o,T,\rho_f)$. In plain terms, we need to know what ρ_f and T result from an initial E and ρ_o; this is the function of $S(E,\rho_o,T,\rho_f)$. Exactly how often a particular E and ρ_o must be considered is the function of $N_o(E,\rho_o)$. Integration of the equations of motion will yield the necessary information about $S(E,\rho_o,T,\rho_f)$.

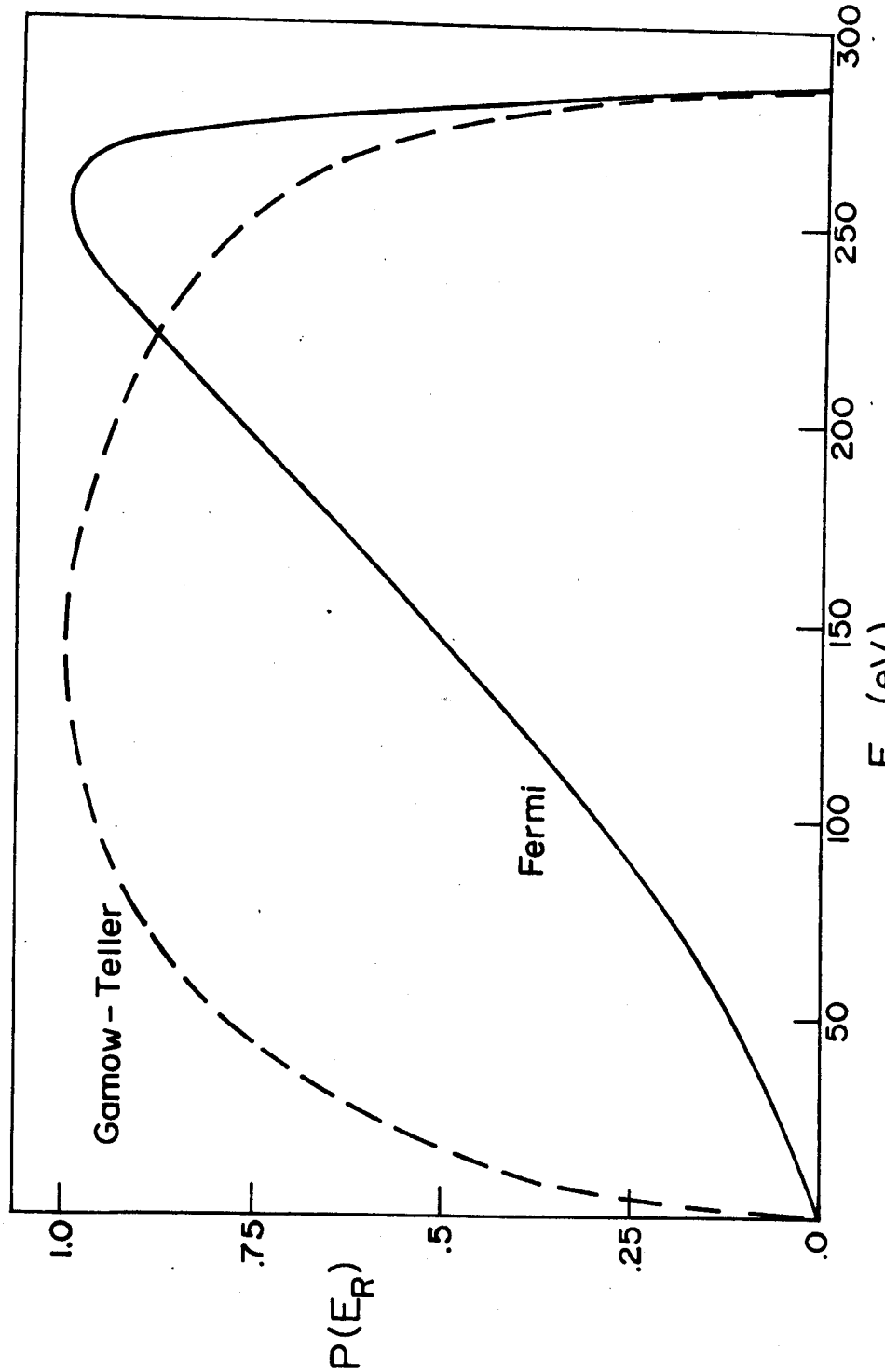

Figure 6-6. Recoil energy distributions for pure Fermi and pure Gamow-Teller decays.

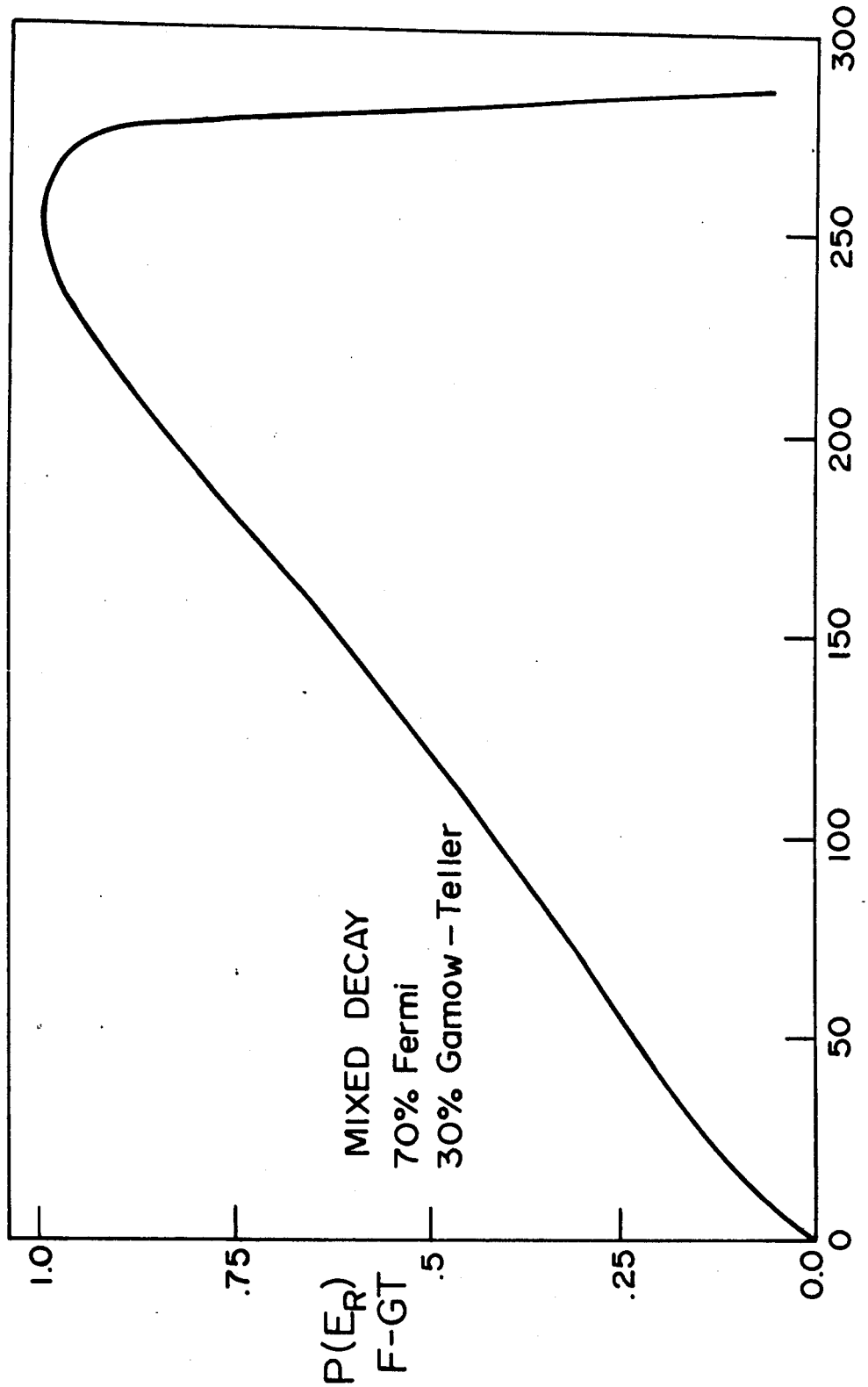

Figure 6-7. Recoil energy distribution for mixed decay.

$N_o(E,\rho_o)$ is ours to vary. In representing the distributions, we divide the energy range bounded by Equation 5-4 into a set of ten subintervals of a set length. So, in practice, our approximation to Equation 6-1 can be expressed as

$$P_f(T) = \sum_{j=1}^{10} \alpha_i S(E_j,T_j)\, N_o(E_j)(\Delta E_j) \qquad (6\text{-}27)$$

and

$$P_f(T) = \sum_{j=1}^{10} \rho_f(T_j) \qquad (6\text{-}28)$$

We have suppressed the ρ arguments for convenience. The index i refers to the ith bin in the energy interval and ΔE_i is the width of the ith bin. The term α_i is a weight factor. For the flat distribution $N_o(E_i)\Delta E_i$ is constant, so we have

$$P_f^{flat}(T) = A \sum_{j=1}^{10} \alpha_i S_j \qquad (6\text{-}29)$$

with

$$S_j \equiv S(E_j, T_j) \tag{6-30}$$

Thus, by evaluating the predicted P_f^{flat} for a flat distribution, we are able to obtain the elements S_j which are the most important and elusive quantities.

The combination of Equation 6-27 and 6-28 allow us to recast our problem in the form of matrix equations.

$$\underset{\sim}{P} = \underset{\approx}{S}\ \underset{\sim}{N}_o \tag{6-31}$$

We construct the $\underset{\approx}{S}$ matrix from Equation 6-29 and then proceed to apply Equation 6-31 to the various initial distribution functions of interest.

Results of Modeling

The determination of S was accomplished as just discussed and led to a number of reasonable conclusions. First, the TOF of a particle is completely a function of the Z velocity within a few nanoseconds of the 5 μsec TOF. While not surprising, it is something that could not be stated definitively before the calculations because of the field nonuniformities. Second, the effect of the kernel function S will not transform the flat energy distribution into the observed form. The result is basically still a

square wave as we input. In a way, the resolution of the difficulty seems to be hinted at by the first conclusion. This tells us that the TOF is dependent on the component of the momentum in the Z direction. Instead of using a flat energy distribution, it seemed reasonable to attempt a flat momentum distribution. Actually we used a flat distribution in the Z component of the momentum since the results are independent of the other components. In addition to the independence of the observed distribution on the transverse components, the initial distribution in these components are severely restricted by the limit curves of Figure 6-2 and reduce to a constant, multiplying the distribution in the Z momentum.

The results of the calculation using the flat momentum distribution gives a set of functional values of $P(T_i)$ at unequally spaced values of T_i, the time-of-flight for the ith bin. Treating these as functional values at unequally spaced base points (T_i's), I used a Newton Divided Difference Interpolation (See (Ca69)) to generate interpolate values at equally spaced time intervals. These values were then used to generate the plot shown in Figure 6-8. A similar procedure was followed for the other distribution functions. For the Fermi and Gamow-Teller initial distributions, the distribution functions that are the momentum equivalents of Figures 6-2 and 6-3, respectively, were used as the $N_o(\vec{P},\rho_o)$. The distribution

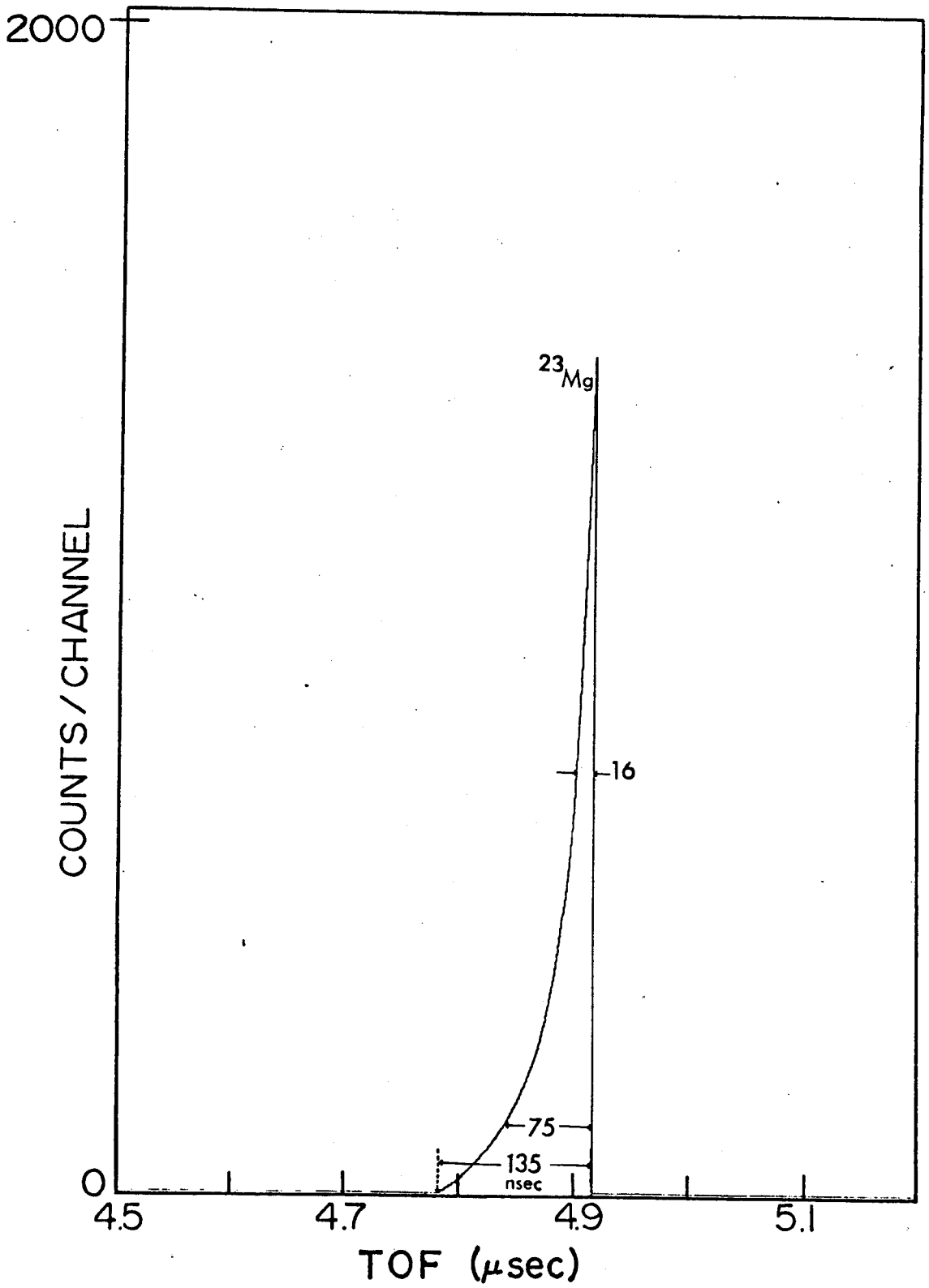

Figure 6-8. Theoretical TOF peak predicted from flat momentum distribution.

Table VI-2. Comparison of Peak Widths for Various Distributions.

	Obs. Peak	N_o^{flat}	N_o^{Fermi}	N_o^{GT}	N_n^{mix}
Base Width (nsec)	145	135	13	135	135
Width at 1 Max (nsec)	90	75	120	130	120
Width at 5 Max (nsec)	20	16	70	105	100

corresponding to the correct admixture of F and GT decay for ^{23}Mg was constructed by a linear combination of the F and GT distribution. The form used was

$$P_{mix} = \alpha P_F + (1 - \alpha)P_{GT} \qquad (6\text{-}32)$$

here $\alpha = .7$ for the case of ^{23}Mg.

The predicted TOF distributions corresponding to the Fermi and Gamow-Teller initial distributions are shown in Figures 6-9 and 6-10, respectively. In Figure 6-11 is shown the observed TOF spectrum resulting from the reaction ^{27}Al + 70-MeV ^{3}He which was discussed in Chapter III. The focus of interest is the large ^{23}Mg peak that we are attempting to simulate. On each of the ^{23}Mg peaks in Figures 6-8, 6-9, 6-10, and 6-11 are given the full widths at the base, at .1 peak maximum and half maximum, all in nanoseconds.

A visual comparison of the three predicted TOF distributions with the experimental ^{23}Mg peak heavily favors the peak shown in Figure 6-8 as the best reconstruction. The peak resulting from the Gamow-Teller distribution (Figure 6-10) has a tail on the short time side as the experimental peak, but is clearly the wrong shape. In addition, this peak is far too broad except at the base. The Fermi distribution gives rise to a peak (Figure 6-9) that is actually a rough mirror image of the experimental.

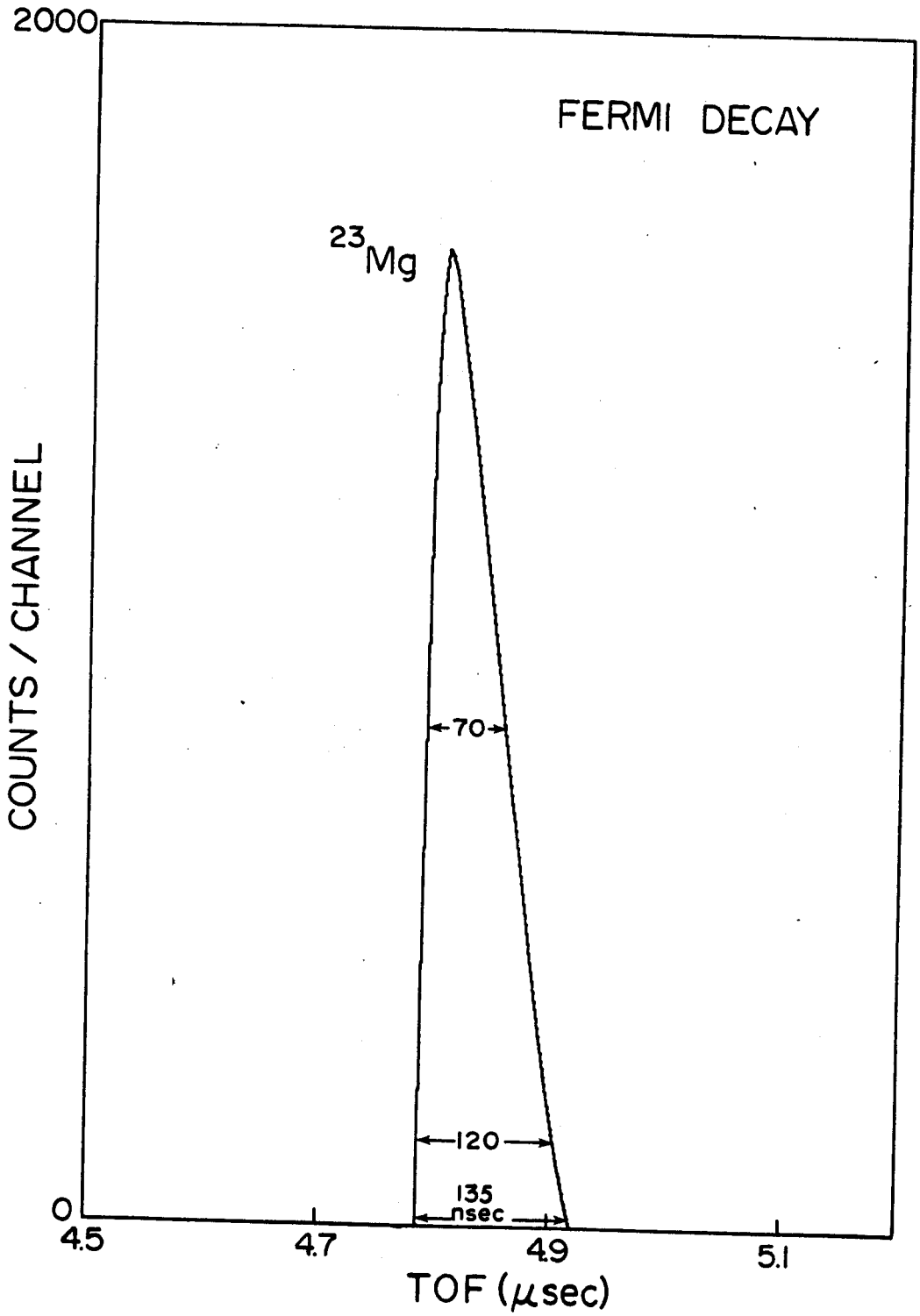

Figure 6-9. Theoretical TOF peak predicted from Fermi distribution.

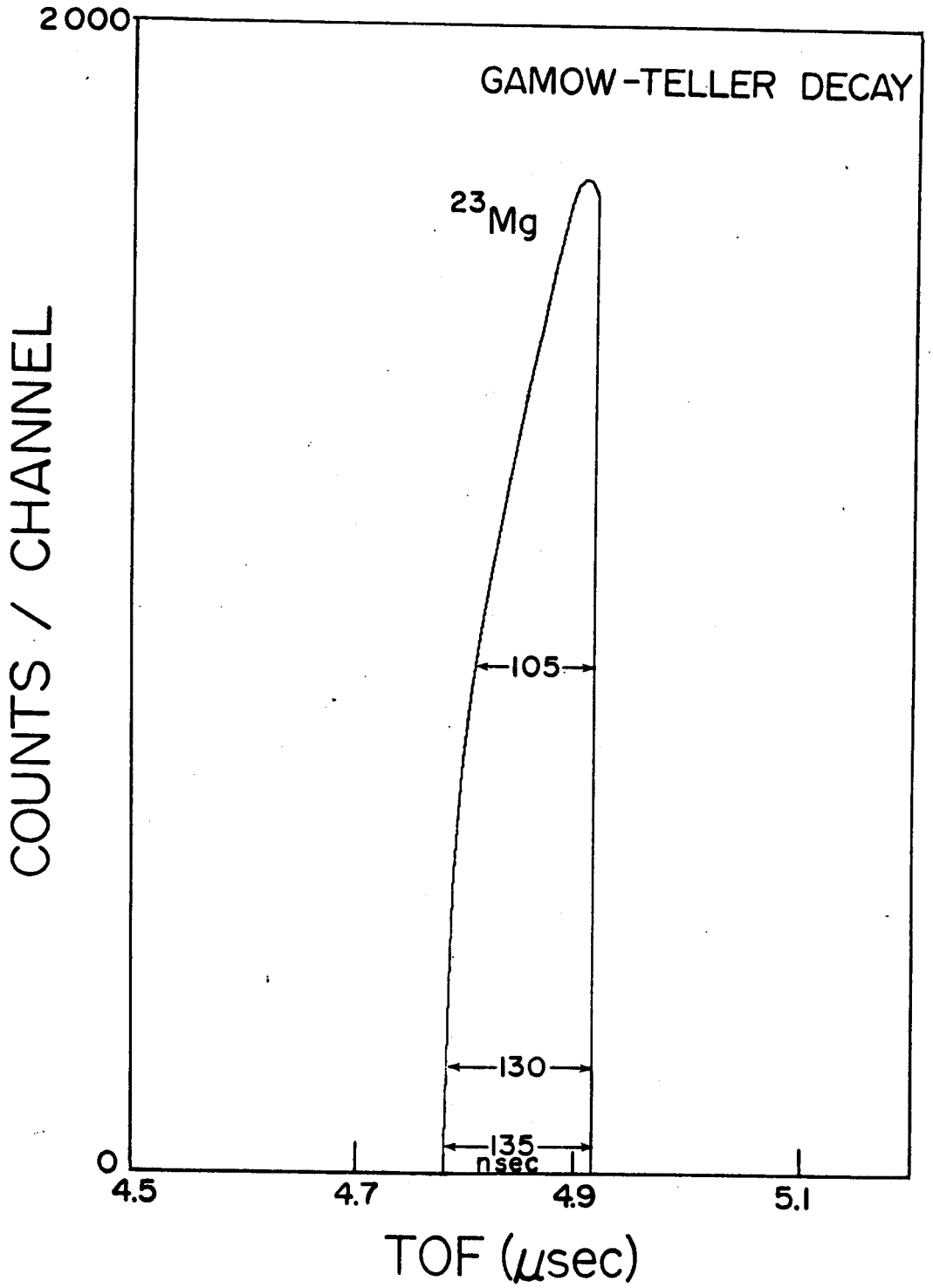

Figure 6-10. Theoretical TOF peak predicted from Gamow-Teller distribution.

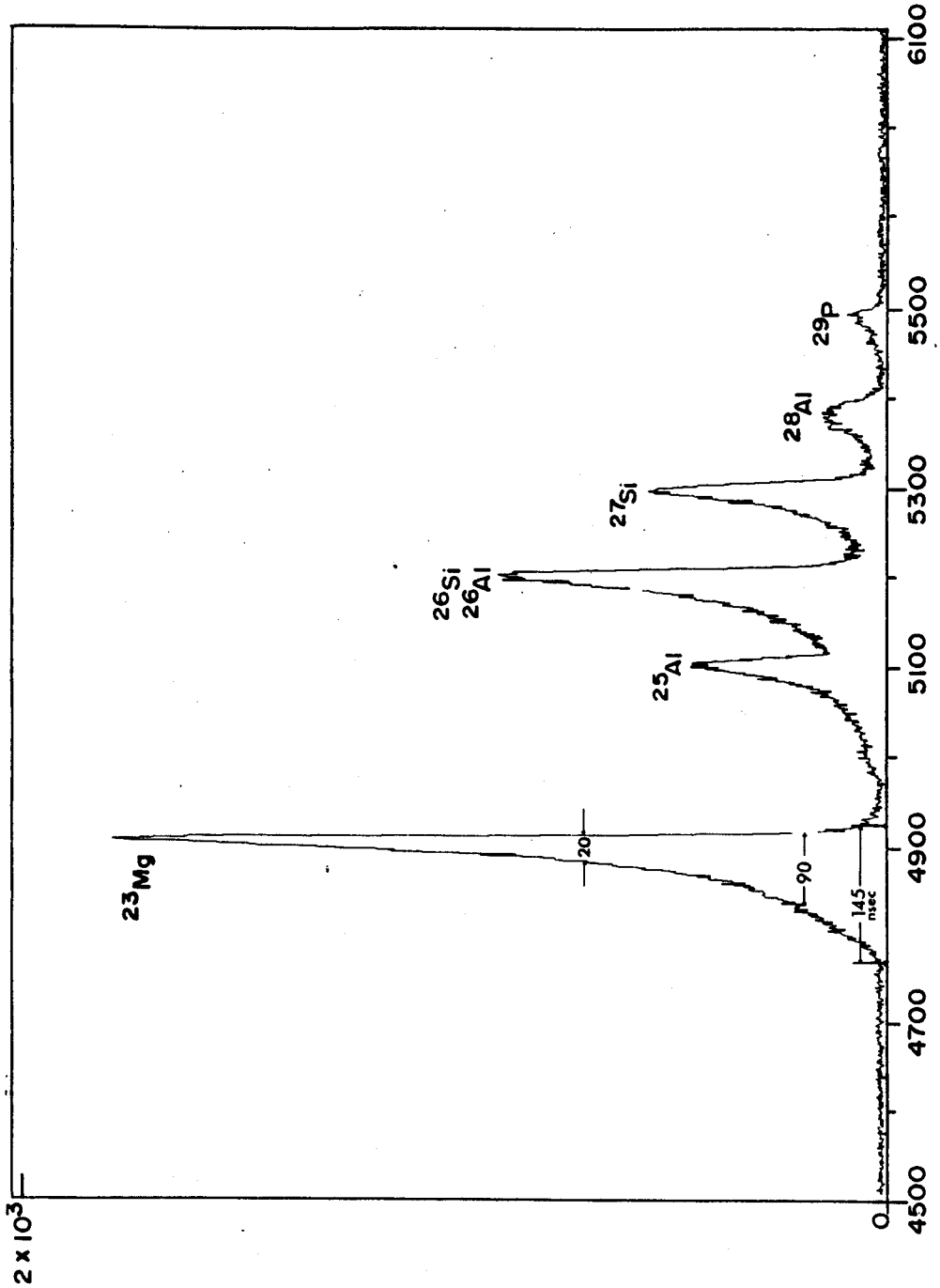

Figure 6-11. Observed TOF spectrum of products of ^{27}Al + 70-MeV ^{3}He reaction.

By this I mean that it has a sharp cutoff on the short TOF side and tailing on the longer TOF side which is the opposite of the experimental ^{23}Mg peak. The peak in Figure 6-8 results from a flat momentum distribution and is an excellent reproduction of the experimental peak. On the short TOF side there is the long bowed-tailing that is so obvious in Figure 6-11. Then the distribution comes to a sharp spike with the sudden dropoff on the long TOF side in the same manner as the experimental peak. The peak resulting from the initial distribution from Equation 6-32 has a shape similar to that of Figure 6-9, except that it is broader at .1 maximum and half maximum (See Table VI-2).

Quantitatively the N_o^{flat} (flat initial momentum distribution) gives the best predictions also. Referring to Table VI-2, the base width predicted is within 6.9% of the experimental width, the width at 0.1 maximum is within 16% and the full width at half-maximum (FWHM) is 25% off. This compares very well with the various widths predicted from the Fermi, GT and mixed distributions. These last three distributions result in widths at .1 max and half-max that are from 50% to 500% in error! The base widths for all the distributions are all the same since they correspond to the same definite limiting type events. That is, the base widths are set by the time differences between a particle starting out with 0.0 initial recoil energy and a particle starting out with the maximum velocity in the Z

direction. Both cases can only occur in one way and so are independent of the initial distribution assumed.

In many experimental instances, one uses the position of the peak maximum as the best estimate of the position of the centroid and then uses the associated time-of-flight to calculate the mass from Equation 3-2 (in Chapter III). The position of the peak maximum for the observed ^{23}Mg is 4910 nsec. The "flat momentum" peak has a predicted position of the maximum at 4915 nsec and the Gamow-Teller peak at 4908 nsec; both are in good agreement with the real peak. The Fermi distribution peak of Figure 6-9 has its maximum at 4800 nsec, which is well off the correct position. In fact, if we use Equation 3-2 with TOF = 4.8 μsec and HV = 6 kV, we get A = 22.0 -- off by one complete mass unit. This is not the case for the observed peak but does demonstrate the care that should be taken in choosing positions (on the peak of interest) to calculate the mass.

Although a little surprising, the simple flat distribution is the most successful in explaining the observed ^{23}Mg peak. The success is fairly impressive; (1) the peak position is correct to 5 nsec, which is a .1% error, (2) the base width is correct to 6%. Thus, theoretical broadening accounts for nearly 94% of the observed peak broadening. The simple model demonstrates the importance of the recoil energy on the observed peak broadening very clearly.

CHAPTER VII

CONCLUSIONS

In this thesis I have tried to present experimental results and theoretical analyses concerning the SEIGFRIED Recoil Mass Identification system. Before closing, I will briefly summarize the work presented and the conclusions drawn throughout this work.

First, it was demonstrated that the system works well in a number of different mass regions, although the chemical nature of the HeJRT system can be a real concern. Second, the observed TOF peaks were shown to contain information about the recoil ion's initial kinetic energy, which is a direct measure of the associated decay energy. To demonstrate the relation between the recoil energy and the peak shapes, I adopted a double-edged approach. First, I showed that a parameterization of the observed peak parameters yields reasonable predictions of the recoil energy and the decay energy. Second, I developed a reasonable theoretical model using numerical methods and used this model to simulate a theoretical peak corresponding to ^{23}Mg which I observed experimentally. The results of the modeling study were very successful. Using a simple

distribution, the experimental peak shape is reproduced very closely. The broadening of the peak was shown to be due to the recoil energy, and the theoretical broadening from this was 95% of the observed broadening. The overall success of our study in the experimental and theoretical studies proves the viability of using TOF system such as SIEGFRIED to identify mass products (measure A) and measure decay energies through the recoil energy. Combining these two measurements in a simple system provides the nuclear experimentalist with very useful and different tool for the study of nuclei far from stability.

APPENDIX I

As an approximate model of the time-of-flight system, we will use the geometry shown in Figure AI-1. In region I, the acceleration zone, there is a uniform electric field $\vec{E}$ with only a Z component. In region II there is a field-free drift zone of length ℓ. Thus, a particle of mass m and charge q is uniformly accelerated across region I and then drifts through region II.

Using cylindrical coordinates (ρ,ϕ,Z), the classical Lagrange equations of motion are:

$$\frac{d}{dt}(m\dot{\rho}) = m\rho\dot{\phi}^2 - q\frac{\partial\Phi}{\partial\rho} \tag{AI-1}$$

$$\frac{d}{dt}(m\rho^2\dot{\phi}) = 0q\frac{\partial\Phi}{\partial\phi} \tag{AI-2}$$

$$\frac{d}{dt}(m\dot{z}) = -q\frac{\partial\Phi}{\partial z} \tag{AI-3}$$

In region I

$$\vec{E} = \frac{V}{d}\hat{Z} \tag{AI-4}$$

$$\Phi = V(1 - Z/d) \tag{AI-5}$$

$$\frac{d}{dt}(m\dot{z}) = q\frac{V}{d} \tag{AI-6}$$

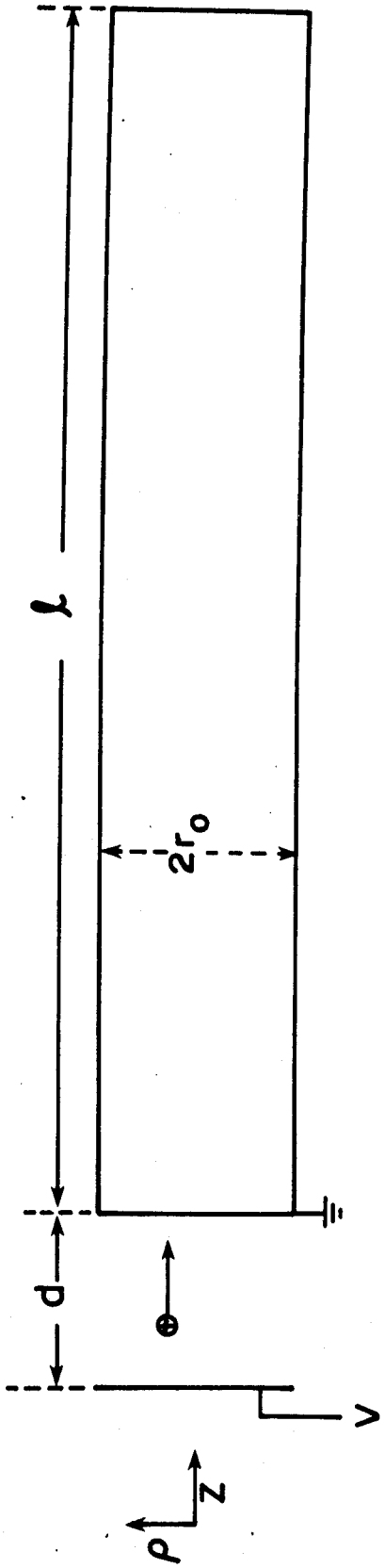

Figure AI-1.

Integrating twice with respect to time,

$$Z = Z_o + \dot{Z}_o t + \frac{qV}{md}\frac{t^2}{2} \qquad \text{(AI-7)}$$

where Z_o is the velocity in the Z direction at t = 0. We consider all particles starting from Z - 0 so $Z_o = 0$.

$$Z = \dot{Z}_o t + \frac{qV}{md}\frac{t^2}{2} \qquad \text{(AI-8)}$$

Solving for t, we have

$$t = \frac{md}{qV} - \dot{Z}_o + \sqrt{Z_o^2 + \frac{2qVZ}{md}} \qquad \text{(AI-9)}$$

When Z = d, the end of region I, the particle undergoes no further acceleration. Defining $\tau = t(z=d)$, the acceleration time, we have from Equation AI-9

$$\tau = \frac{md}{qV}\{-\dot{Z}_o + \sqrt{Z_o^2 + \frac{2qV}{m}} \qquad \text{(AI-10)}$$

Since Φ is independent of ϕ and ρ in both regions I and II, the remaining equations of motion are simple.

First, $\partial\Phi/\partial\phi = 0$, so Equation AI-2 tells us that $m\rho^2\dot{\phi}$ is a constant of motion. Actually, this is the angular momentum about the Z axis. Thus, we have

$$L \equiv m\rho^2\dot{\phi} = \text{constant} \tag{AI-11}$$

Using L to eliminate $\dot{\phi}$ from Equation AI-1, we have for the ρ equation

$$\frac{d^2\rho}{dt^2} = \frac{L^2}{m^2}\frac{1}{\rho^3} \tag{AI-12}$$

Equation AI-12, in spite of its simple form, is an example of a second-order nonlinear differential equation. While nonlinear differential equations of any order are notoriously difficult in general, this particular equation can be solved. Since appropriate references were not found we will solve this in a step by step manner!

Defining a new independent variable x,

$$x = \frac{Lt}{m} \tag{AI-13}$$

Equation AI-12 becomes

$$\frac{d^2\rho}{dx^2} = \frac{1}{\rho^3} \tag{AI-14}$$

Defining $u = \frac{d\rho}{dx}$, we have

$$u \frac{du}{d\rho} = \frac{1}{\rho^3} \tag{AI-15}$$

Integration gives

$$u^2 - u_o^2 = \frac{1}{\rho_o^2} - \frac{1}{\rho^2} \tag{AI-16}$$

or

$$\frac{d\rho}{dx} = \quad u_o^2 + \frac{1}{\rho_o^2} - \frac{1}{\rho^2} \tag{AI-17}$$

Integrating from x = 0 to x, we have

$$x = \frac{\rho_o^2}{1+(u_o\rho_o)^2}\left\{ \sqrt{(u_o^2 + \frac{1}{\rho_o^2})^2 - 1} \; - \; u_o\rho_o \right\} \tag{AI-18}$$

Inverting to solve for ρ, we get

$$\rho(x) = \sqrt{\frac{[(u_o^2 + 1/\rho_o^2)\, x + u_o\rho_o]^2 + 1}{u_o^2 + 1/\rho_o^2}} \tag{AI-19}$$

or in terms of t, L, and ρ_o

$$\rho(t) = \rho_o \sqrt{\frac{[(\dot{\rho}_o^2\rho_o^2+(L/M)^2)t/\rho_o^2+\dot{\rho}_o\rho_o]^2 + (L/m)^2}{(\dot{\rho}_o\rho_o)^2 + (L/m)^2}} \qquad \text{(AI-20)}$$

In region II there are no external forces acting on the particle, so the equations of motion are trivial. The only one we need to look at is Equation AI-3. For a particle "starting" from Z = d we have

$$\frac{d^2Z}{dt^2} = 0 \qquad \text{(AI-21)}$$

$$\dot{Z} = v_Z \text{ a constant} \qquad \text{(AI-22)}$$

and

$$Z = v_Z t + d \qquad \text{(AI-23)}$$

where t is measured from time of passing poind d. From the discussion concerning region I, we know that when Z = d its velocity Z_d is

$$\dot{Z}_d = \sqrt{Z_o^2 + \frac{2qV}{m}} \qquad \text{(AI-24)}$$

Thus

$$v_Z = \dot{Z}_d$$

We are interested in the time a particle takes to drift through region II. Calling this time T from Equation AI-23, we have

$$T = (\ell - d)/v_Z \qquad \text{(AI-26)}$$

$$T = (\ell - d)/\sqrt{Z_o^2 + \frac{2qV}{m}} \qquad \text{(AI-27)}$$

This will be called the drift time. The total time of flight is the sum of the drift time and the acceleration time:

$$TOF = T + \tau \qquad \text{(AI-28)}$$

$$TOF = \frac{(\ell-d)}{\sqrt{Z_o^2 + \frac{2qV}{m}}} + \frac{md}{qV}\left\{-Z_o + \sqrt{Z_o^2 + \frac{2qV}{m}}\right\} \qquad \text{(AI-29)}$$

APPENDIX II

A β decay is actually a three-body event, involving the decaying nucleus, the β particle, and a neutrino. If we define the following momenta and energies:

$\vec{r}$	momentum vector of daughter nucleus of mass M
$\vec{p}$	electron momentum vector
$\vec{q}$	neutrino momentum vector
E_o	total decay energy
E	total electron energy
E_ν	total neutrino energy
R	recoil energy

then the appropriate conservation laws take the forms:

$$E_o = E + E_\nu + R \qquad \text{(AII-1)}$$

$$q = E_\nu/c \qquad \text{(AII-2)}$$

$$E^2 = p^2c^2 + m^2c^4 \qquad \text{(AII-3)}$$

$$R = r^2/2M \qquad \text{(AII-4)}$$

$$\vec{r} = \vec{p} + \vec{q} \tag{AII-5}$$

$$r^2 = p^2 + q^2 + 2pq\cos\theta \tag{AII-6}$$

since $R << E + E_v$

$$E_o \simeq E + E_v \tag{AII-7}$$

$$q^2 = \frac{E_v^2}{c^2} \simeq \frac{(E_o-E)^2}{c^2} \tag{AII-8}$$

According to relativistic energy-momentum relation for the electron,

$$p^2 = (E^2 - m^2c^4)/c^2 \tag{AII-9}$$

$$r^2 = (E^2-m^2c^4)/c^2 + (E_o-E)^2/c^2 + \frac{(E_o-E)}{c}\ \frac{\sqrt{E^2-m^2c^4}}{c}\cos\theta \tag{AII-10}$$

$$R = \frac{r^2}{2M} = \frac{1}{2Mc^2}(E^2-m^2c^4) + (E_o-E)^2 + (E_o-E)\sqrt{E^2-m^2c^4}\ \cos \tag{AII-11}$$

We want R in terms of the kinetic energy of the electron, since for β^- decay the Q_β in the literature represents

the maximum kinetic energy of the electron. Defining T as the electron kinetic energy, we have

$$T = E - mc^2$$

$$Q_{\beta-} = T_o = E_o - mc^2$$

$$R = \frac{1}{2Mc^2} T(T+2mc^2) + (T_o-T)^2 + (T_o-T)\sqrt{T(T+2mc^2)}\cos\theta \qquad \text{(AII-12)}$$

R is a maximum for $\theta = 0$ and $T - T_o$, so

$$R_{Max} = \frac{T_o(T_o + 2mc^2)}{2Mc^2} \qquad \text{(AII-13)}$$

If we have T_o and mc^2 in units of MeV, we can get R_{Max} in eV by the formula

$$R = \frac{536.8}{A} (T_o(T_o + 1.022)) \qquad \text{(AII-14)}$$

where A is the mass number of the nucleus.

APPENDIX III

In any interpolation scheme, one starts with values of a function f(x), that is known (or conveniently obtained) at definite values of the independent variable x. The actual interpolation is estimating the values of the function for arguments between the base points x_o, x_1, $x_2, \ldots, x_n$ at which the functional values of $f(x_o)$, $f(x_1)$, $f(x_2)$, ..., $f(x_n)$ are known. The most common method used to solve such problems is to assume that a polynomial p(x) is a suitable approximation to the function f(x). This polynomial is forced to agree with the known values of f(x) and then used to predict an approximation to f(x) at x values that do not coincide with the base points.

The algorithm used for the field interpolations in this thesis was the Lagrangian Double 3-Point Interpolation scheme. The basis for this algorithm is that a linear combination of two quadratics is used for the interpolation polynomial. Referring to Figure AIII-1, the two quadratic polynomials are $\phi_1(x)$ and $\phi_2(x)$.

$$\phi_1(x) = ax^2 + bx + c \qquad \text{(AIII-1)}$$

$$\phi_2(x) = kx^2 + lx + m \qquad \text{(AIII-2)}$$

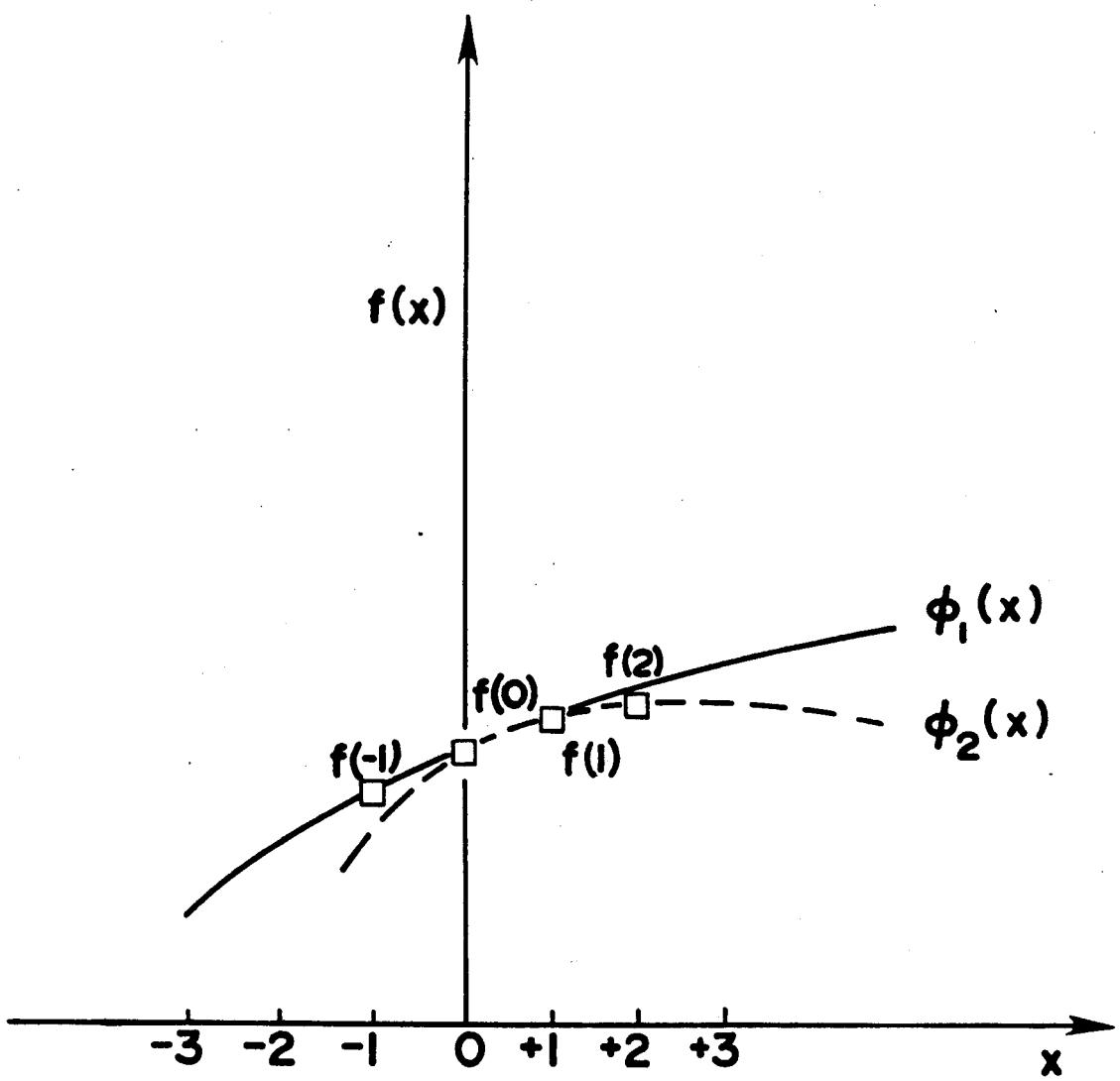

Figure AIII-1.

At the points x: =1,0,+1 we have for unit spacing

$$\phi_1(-1) = f(-1) \qquad \text{(AIII-3a)}$$

$$\phi_2(0) = f(0) \qquad \text{(AIII-3b)}$$

$$\phi_1(1) = f(1) \qquad \text{(AIII-3c)}$$

and at the points x: 0,1,2 we require

$$\phi_2(0) = f(0) \qquad \text{(AIII-4a)}$$

$$\phi_2(1) = f(1) \qquad \text{(AIII-4b)}$$

$$\phi_2(2) = f(2) \qquad \text{(AIII-4c)}$$

These sets of simultaneous equations can be solved to obtain the coefficients a, b, c, k, l, and m in terms of the $f(x_i)$'s. Now the interpolation polynomials become

$$\phi_1(x) = \frac{(f_1+f_{-1}-2f_o)}{2} x^2 + \frac{(f_1-f_{-1})}{2} x + f_o \qquad \text{(AIII-5)}$$

$$\phi_1(x) = \frac{(f_o+f_2-2f_1)}{2} x^2 + \frac{(4f_1-f_2-3f_o)}{2} x + f_o \qquad \text{(AIII-6)}$$

with $f_i \equiv f(x_i)$.

For the Lagrangian Double 3-Point algorithm we use an interpolating polynomial, F(x) which has the form

$$F(x) = (1-x)\phi_1(x) + x\phi_2(x) \qquad \text{(AIII-7)}$$

For our purposes we also need the derivative of F(x).

$$\frac{dF(x)}{dx} = -\phi_1(x) + (1-x)\frac{d\phi_1}{dx}(x) + \phi_2(x) + x\frac{d\phi_2}{dx}(x) \qquad \text{(AIII-8)}$$

More convenient forms for use with computer routines

$$F(x) = f(0)\cdot\{1 + 3x^3/2 - 5x^2/2\} + f(1)\cdot\{x/2 + 2x^2 - 3x^3/2\} + f(2)\cdot\{x^3/2 - x^2/2\} + f(-1)\cdot\{x^2 - x/2 - x^3/2\} \qquad \text{(AIII-9)}$$

$$\frac{dF(x)}{dx} = f(0)\cdot\{9x^2/2 = 5x\} + f(1)\cdot\{1/2 + 4x - 9x^2/2\} + f(2)\cdot\{3x^2/2 - x\} + f(-1)\cdot\{2x - 1/2 - 3x^2/2\} \qquad \text{(AIII-10)}$$

APPENDIX IV

To obtain approximate expressions for derivatives, we made use of a Taylor expansion. Consider development of the series for $f(x_o + \Delta x, y_o)$ about the point (x_o, y_o):

$$f(x_o+\Delta x,y_o) = f(x_o,y_o) = f(x_o,y_o) + \Delta x \left.\frac{\partial f}{\partial x}\right|_{x_o,y_o} + \frac{(\Delta x)^2}{2!} \left.\frac{\partial^2 f}{\partial x^2}\right|_{x_o,y_o}$$

$$+ \frac{(\Delta x)^3}{3!} \left.\frac{\partial^3 f}{\partial x^3}\right|_{x_o,y_o} + \ldots + \frac{(\Delta x)^n}{n!} \left.\frac{\partial^n f}{\partial x^n}\right|_{x_o,y_o} + \ldots, \qquad \text{(AIV-1)}$$

where, $|_{x_o,y_o}$ means the derivative is evaluated at the point (x_o, y_o).

Rearranging and dividing by Δx, we have

$$\left.\frac{\partial f}{\partial x}\right|_{x_o,y_o} = \frac{f(x_o+\Delta x,y_o) - f(x_o,y_o)}{\Delta x} - \frac{\Delta x}{2} \left.\frac{\partial^2 f}{\partial x^2}\right|_{x_o,y_o}, \qquad \text{(AIV-2)}$$

plus higher terms in Δx, or,

$$\left.\frac{\partial f}{\partial x}\right|_{x_o,y_o} \simeq \frac{f(x_o+\Delta x,y_o) - f(x_o,y_o)}{\Delta x} + O(\Delta x) . \qquad \text{(AIV-3)}$$

where $O(\Delta x)$ represents the order-of-magnitude error associated by the given approximation. Equation AIV-3 represents the "forward-difference" approximation to the derivative.

We could also obtain a "backward-difference" approximation by expansion of $f(x_o-\Delta x,y_o)$:

$$f(x_o-\Delta x,y_o) = f(x_o,y_o) - \Delta x \left.\frac{\partial f}{\partial x}\right|_{x_o,y_o} + \frac{(\Delta x)^2}{2!} \left.\frac{\partial^2 f}{\partial x^2}\right|_{x_o,y_o}$$

$$= \frac{(\Delta x)^3}{3!} \left.\frac{\partial^3 f}{\partial x^3}\right|_{x_o,y_o} + \ldots + (-1)^n \frac{(\Delta x)^n}{n!} \left.\frac{\partial^n f}{\partial x^n}\right|_{x_o,y_o} + \ldots, \qquad \text{(AIV-4)}$$

which can be rearranged to yield

$$\left.\frac{\partial f}{\partial x}\right|_{x_o,y_o} \simeq \frac{f(x_o,y_o) - f(x_o- x,y_o)}{\Delta x} + O(x) . \qquad \text{(AIV-5)}$$

As indicated, both the forward- and backward-difference approximations carry associated errors that are on the order of Δx. To obtain a better approximation to the derivative, one can subtract Equation AIV-4 from AIV-1 to obtain

$$f(x_o+\Delta x,y_o) - f(x_o-\Delta x,y_o) = 2\Delta x \left.\frac{\partial f}{\partial x}\right|_{x_o,y_o} + 2\frac{(\Delta x)^3}{3!}\left.\frac{\partial^3 f}{\partial x^3}\right|_{x_o,y_o}, \qquad \text{(AIV-6)}$$

plus higher terms.

This can be rearranged to yield

$$\left.\frac{\partial f}{\partial x}\right|_{x_o,y_o} \approx \frac{f(x_o+\Delta x,y_o) - f(x_o-\Delta x,y_o)}{2\Delta x} + O((\Delta x)^2) . \qquad \text{(AIV-7)}$$

This is called the "central-difference" approximation. Comparing the cutoff errors associated with approximations AIV-3, AIV-5, and AIV-7, it is evident that for $\Delta x < 1$, expression AIV-7 carries the smallest error.

To obtain an approximate expression for the second derivative, <u>add</u> Equation AIV-1 and AIV-4 and divide by $(\Delta x)^2$ to obtain

$$\frac{f(x_o+\Delta x,y_o) + f(x_o-\Delta x,y_o)}{(\Delta x)^2} = 2f(x_o,y_o) + \left.\frac{\partial^2 f}{\partial x^2}\right|_{x_o,y_o}$$

$$+ \frac{(\Delta x)^2}{12} \left.\frac{\partial^4 f}{\partial x^4}\right|_{x_o,y_o} , \qquad \text{(AIV-8)}$$

plus higher terms,

or,

$$\left.\frac{\partial^2 f}{\partial x^2}\right|_{x_o,y_o} \simeq \frac{f(x_o+\Delta x,y_o) + f(x_o-\Delta x,y_o) - 2f(x_o,y_o)}{(\Delta x)^2} + O((\Delta x)^2) \qquad \text{(AIV-9)}$$

As in the "central-difference" approximation to the first derivative, this expression has an associated error on the order of $(\Delta x)^2$.

BIBLIOGRAPHY

BIBLIOGRAPHY

(Ac70) F. S. Acton, Numerical Methods That Work, New York: Harper and Row, p. 489 (1970).

(Am69) W. F. Ames, Numerical Methods for Partial Differential Equations, New York: Barnes and Noble, p. 106 (1969).

(Bl73) M. Blann and F. Plasil, ALICE: A Nuclear Evaporation Code, U.S.A.E.C. Report No. COO-3494-10 (1973).

(Ca69) B. Carnham, H. A. Luther and J. O. Wilkes, Applied Numerical Methods, New York: John Wiley and Sons (1969).

(Ca63) T. Carlson, Phys. Rev. 130, 2361 (1963).

(Ed76) M. Edmiston, Ph.D. Thesis, Michigan State University, MSUNC-186 (1976).

(Fo60) G. E. Forsythe and W. R. Wasow, Finite Difference Methods for Partial Differential Equations, New York: John Wiley and Sons, p. 242 (1960).

(Gr65) I. S. Gradshteyn and I. W. Ryzhik, Table of Integrals, Series and Products, New York: Academic Press, p. 1 (1965).

(Ha62) R. W. Hamming, Numerical Methods for Scientists and Engineers, New York: McGraw-Hill, p. 194 (1962).

(Jo63) C. H. Johnson, F. Pleasonton and T. A. Carlson, Phys. Rev. 132, 1149 (1963).

(Ju71) H. Junglass, R. D. MacFarlane and Y. Fares, Radiochim. Acta. 16, 141 (1971).

(Ko73) K. L. Kosanke, Ph.D. Thesis, Michigan State University, COO-1779-76 (1973).

(LeB76) Y. LeBeyec, R. L. Hahn, K. S. Toth and R. Eppley, Phys. Rev. C 14, 1038 (1976).

(Ma74) R. D. Macfarlane, D. F. Torgerson, Y. Fares and C. A. Hassel, Nucl. Instr. Meth. 116, 381 (1974).

(Mu76) D. W. Mueller, Ph.D. Thesis, Michigan State University, MSUNC-160 (1976).

(Ne78) S. Negra, C. Deprun, H. Jungolas, H. Gauvin, J. P. Husson and Y. LeBeyec, Nucl. Instr. Meth., 156, 355 (1978).

(Ne79) S. D. Negra, C. Deprun, H. Gauvin, J. P. Husson and Y. LeBeyec, Laboratoire De Chemie Nucleaire-Orsay Report IPNC RC 79-04 (unpublished).

(Ro57) K. J. Roulstein and S. I. H. Naqvi, Nucleonics, 15, 86 (1957).

(Ro69) S. J. Routti and S. G. Prussin, Nucl. Instr. Meth. 72, 125 (1969).

(Si66) K. Siegbahn, Alpha-, Beta- and Gamma-Ray Spectroscopy, Amsterdam: North-Holland, p. 15 (1966).

(Wo76) H. Wolnik, Nucl. Instr. Meth. 139, 311 (1976).

(Wo77) H. Wolnik, B. Pfeiffer, J. P. Boequet, F. Schussler, Nucl. Instr. Meth. 144, 565 (1977).

(Wu66) C. S. Wu and S. A. Moscowski, Beta Decay, New York: John Wiley and Sons, p. 111 (1966).